CHEMICAL REVIEWS

pubs.acs.org/CR Review

Molecular-Modified Photocathodes for Applications in Artificial Photosynthesis and Solar-to-Fuel Technologies

Edgar A. Reyes Cruz,[†] Daiki Nishiori,[†] Brian L. Wadsworth,[†] Nghi P. Nguyen, Lillian K. Hensleigh, Diana Khusnutdinova, Anna M. Beiler, and G. F. Moore*

Cite This: *Chem. Rev.* 2022, 122, 16051−16109 Read Online

ABSTRACT: Nature offers inspiration for developing technologies that integrate the capture, conversion, and storage of solar energy. In this review article, we highlight principles of natural photosynthesis and artificial photosynthesis, drawing comparisons between solar energy transduction in biology and emerging solar-to-fuel technologies. Key features of the biological approach include use of earth-abundant elements and molecular interfaces for driving photoinduced charge separation reactions that power chemical transformations at global scales. For the artificial systems described in this review, emphasis is placed on advancements involving hybrid photocathodes that power fuel-forming reactions using molecular catalysts interfaced with visible-light-absorbing semiconductors.

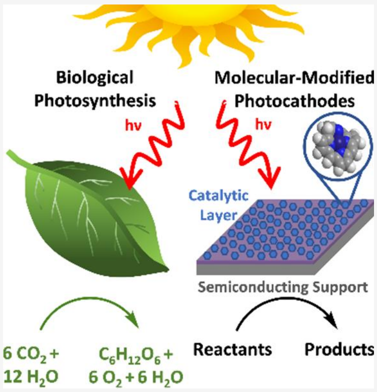

CONTENTS

1. INTRODUCTION

Artificial photosynthesis applies the fundamental principles of the natural/biological process including the capture, conversion, and storage of solar energy, to develop human-engineered counterparts.[1−6] Natural photosynthesis is currently the largest-scale process for storing light energy in the form of chemical bonds,[7,8] but the overall solar-to-fuel (STF) conversion efficiency is limited to a few percent and its products are already appropriated for powering the biosphere.[9] Although natural photosynthesis is a product of continued evolution stemming from environmental pressures and opportunities,[10] it is not designed to satiate the material and fuel-consumption demands of modern societies.[11] Conversely,

Received: March 25, 2022
Published: September 29, 2022

https://doi.org/10.1021/acs.chemrev.2c00200
Chem. Rev. 2022, 122, 16051−16109

if the associated technological and policy challenges can be surmounted, artificial photosynthesis offers a route to meeting global human energy demands with minimal environmental impact.[1,4,5,12−14] In this context, designing artificial photosynthetic assemblies that use "just the best bits" of the biological counterpart is a promising approach.[15,16]

The coupling of solid-state light capture and conversion technologies (i.e., semiconductors) with electrocatalytic materials yields a strategy for selectively driving industrially relevant chemical transformations using the power of the sun.[17−20] In an example that utilizes existing technologies, photovoltaics (PV) can power a separate electrocatalytic component for generating oxygen and hydrogen from water in an approach referred to as PV-electrolysis. Because this is achievable using commercially available components, PV-electrolysis is at a relatively high technology readiness level in comparison to other STF technologies.[6] In contrast, photoelectrochemical (PEC) approaches that directly integrate the light-absorbing and catalytic components are at a relatively low technology readiness level but are a subject of intense research given their potential to require fewer material components and reduce costs associated with installation and operation.[6]

Herein, we give an overview of the functionalization strategies and characterization methods used to assemble and study visible-light-absorbing semiconductors modified with molecular, fuel-forming catalysts.[21−25] Such constructs have demonstrated promising performance; however, there is currently insufficient understanding of how charge carriers move through these systems to provide rational design principles.[26−30] Related to this, the development of new methods to interface electrocatalysts with semiconductor electrodes and characterize the resulting assemblies are active areas of research investigation undertaken by both relatively large collaborative teams and individual research groups.[4,5,31,32] Although the current availability of ligand platforms able to withstand oxidative operating conditions may limit their applications,[33] in general, molecular-based modification of semiconductors offers opportunities to combine the relatively high activity, selectivity, and tunability of molecular components with the favorable solar energy capture and conversion properties of solid-state semiconducting materials.[34,35]

2. PHOTOCHEMISTRY, PHOTOELECTROCHEMISTRY, PHOTOCATALYSIS, PHOTOSYNTHESIS, PHOTOELECTROSYNTHESIS, AND EFFICIENCIES

Photochemistry is a branch of chemistry concerned with the chemical effects of light.[36,37] Photoelectrochemistry involves the application of one or more light-absorbing semiconductor electrodes in contact with an electrolyte, and it uses photogenerated charge carriers (electrons and holes) to drive redox transformations.[38−41] In general, assemblies that utilize light to promote chemical reactions can be classified as excitonic chemical conversion systems.[42] The terms photocatalytic and photosynthetic have sometimes been used interchangeably to describe excitonic chemical conversion systems.[42] However, it has been recommended that these terms not be used in an analogous fashion because they can be distinguished via the overall thermodynamics of the related reactions.[38,39,43] Photocatalytic reactions are exergonic (Gibbs free energy change $\Delta G < 0$), meaning there is no net storage of chemical energy, yet light is required to accelerate the reaction kinetics. Conversely, photosynthetic reactions are endergonic ($\Delta G > 0$), meaning photonic energy is stored in the bonds of the chemical products.[39] Photosynthetic systems have been further divided into the categories of type-1 and type-2, where type-1 assemblies spatially separate the cathodic and anodic half-reactions to prevent reverse reactions, and type-2 assemblies employ charge-transfer selectivity to prevent reverse reactions.[42] Further, photoelectrosynthetic systems are a subset of photosynthetic systems, constituting examples where a chemical bias is replaced by an electrochemical bias.[42]

The efficiencies of photochemical systems can be broadly separated into either benchmarking- or diagnostic-type efficiencies. Benchmarking efficiencies are ratios of total power output to total power input. In the case of solar PEC hydrogen production from water, this is the solar-to-hydrogen (STH) conversion efficiency; however, related equations for other chemical products can be expressed more generally as STF conversion efficiency.[13,44,45] As shown in eq 1a,[46] the STF conversion efficiency is the ratio of the chemical power produced to the total incident solar power. In this particular example involving hydrogen evolution and thus STH, the chemical power is the product of the rate of hydrogen evolution, which can be determined via chemical analysis methods, and the standard Gibbs free energy change per mole of hydrogen formed via the splitting of water ($\Delta G° = \Sigma\Delta G_f°(\text{products}) - \Sigma\Delta G_f°(\text{reactants}) = 237.14$ kJ mol H_2^{-1} at 1 bar and 25 °C, where $\Delta G_f°$ is the standard Gibbs free energy change of formation). The total incident solar power is the product of the area of the light absorber and the incident illumination power density (P_{total}), which is 100 mW cm^{-2} under air mass 1.5 global tilt (AM 1.5 G)[47] conditions. As shown in eq 1b, the chemical energy output can also be expressed as the product of the standard cell potential of the overall chemical reaction ($E°_{\text{cell}} = E°_{\text{anode}} - E°_{\text{cathode}} = -\Delta G°/nF = 1.23$ V, where F is the Faraday constant (96485 C mol^{-1}) and n is the number of electrons involved in the reaction (4 in the case of water splitting), the short-circuit current density (J_{sc}), and the faradaic efficiency of the reaction (FE).[46] This latter approach involves (photo)electrochemical methods of determining the chemical energy output but also requires knowledge (or an assumption) of FE, which as shown in eq 1c is the ratio of the amount of chemical product (N) to the total amount of charge passed during the PEC reaction (Q) multiplied by the Faraday constant (F) and the number of electrons required to form the product (n):

$$STH = \left[\frac{(237\ \text{kJ mol H}_2^{-1}) \times (\text{mol H}_2\ \text{s}^{-1})}{Area\ (\text{cm}^2) \times P_{total}\ (\text{mW cm}^{-2})}\right]_{AM1.5G} \qquad (1a)$$

$$STH = \left[\frac{(1.23\ \text{V}) \times |J_{\text{sc}}\ (\text{mA cm}^{-2})| \times \eta_F}{P_{\text{total}}\ (\text{mW cm}^{-2})}\right]_{AM1.5G} \qquad (1b)$$

$$FE = \frac{n \times N\ (\text{mol}) \times F\ (\text{C mol}^{-1})}{Q\ (\text{C})} \qquad (1c)$$

Unlike benchmarking efficiencies, which strictly involve measurements using two-electrodes (i.e., a cathode and an anode) with no electrochemical or chemical biasing, diagnostic efficiencies can involve applications of bias potentials (V_b) or the use of three-electrodes (i.e., working, counter, and reference electrodes), which enable decoupling and determination of kinetic and thermodynamic properties associated with the cathode or anode component of a PEC cell. The applied bias photon-to-current efficiency (ABPE) is an example of a diagnostic efficiency that differs from the STF efficiency because it involves application of a V_b between the working and counter electrode to produce a photocurrent density (J_{ph}), as shown in eq 2:[46]

$$ABPE = \left[\frac{[1.23\ \mathrm{V} - |V_b|\ (\mathrm{V})] \times J_{ph}\ (\mathrm{mA\ cm^{-2}})}{P_{total}\ (\mathrm{mW\ cm^{-2}})}\right]_{AM1.5G} \tag{2}$$

If an ABPE is reported for a three-electrode measurement, it is recommended the potential difference between the working electrode and the counter electrode as well as the potential difference between the working electrode and reference electrode are reported.[46]

Other diagnostic-type efficiencies involve counting of particles rather than energy or power. For example, the external quantum efficiency (EQE) (sometimes referred to as the incident photon-to-current efficiency (IPCE)) can be defined as the ratio of electron flux measured as current to incident photon flux (i.e., particles of light, and not power of light) as shown in eq 3a. EQE can also be defined as the product of the probability of photon absorption (Φ_{abs}), the probability of charge separation (Φ_{sep}), and the probability of charge injection across a semiconductor junction (Φ_{inj}). As shown in eq 3b, Φ_{abs} represents the fraction of incident photons absorbed by a material and is synonymous with the terms light harvesting efficiency (LHE) as well as absorptance. The internal quantum efficiency (IQE) (sometimes referred to as the absorbed photon-to-current efficiency (APCE)), represents another type of benchmarking efficiency, and can be defined as the ratio of electron flux measured as current, to absorbed photon flux as shown in eq 3c.[46] IQE can also be defined as the product of Φ_{sep} and Φ_{inj} and is thus equal to the EQE divided by LHE:

$$EQE = IPCE = \frac{electrons\ (\mathrm{cm^{-2}\ s^{-1}})}{incident\ photons\ (\mathrm{cm^{-2}\ s^{-1}})} = \Phi_{abs}\Phi_{sep}\Phi_{inj} \tag{3a}$$

$$\Phi_{abs} = LHE = \frac{absorbed\ photons\ (\mathrm{cm^{-2}\ s^{-1}})}{incident\ photons\ (\mathrm{cm^{-2}\ s^{-1}})} \tag{3b}$$

$$IQE = APCE = \frac{electrons\ (\mathrm{cm^{-2}\ s^{-1}})}{absorbed\ photons\ (\mathrm{cm^{-2}\ s^{-1}})} = \Phi_{sep}\Phi_{inj} \tag{3c}$$

Although they are not necessarily types of efficiencies, parameters for describing durability and activity include the turnover number (TON) and turnover frequency (TOF). TON is defined as the number of moles of substrate transformed by one mole of catalyst,[48] and TOF is the time derivative of TON.[49] For one-electron reduction reactions and two-electron reduction reactions where the first one-electron reaction between the catalyst and substrate is rate-determining,[50] TON and TOF are expressed using eqs 3d and 3e:[48]

$$TON = \frac{N}{N_{cat}} = \frac{kC_A{}^0 t}{1 + \exp\left[\frac{F}{RT}(E - E_{PQ}{}^0)\right]} \tag{3d}$$

$$TOF = \frac{N_{\text{per unit of time}}}{N_{cat}} = \frac{kC_A{}^0}{1 + \exp\left[\frac{F}{RT}(E - E_{PQ}{}^0)\right]} \tag{3e}$$

where N is the amount of chemical product, N_{cat} is the total amount of catalyst on the surface, k is the apparent rate constant associated with the catalytic reaction, $C_A{}^0$ is the concentration of the chemical substrate, t is time, E is the electrode potential, $E_{PQ}{}^0$ is the standard reduction potential of the catalyst, R is the gas constant, T is the temperature, and $N_{\text{per unit of time}}$ is the amount of product generated per unit of time. When the electrode activity is limited only by kinetics associated with chemical catalysis, and not by electron-transfer kinetics or mass-transfer phenomena, all the catalysts at the electrode surface are effectively in their activated forms and the concentration of chemical substrate at the electrode surface is approximately equal to its bulk concentration. Under these conditions, the plateau current of the voltammogram will not increase upon increasing the scan rate, and the TOF equals the maximum turnover frequency (TOF_{max}) as shown in eq 3f:[49]

$$TOF_{max} = kC_A{}^0 \tag{3f}$$

Given that electron flux can be expressed as a product of n (the number of electrons required for the reaction), TOF, Γ_{C_T} (per geometric area density of the total catalyst), and Avogadro constant (N_A), eq 3a can be transformed into eq 3g, which shows the connection between EQE and TOF:

$$EQE = \frac{n \times TOF\ (\mathrm{s^{-1}}) \times \Gamma_{C_T}\ (\mathrm{mol\ cm^{-2}}) \times N_A\ (\mathrm{mol^{-1}})}{incident\ photons\ (\mathrm{cm^{-2}\ s^{-1}})} \tag{3g}$$

If the photoelectrosynthetic illumination intensity, charge transfer rate constants, and the concentration of chemical substrates are sufficiently high, TOF in eq 3g will be replaced with TOF_{max} upon sufficiently biasing the electrode potential, meaning that the overall efficiency (EQE) associated with the fuel-forming reaction can become limited by the value of TOF_{max}.

For all types of efficiencies reported in the literature, it is informative to know where the counting starts (e.g., number of incident photons or incident power versus number of absorbed photons or absorbed power) and where the counting ends (e.g., carriers measured as current moving a potential versus enthalpies or Gibbs free energies associated with the chemical products). The implementation and limitations associated with these types of efficiencies have been described elsewhere.[46,51] While these efficiency calculations provide standardized approaches for making comparisons between photochemical assemblies, other important considerations include monetary costs and stability of the materials.[9,52]

3. NATURAL PHOTOSYNTHESIS

Nature utilizes an array of pigments to harvest solar energy including chlorophylls, bacteriochlorophylls, carotenoids, and phycobilins. These molecules can be arranged in antenna complexes, where the absorption of light triggers spatial and energetic funneling of photonic energy to chlorophyll-based reaction centers that initiate a cascade of photoinduced electron-transfer events.[53] The pigments in the antenna enable use of a larger cross-section of the solar spectrum compared to what can be directly absorbed via chlorophyll-based reaction centers.[53−55] For example, in Photosystem I (PSI) (Figure 1),

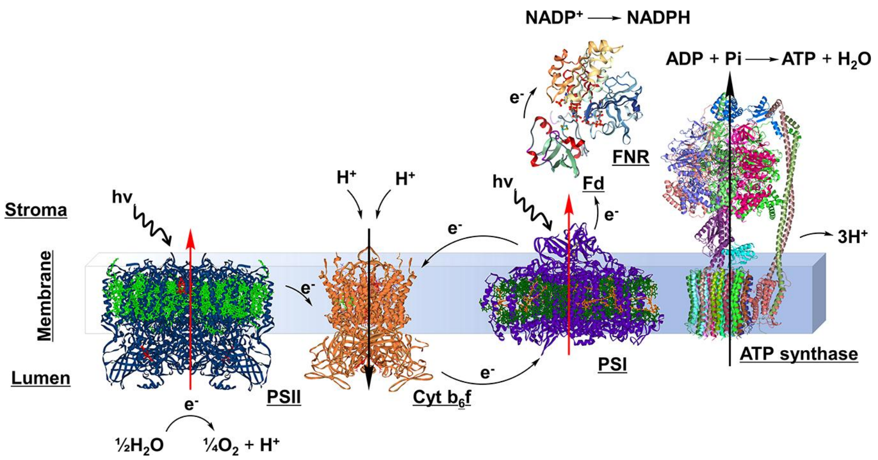

Figure 1. Diagrammatic scheme highlighting the light-induced electron- and proton-transfer reactions occurring within and across the thylakoid membrane of oxygenic photosynthetic organisms. Four major intramembranous protein complexes are shown including Photosystem II (PSII; water-plastoquinone oxidoreductase), cytochrome (Cyt) b_6f (plastoquinol-plastocyanin-oxidoreductase), Photosystem I (PSI; plastocyanin-ferredoxin-oxidoreductase), and ATP synthase.

the modified chlorophyll *a* reaction center, P700, has relatively intense absorption bands in the blue (Soret bands) and red (Q bands) regions of the solar spectrum, but the surrounding antenna complex enables utilization of photons at wavelengths where the LHE of P700 is relatively low.[54] Although high light fluxes can result in photodamage, nature has evolved elaborate protection, regulation, and repair mechanisms.[56,57] These include the rapid quenching of chlorophyll triplet states via energy transfer to surrounding carotenoids, thereby avoiding the generation and damaging effects of singlet oxygen.[58]

Following the transfer of energy to a reaction center, the resulting excited state is transformed to charge-separated states. In biological photosynthetic assemblies, multistep electron-transfer reactions involving molecular cofactors spatially separate charges, resulting in relatively long lifetimes of the final charge-separated state and an electron motive force that is appropriate for meeting the thermodynamic demands of water splitting.[54,55] As an example, initiation of photoinduced charge transfer reactions from the excited-state reaction center of PSI to neighboring chlorophyll *a* (A_0) is followed by a series of subsequent electron-transfer steps involving phylloquinone (A_1), three iron-sulfur protein clusters (F_x, F_A, and F_B) (Figure 2), and ferredoxin, which shuttles electrons to ferredoxin−NADP$^+$ reductase.[55,59] Each electron-transfer step increases the physical distance between the resulting electron−hole pair (~7−16 Å per electron transfer), thereby reducing the rates of charge recombination.[54] However, each electron-transfer step occurs at the thermodynamic expense of utilizing a fraction of the initially absorbed photonic energy and therefore limits the energy that can be stored in chemical products.

As shown in Figure 3, the electron-transfer kinetics associated with photosynthetic complexes, including PSI, have been modeled using the Marcus−Hush−Levich equation, where the rate constant for electron transfer (k_{et}) in the adiabatic regime is described by eq 4:[60−62]

$$k_{\mathrm{et}} = \sqrt{\left(\frac{\pi}{\hbar^2 \lambda k_B T}\right)}\, |H_{AB}|^2 e^{\left[-\frac{(\Delta G^\circ + \lambda)^2}{4\lambda k_B T}\right]} \tag{4}$$

In eq 4, the pre-exponential factor includes the reduced Planck constant ($\hbar = 1.054571 \times 10^{-34}$ J s), the reorganization energy (λ) (describing the energy required for structural adjustments to distort the nuclear configuration of the reactants into the nuclear configuration of the products without charge transfer occurring), the Boltzmann constant ($k_B = 1.380649 \times 10^{-23}$ J K^{-1}), temperature (T), and the electronic matrix element (H_{AB}) (describing the overlap of donor and acceptor orbitals between the reactants and products). The exponential term is the Franck−Condon factor, which includes ΔG° for the electron-transfer reaction and λ. Eq 4 is essentially a nonlinearized version of the Butler−Volmer expression,[63,64] where the charge-transfer coefficient changes as a function of the driving force. In general, there are three distinct regimes of electron transfer kinetics associated with Marcus−Hush−Levich theory. In the normal region, where the negative standard Gibbs free energy change for electron transfer is less than the reorganization energy (i.e., $-\Delta G^\circ < \lambda$), the rate of electron transfer increases as a function of increasing thermodynamic driving force (Figure 3a). When the negative standard Gibbs free energy change for electron transfer is equal in value to the reorganization energy ($-\Delta G^\circ = \lambda$) electron transfer becomes activationless and the rate of electron transfer is thus maximized (Figure 3b). Further increasing the driving force to conditions where the negative standard Gibbs free energy change for electron transfer is greater than the reorganization energy ($-\Delta G^\circ > \lambda$) results in inverted region kinetics where the rate of electron transfer decreases as the thermodynamic driving force increases (Figure 3c). Inverted region behavior has been invoked to rationalize the relatively sluggish kinetics associated with charge recombination pathways in biological photosynthesis (indicated with dashed blue arrows in Figure 2) as compared to the relatively fast rates of forward electron-transfer steps (indicated with solid blue arrows in Figure 2). Similar inverted region behavior is generally not observed in electron-transfer reactions involving electrode materials (as indicated by the dashed gray line of Figure 3d). In this case, the relatively high density of states associated with conductive materials favors overlap of initial and final states with activationless electron-transfer kinetics.

An overall equation for natural photosynthesis is shown in eq 5:

$$6CO_2 + 12H_2O + hv \rightarrow C_6H_{12}O_6 + 6O_2 + 6H_2O \tag{5}$$

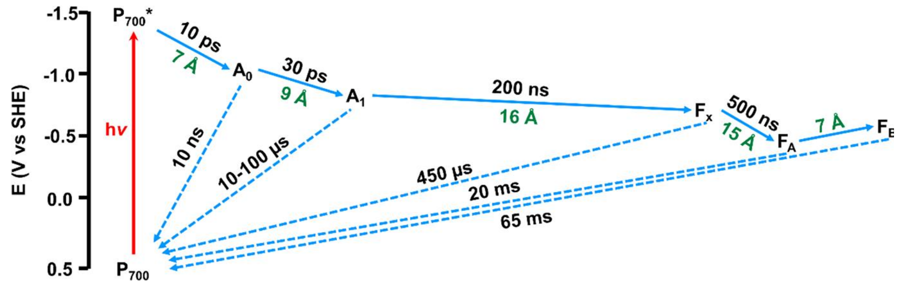

Figure 2. Energy-kinetic diagram showing the photochemistry and electron-transfer events associated with PSI. In this diagram, chlorophyll A_0 serves as a redox mediator between the excited state P700* reaction center and phylloquinone A_1.

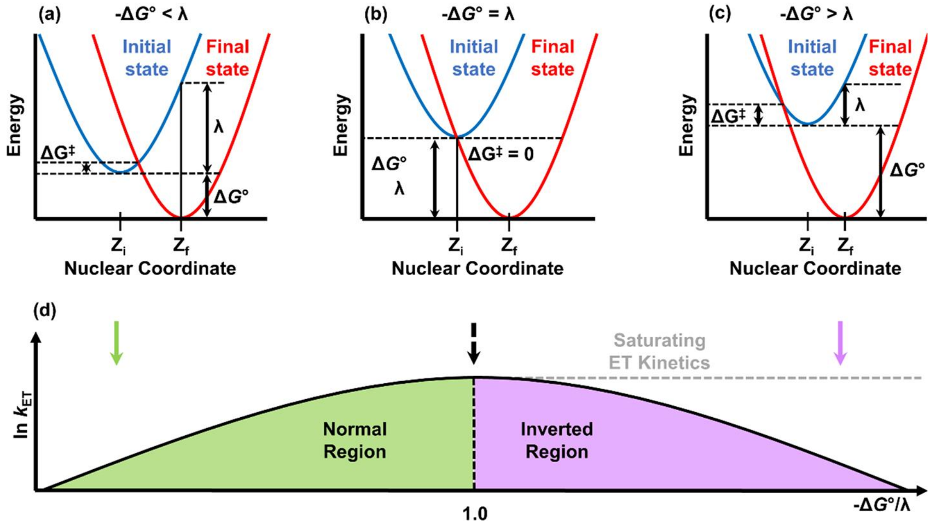

Figure 3. (a−c) Marcusian diagrams with potential energy surfaces for electron transfer from an initial state (blue) to a final state (red). Each case represents one of three different scenarios in the (d) Marcus curve: normal region (green), the activationless point (dashed black line), the inverted region (pink), and saturating electron-transfer kinetics (dashed gray line).

Consistent with this equation, Ruben and co-workers have shown via ^{18}O isotope labeling experiments that oxygen atoms of the product O_2 are derived from oxygen atoms of reactant H_2O, and the oxygen atoms of the reactant CO_2 are used to form additional molecules of H_2O in the product state.[65] By utilizing photoinduced charge-separation reactions, photosynthetic organisms are capable of extracting electrons from water at the oxygen evolving complex (OEC) of Photosystem II (PSII) and storing them in the form of relatively high energy chemical reducing equivalents. In this process, PSII and PSI act in series, with PSII handling the oxidative chemistry (eq 6a) and PSI handling the reductive chemistry (eq 6b) via a 'wireless' process that achieves overall splitting of water:

$$2H_2O \rightarrow O_2 + 4H^+ + 4e^- \quad E^{\circ\prime} = -0.81\ \text{V vs NHE (pH 7)} \tag{6a}$$

$$2NADP^+ + 4H^+ + 4e^- \rightarrow 2NADPH + 2H^+ \quad E^{\circ\prime} = -0.32\ \text{V vs NHE (pH 7)} \tag{6b}$$

In PSI, electrons are transferred to the ferredoxin−$NADP^+$ reductase enzyme and used to facilitate light-driven formation of reduced nicotinamide adenine dinucleotide phosphate (NADPH) (Figure 1). NADPH can also be generated along with CO_2 by the breakdown of glucose ($C_6H_{12}O_6$) via the pentose phosphate pathway. NADPH is then utilized as a chemical reductant in the Calvin−Benson−Bassham cycle, sometimes referred to as the reductive pentose phosphate pathway, where CO_2 fixation occurs to form glyceraldehyde-3-phosphate (G3P), which is used to form carbohydrates including glucose.[66,67] Unlike the light-driven processes occurring at PSII and PSI, the Calvin cycle occurs in the dark. As shown in eq 7, this cycle involves proton- as well as electron-transfer reactions that are powered by the hydrolysis of adenosine triphosphate (ATP), a molecule that stores as well as intracellularly transports energy in chemical form and is also a product of photosynthesis (*vide infra*):

$$3CO_2 + 6NADPH + 6H^+ + 9ATP \rightarrow G3P + 6NADP^+ + 9ADP + 3H_2O + 8P_i \tag{7}$$

Electron-transfer reactions in biology are often coupled to proton-transfer reactions. As an example involving oxygenic photosynthesis, the cytochrome plastoquinol-plastocyanin-oxidoreductase (Cyt b_6f) complex shuttles electrons between plastoquinol, which forms upon the reduction of plastoquinone at the Q_B site of PSII, to plastocyanin, which in turn transfers electrons to the P700 cofactor of PSI, while also pumping protons from the stromal side of the membrane protein to its luminal side. This results in the formation of a proton motive force that ultimately powers the synthesis of ATP (Figure 1).[68−71] Thus, a fraction of the initially absorbed photonic energy is used to drive the formation of electron as well as proton gradients and the generation of NADPH as well as

ATP. Proton-coupled electron transfer (PCET) processes found in biology have inspired the design of synthetic assemblies.[72−81] Ultimately, the ability to incorporate and control PCET processes is essential to designing artificial photosynthetic systems that effectively couple the inherent one-photon to one-electron chemistry of light absorption with the multielectron, multiproton chemistry required for nearly all fuel-forming reactions relevant to solar photochemistry (Table 1).[28,82−87]

Table 1. Formal ($E^{\circ\prime}$ at pH 7) and Standard[a] (E° at pH 0) Potentials Written as Reduction Half-Reactions by Convention[b]

half-reactions relevant to solar photochemistry	
half-reaction	potential (V vs NHE)
$N_2 + e^- \rightarrow N_2^-$	$E^{\circ\prime} = -4.2$
$N_2 + H^+ + e^- \rightarrow N_2H$	$E^{\circ} = -3.2$[a]
$CO_2 + e^- \rightarrow CO_2^{\bullet -}$	$E^{\circ\prime} = -1.90$
$CO_2 + 2H^+ + 2e^- \rightarrow HCO_2H$	$E^{\circ\prime} = -0.61$
$CO_2 + 2H^+ + 2e^- \rightarrow CO + H_2O$	$E^{\circ\prime} = -0.53$
$2CO_2 + 2H^+ + 2e^- \rightarrow H_2C_2O_4$	$E^{\circ\prime} = -0.49$
$CO_2 + 4H^+ + 4e^- \rightarrow HCHO + H_2O$	$E^{\circ\prime} = -0.48$
$2H^+ + 2e^- \rightarrow H_2$	$E^{\circ\prime} = -0.41$
$CO_2 + 6H^+ + 6e^- \rightarrow CH_3OH + H_2O$	$E^{\circ\prime} = -0.38$
$CO_2 + 8H^+ + 8e^- \rightarrow CH_4 + 2H_2O$	$E^{\circ\prime} = -0.24$
$N_2 + 5H^+ + 4e^- \rightarrow N_2H_5^+$	$E^{\circ} = -0.23$[a]
$N_2 + 8H^+ + 6e^- \rightarrow 2NH_4^+$	$E^{\circ} = +0.28$[a]
$O_2 + 4H^+ + 4e^- \rightarrow 2H_2O$	$E^{\circ\prime} = +0.81$
$HOO^{\bullet} + 3H^+ + 3e^- \rightarrow 2H_2O$	$E^{\circ\prime} = +1.26$
$HOOH + 2H^+ + 2e^- \rightarrow 2H_2O$	$E^{\circ\prime} = +1.37$
$HO^{\bullet} + H^+ + e^- \rightarrow H_2O$	$E^{\circ\prime} = +2.39$

[a] In these selected examples, where the chemical form of the product depends on the pH of the solution, standard reduction potentials (at pH 0) are reported instead of formal potentials (at pH 7). [b] Values are taken from refs 82, 84, 85, and 87.

4. FROM ENZYMES TO HUMAN-ENGINEERED CATALYSTS

Nature employs a myriad of enzymes for catalyzing various redox half-reactions including oxygen evolution, hydrogen evolution, carbon dioxide reduction, nitrogen reduction, and oxygen reduction reactions.[88−92] These enzymes feature active sites containing earth-abundant metal centers coordinated to soft-material frameworks (in the case of proteins, amino acid residues), which are proposed to provide primary, secondary, and further extended coordination environments that promote effective catalysis.[90,93−96] In this context, the three-dimensional chemical environments of enzymes are the products of four billion years of fierce evolution that have amplified their catalytic activity and selectivity by promoting favorable binding of substrates, selective formation of transition states, stabilization of intermediates, favorable release of products, and tuning as well as leveling of the redox potentials encountered across a reaction coordinate.[94] In one example of redox tuning, the metal centers of Fe-containing complexes in biological assemblies span over a 1 V range in their midpoint potential (Figure 4).[97−101]

The favorable properties of enzymes have made them targets for integration with solid-state electrode materials, and the process of mediating current flow between biological complexes and conductive surfaces has led to applications in sensor technologies, fuel cells, and electrocatalysis.[92,102−108] However, in the context of STF technologies, the relatively large molecular footprint and fragility of enzymes restrict several industrial applications. As an example, one mole of *D. desulfuricans* hydrogenase enzyme, which can produce 9000 hydrogen molecules per second per enzyme,[109] could fill the airship *Graf Zeppelin* in ~10 min or the main liquid-hydrogen tank of a space shuttle in ~2 h,[110] but given its molecular weight of ~53 kDa, one mole of hydrogenase equates to ~120 lb (~55 kg) of hydrogenase. Such characteristics have prompted researchers to investigate the design of more streamlined assemblies including the pursuit of both top-down and bottom-up strategies.[90,105,111]

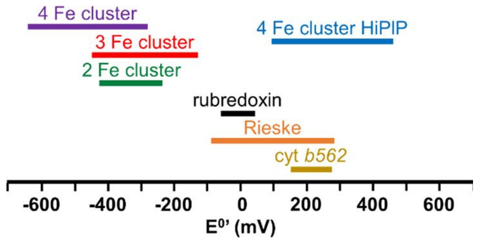

Figure 4. Redox span of iron complexes in biological systems.

The well-defined structures of enzymes have been modulated to investigate and better understand structure−function relationships. In addition to amino acid mutations within the biological toolbox, strategies to incorporate chemical functionalities not found in nature have also been explored including the use of unnatural amino acids, development of chimeric proteins, and de novo protein synthesis.[112−122] For example, synthetic functional models of the [Fe−Fe] site of hydrogenase have been effectively incorporated into the protein apo-HydA.[123] In a related vein, the rubredoxin scaffold has been used to coordinate Ni in place of its native Fe metal center, resulting in a hydrogen evolution catalyst that is oxygen tolerant.[124] The development of human-engineered molecular catalysts, which are often inspired by the active sites of enzymes, also continues to be an active area of research. In one particular example, Ni catalysts containing diphosphine ligands developed by DuBois and co-workers[125] have been studied as homogeneous electrocatalysts as well as components in heterogeneous electrocatalytic assemblies and in photoelectrosynthetic cells.[126−128] Shaw and co-workers have further shown that synthetically adding amino acids to the outer coordination sphere of this class of catalysts can significantly enhance their performance by reducing the overpotential (η) required to achieve a given rate of H_2 production, improving their solubility, and enhancing their stability during catalytic operation. These examples highlight promising features of extended three-dimensional environments for controlling the reactivity of catalytic sites.[129−132]

5. ARTIFICIAL PHOTOSYNTHESIS AND PHOTOELECTROSYNTHETIC CELLS

The construction of molecular-based light-harvesting complexes and electron donor−acceptors has provided fundamental insights regarding energy and charge transfer processes. This includes the fabrication of purely molecular assemblies[75,133−146] as well as molecular components interfaced with solid-state, inorganic materials to form dye-sensitized solar cells and dye-sensitized photoelectrosynthetic cells.[147−153] However, this review specifically focuses on photoelectrosynthetic cells featuring solid-state, visible-light-absorbing semiconductors (Figure 5) modified with molecular fuel-forming electrocatalysts.

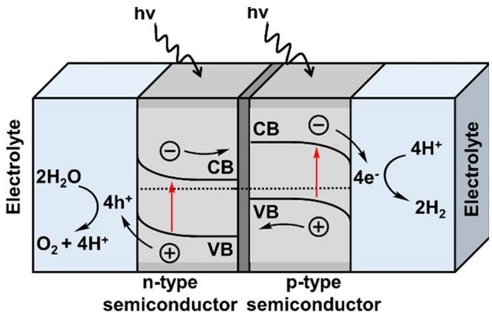

Figure 5. Diagrammatic scheme highlighting the light-induced electron- and proton-transfer reactions of a photoelectrochemical cell for solar water splitting. Minority charge carriers generated upon illumination (holes in the n-type semiconductor photoanode and electrons in the p-type semiconductor photocathode) are driven to the semiconductor/electrolyte solution interface.

The current density, J, produced upon illumination of a photoelectrode can be described according to eq 8:

$$J = EQE \times \frac{q_{\mathrm{p}}}{A} \times q \tag{8}$$

where EQE is the external quantum efficiency (as defined in eq 3a), q_{p}/A is the photon flux per geometric area incident on a light-absorber surface, and q is the charge of an electron ($1.602176634 \times 10^{-19}$ C).[154] For semiconductors, the spectral range of photons that can be absorbed is limited by their band gaps, which is the energy difference between the valence and conduction bands (E_{VB} and E_{CB}). In addition, not all photons with sufficient energy will be absorbed, as Φ_{abs} is dependent on the optical properties of a semiconductor and can be negatively affected by losses arising from transmission and reflection.[155,156]

Engineering of nanostructured semiconductor materials, including the synthesis of nanowire composites, can mitigate reflective losses and improve light-trapping effects.[157,158] For example, pillared nanowire arrangements have relatively long dimensions for effectively absorbing light but also have relatively short (radial) dimensions for diffusing carriers. The minority charge carrier diffusion length (L), which defines the average distance minority charge carriers (i.e., holes in n-type semiconductor photoanodes and electrons in p-type semiconductor photocathodes)[159,160] travel before recombination occurs, is described via eq 9:[160,161]

$$L = \sqrt{\frac{k_{\mathrm{B}} T \mu \tau}{q}} \tag{9}$$

where μ is the minority-carrier mobility, and τ is the minority carrier average lifetime. For planar semiconductors, if L is short relative to the absorption depth of light, Φ_{sep} will be negatively affected.

Upon contact of a semiconductor with a liquid, a semiconductor|liquid junction is formed, and the difference in potential between the semiconductor Fermi level (E_{F}) (which describes the thermodynamic occupancy of all electronic states within the semiconductor band gap and is the energy level for which the occupational probability for an electron or hole is 50% under thermal equilibrium conditions)[162] and the potential of the liquid solution (which is defined by the Nernst equation and the concentrations of reduced and oxidized species) must equilibrate. This equilibration process occurs via an exchange of carriers across the resulting interface until the potential of the semiconductor and solution are the same and equilibrium is established.[160] In the case of p-type semiconductors, the energetic positioning of the E_{F}, which is relatively closer to the E_{VB} rather than the E_{CB}, causes the material to behave like an anode in the dark. Thus, equilibrium between E_{F} and the solution potential results in the net transfer of holes from the semiconductor to the solution (Figure 6a,b).[160,163] This movement of charge across

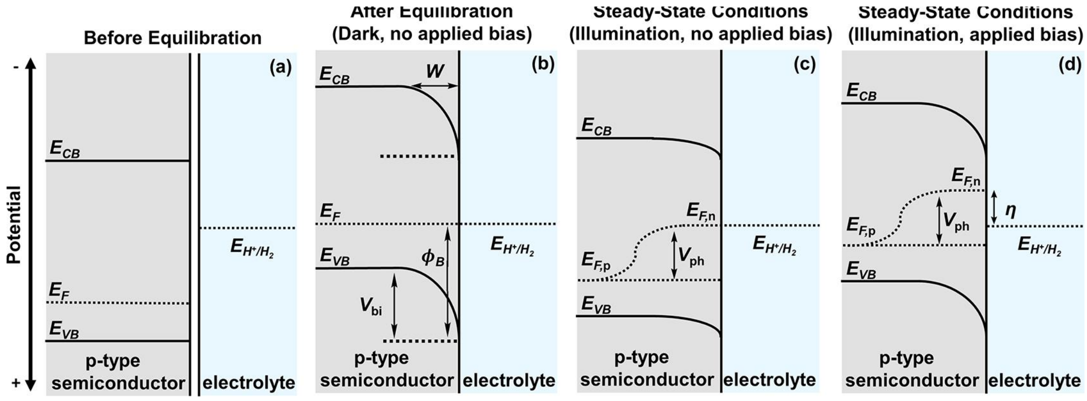

Figure 6. Illustration of a p-type semiconductor (a) before equilibration, (b) after equilibration with an electrolyte in the dark, (c) under steady-state illumination without an applied potential, and (d) under steady-state illumination with an applied potential. E_{F} is the Fermi level, $E_{\mathrm{F,n}}$ is the electron quasi-Fermi level, $E_{\mathrm{F,p}}$ is the hole quasi-Fermi level, E_{CB} is the conduction band-edge potential and E_{VB} is the valence band-edge potential, $E_{\mathrm{H^+/H_2}}$ is the redox potential of the $\mathrm{H^+/H_2}$ couple, W is the width of the space-charge region, V_{ph} is the photovoltage, V_{bi} is the built-in potential of the space-charge region, and η is the overpotential. The barrier height, ϕ_{B}, is the maximum internal energy that can be extracted from an electron−hole pair and is equal to the difference between the solution potential (in this case $E_{\mathrm{H^+/H_2}}$) and E_{VB}. In general, a thermodynamic requirement for driving solar-fuel forming reactions (the hydrogen evolution reaction (HER) in this figure) requires the electrochemical potential of the electrons (as determined by the quasi-Fermi level ($E_{\mathrm{F,n}}$) when there is direct contact between the semiconductor and electrolyte) to be negative of the corresponding solution potential ($E^{\circ\prime}$ or $E_{\mathrm{H^+/H_2}}$ in this figure).

the semiconductor|liquid interface yields a difference in potential within the semiconductor and a built-in voltage (V_{bi}). For a p-type semiconductor, this potential difference is manifested as a 'downward' bending (Figure 6b,c) of the E_{CB} and E_{VB} due to the net removal of holes from the semiconductor and the concomitant 'drop' in electric field intensity within the semiconductor. The electric field is a region surrounding a charge that exerts electrostatic force on other charges, and the strength of an electric field at any point in space is called the electric field intensity ($\vec{E}$). $\vec{E}$ produced by a point charge (Q) at any distance away (r) can be quantified as shown in eq 10a, where ε_0 is the permittivity of free space and $\hat{r}$ is the unit vector from one particle to the other. $\vec{E}$ is a vector field, and the force ($\vec{F}$) that a unit charge (q) would experience is determined as shown in eq 10b:

$$\vec{E} = \frac{Q}{4\pi\varepsilon_0 r^2}\hat{r} \quad (10a)$$

$$\vec{F} = q\vec{E} \quad (10b)$$

Following equilibration of potentials between a p-type semiconductor and liquid in the absence of light, the excess of negative charges arising from ionized dopants within the p-type semiconductor are distributed over the space-charge region as described in eq 11:[164]

$$W = \sqrt{\frac{2\varepsilon\varepsilon_0 V_{bi}}{qN_D}} \quad (11)$$

where the width of the space-charge region (W) depends on the static dielectric constant of the material (ε), V_{bi}, and doping density (N_D). In general, a lower concentration of dopants will result in a larger W, as charges must be extracted from deeper within the semiconductor to establish equilibrium between the solution and semiconductor potentials. The resulting band bending favors electron transfer from the semiconductor to electron-accepting species in the solution when the semiconductor is illuminated.[160] Thus, a solution-equilibrated p-type semiconductor behaves like a cathode when illuminated and is referred to as a photocathode even though it behaves as an anode when equilibrating with the solution in the dark. In the case of an n-type semiconductor, where the energetic positioning of E_F is relatively closer to the E_{CB} rather than the E_{VB}, equilibration with a solution involves the net transfer of electrons from the semiconductor to the solution, resulting in an upward bending of the E_{CB} and E_{VB} (see Figure 5). By extension, a solution-equilibrated n-type semiconductor behaves like an anode when illuminated and is referred to as a photoanode even though it behaves as a cathode when equilibrating with the solution in the dark.

In contrast to the multistep redox events used to spatially separate charges in photosynthetic organisms (Figure 2), charge separation in solid-state semiconducting materials is driven by differences in $\vec{E}$ formed within the semiconductor (Figure 6b).[160,164,165] Given the initial difference in potential between the E_F of a semiconductor and redox potential of an electrolyte solution is typically on the order of an electronvolt, and W is on the order of hundreds of nanometers, the electric field developed within a semiconductor can be on the order of 10^5 V cm^{-1}.[160,163] Because of these relatively high electric field strengths, recombination in the space-charge region is orders of magnitude slower than in the bulk semiconductor, and charge carriers, which typically have mobilities of 10−1000 cm^2 V^{-1} s^{-1}, are readily separated.[160] However, such band-bending effects will not arise in nanostructured materials if the dimensions of the semiconductor are not large enough to develop a substantial space-charge region.[166]

Under illumination, the E_F of a semiconductor is split into two quasi-Fermi levels associated with nonequilibrium steady-state electron, $E_{F,n}$, and hole, $E_{F,p}$, populations. This splitting gives rise to a corresponding photovoltage, V_{ph}, and a decrease in the degree of band bending (Figure 6c).[160] The maximum V_{ph} of a semiconductor is smaller than the band gap due to the intrinsic bulk recombination, and the presence of surface states can further reduce V_{ph} by lowering the barrier height (ϕ_B) (which is the maximum internal energy that can be extracted from electron−hole pairs).[167] Forward electrochemical biasing of the semiconductor enhances the band bending and the fraction of minority-carrier electrons reaching the semiconductor surface. For an ideal p-type semiconductor,[168,169] the driving force for the cathodic reaction at the semiconductor|liquid interface is equal to the difference between $E_{F,n}$ at the surface and the thermodynamic potential of the solution reaction under the conditions of operation. For an ideal n-type semiconductor,[168,169] the driving force for the anodic reaction at the semiconductor|liquid interface is equal to the difference between $E_{F,p}$ at the surface and the thermodynamic potential of the solution reaction under the conditions of operation.[159] In both cases, the position of the quasi-Fermi level associated with the minority carriers is dependent on the applied potential (V) as well as the illumination intensity (which also affects the value of V_{ph}). In the example of a p-type semiconductor, as $E_{F,n}$ changes, the associated rate constant for electron transfer remains constant and is independent of V and illumination intensity.[159,170] Thus, for a well-behaved semiconductor electrode, the dependence of J (a reaction rate) on the electrochemical potential (a driving force) is established by changing the degree of band bending within the semiconductor, which in turn controls the steady-state concentration of minority charge carriers reaching the electrode surface.[168,169] This is in stark contrast to electrocatalytic reactions involving conducting metallic electrodes, where the potential of the electrode is defined by a single E_F and differences in V appear mostly outside the electrode in the solution phase. Thus, in accordance with Marcus−Hush−Levich theory and Butler−Volmer kinetics,[60−64] enhancement of electrocatalytic reaction rates upon increasing the η is due to the driving-force-dependent nature of the charge-transfer rate constant, not changes in the surface concentrations of charge carriers.

The current density produced by a semiconductor|liquid junction under illumination has been modeled by Gärtner.[171,172] For p-type semiconductors, which are a focus of this review, the minority carrier current density (J_g) is obtained by summing the electron current density at the depletion edge (J_w) (i.e., the boundary between the space-charge region and bulk semiconductor) and the electron photocurrent density in the space-charge region (J_{SCR}) when recombination effects within the space-charge region and at the interface are neglected (eqs 12a−12c):

$$J_g = J_w + J_{SCR} \quad (12a)$$

$$J_w = J_0\left[\frac{n_w}{n_0} - 1\right] - qI_0\alpha L\frac{e^{(-\alpha W)}}{1 + \alpha L} \quad (12b)$$

$$J_{\mathrm{SCR}} = -qI_0(1 - e^{-\alpha W}) \tag{12c}$$

In eqs 12a−12c, n_w is the electron density at the depletion edge, n_0 is the electron density in the bulk, q is the unit charge, I_0 is the incident photon flux on the semiconductor after correcting for interface reflection and electrolyte absorption losses, α is the absorption coefficient of the photoelectrode, and J_0 is the saturation current density. As the electron concentration in the bulk (n_0) is relatively small, $|J_w|$ is limited to J_0 as shown in eq 13 in the absence of illumination, even at large applied V_b:

$$|J_w| \approx J_0 = \frac{qn_0L}{\tau} \tag{13}$$

where τ is the minority carrier average lifetime. Under the boundary condition used in the Gärtner model, where $n_w = 0$ at the depletion edge, J_g can be expressed as shown in eq 14:

$$J_g = -J_0 - qI_0\left(1 - \frac{e^{-\alpha W}}{1 + \alpha L}\right) \tag{14}$$

In this form, the equation addresses monochromatic illumination conditions. To address broad-band illumination conditions, integration can be applied over a selected spectral range. In summary, the Gärtner model gives a relatively simplified description of the current density produced upon illumination of a photoelectrode where carrier recombination within the space-charge region is not accounted for. Thus, the predicted current can deviate from experimental results under conditions where the band bending is relatively low and recombination rates are relatively high.[164]

The Gärtner model was further extended by Reichman[172] to account for contributions from recombination in the space-charge region. In this revised model, the current density due to holes (J_p) and electrons (J_n) is described in terms of the surface concentrations of charge carriers (p_s and n_s) relative to their values at equilibrium (p_{s0} and n_{s0}), meaning the surface concentrations of charge carriers when no net current flows, as expressed in eqs 15a and 15b, respectively:

$$J_p = J_p^{\,0}\left[\frac{p_s}{p_{s0}} - 1\right] \tag{15a}$$

$$J_n = -J_n^{\,0}\left[\frac{n_s}{n_{s0}} - 1\right] \tag{15b}$$

where $J_p^{\,0}$ and $J_n^{\,0}$ are the exchange current densities (i.e., the current densities at equilibrium where no net current flows) for holes and electrons, respectively. For a p-type semiconductor under illumination, the surface concentration of holes (defined as p_s/p_{s0}) is a function of V and is independent of the light intensity (eq 16a).[172] Conversely, the surface concentration of electrons (n_s/n_{s0}) is a function of V as well as the illumination intensity and is dependent on recombination losses in the space-charge region (K_r) (eqs 16b−16e):

$$\frac{p_s}{p_{s0}} = e^{qV/k_BT} \tag{16a}$$

$$\frac{n_s}{n_{s0}} = \left(\frac{-K_r + (K_r^{\,2} + 4AB)^{1/2}}{2A}\right)^2 \tag{16b}$$

$$K_r = \frac{\pi k_B T n_i W}{4\tau(V_{bi} - V)} \times e^{qV/2k_BT} \tag{16c}$$

$$A = J_n^{\,0} + J_0 \times e^{qV/k_BT} \tag{16d}$$

$$B = J_n^{\,0} - J_g \tag{16e}$$

where n_i is the intrinsic carrier concentration and V is the applied potential.

6. MOLECULAR-CATALYST-MODIFIED SEMICONDUCTORS

The immobilization of molecular electrocatalysts to a semiconductor surface results in formation of semiconductor|catalyst interfaces. When these modified semiconductors are immersed in liquids, semiconductor|catalyst|liquid junctions are formed. Application of relatively thick catalytic films (i.e., those that are ion-impermeable and can be formed by metallic electrocatalytic coatings) give rise to 'buried' junctions. Under these conditions, the catalytic processes occurring at the catalyst|liquid interface are physically separated from the V_{ph} generation and charge separation processes occurring at the semiconductor|catalyst interface.[27,44] Unlike semiconductor|liquid junctions, the E_{CB} and E_{VB} edges associated with 'buried' junctions are not required to straddle the thermodynamic potentials of the redox half-reactions under the conditions of operation because the V_{ph} are not fixed relative to a material-specific flatband potential (V_{flatband}).[44,160] Alternatively, catalytic surface coatings that are ion-permeable, including molecular catalyst layers and coatings of porous oxide materials, form interfaces that have been referred to as 'adaptive' junctions.[173,174] Because the electrocatalyst layer (molecular or other) is permeable to the electrolyte solution, the semiconductor|catalyst|solution system needs to be treated as a single element, and the maximum internal energy that can be extracted from electron−hole pairs (i.e., the barrier height (ϕ_B)) increases as a function of the catalyst redox states.[27] Thus, in comparison to nonporous metallic electrocatalyst coatings, the 'adaptive' junctions do not require a potential drop across the electrocatalyst|liquid interface as the free motion of ions from the electrolyte solution enables the potential drop to occur mostly inside the semiconductor across the space-charge region. For this reason, the E_{CB} and E_{VB} band edge positions associated with adaptive junctions must straddle the thermodynamic potentials of the redox half-reactions occurring in the liquid phase.

In comparison with PEC charge-transfer reactions occurring at semiconductor|liquid junctions, relatively few models have been developed to describe photoelectrosynthetic reactions involving molecular-catalyst-modified semiconductors.[44,159,164,168,170−172,175−184] In one example, the current−potential responses of molecular-catalyst-modified n-type semiconductors were simulated by modeling the catalyst-solution currents (eq 17a) and semiconductor|catalyst currents (eq 17b):[179]

$$J_{\mathrm{cat}} = k_{\mathrm{cat}}C^+ - k_{-\mathrm{cat}}C = k_{\mathrm{cat}}\hat{C}\frac{e^{qV_{\mathrm{cat}}/k_BT} - 1}{e^{qV_{\mathrm{cat}}/k_BT} + K} \tag{17a}$$

$$J_{\mathrm{jxn}} = (k_{\mathrm{ht}}p_sC - k_{-\mathrm{ht}}\{p_s\}C^+) - (k_{\mathrm{et}}n_sC^+ - k_{-\mathrm{et}}\{n_s\}C) \tag{17b}$$

In eq 17a, J_{cat} is the catalyst solution current density, k_{cat} and k_{-cat} are forward and reverse rate constants associated with chemical catalysis (with units of mA cm), $\hat{C}$, C^+, and C are the total, oxidized (activated), and unoxidized catalyst site concentrations, respectively, qV_{cat} is the chemical potential difference across the catalyst layer (qV_{cat} = potential of the solution − potential of the catalyst), and K is the equilibrium constant for the reaction ($K = k_{cat}/k_{-cat}$). In eq 17b, J_{jxn} is the semiconductor-catalyst current density, k_{ht} and k_{-ht} are the forward and reverse rate constants for hole transfer (with units of mA cm^4), and k_{et} and k_{-et} are the forward and reverse rate constants for electron transfer (with units of mA cm^4). This model shows that when the value of k_{cat} is relatively small and V is much greater than the open-circuit potential (V_{oc}) (i.e., the potential where there is no net current flow under illumination),[160] the concentration of surface-immobilized active catalyst species approaches the total concentration of surface-immobilized catalyst species. Under these conditions, the current is limited by the rate at which the activated catalyst can reduce or oxidize the substrate. In contrast, when k_{cat} is relatively large, the current−potential response can be effectively modeled using the current−potential response of the photodiode.[179]

In another example, experimental results using a molecular-catalyst-modified p-type semiconductor (a Co porphyrin-polypyridyl-modified p-type GaP working electrode) were used to model current−potential responses and develop a framework for extracting kinetic and thermodynamic benchmarking parameters associated with immobilized catalysts. The current response (eq 18a) was modeled by applying either steady-state (eq 18b) or pre-equilibrium (eq 18c) approximations to describe the fraction of surface-immobilized catalysts present in their activated form under varying applied V_b and intensities of simulated solar illumination:[181]

$$J = \frac{nF}{FE} \times k_{cat}\Gamma_{C'} \tag{18a}$$

$$J = \frac{nF}{FE} \times \frac{k_{cat}\Gamma_{C_T} n_s}{\frac{k_{-et} + k_{cat}}{k_{et}} + n_s} \tag{18b}$$

$$J = \frac{nF}{FE} \times \frac{k_{cat}\Gamma_{C_T} n_s}{K^{-1} + n_s} \tag{18c}$$

In these equations, J is the current density, n is the number of electrons required for the chemical transformation, F is the Faraday constant, FE is the faradaic efficiency, k_{cat} is a rate constant (with units of s^{-1}), k_{et} and k_{-et} are the forward and reverse rate constants for electron transfer between the semiconductor and catalyst layer (with units of cm^2 mol^{-1} s^{-1} and s^{-1}, respectively), n_s represents the surface electron concentration under steady-state illumination, K^{-1} is an equilibrium constant equal to the ratio of the forward and reverse rate constants for electron transfer from the semiconductor (k_{-et}/k_{et}), and Γ_{C_T} and $\Gamma_{C'}$ are the per geometric area surface densities of total and activated catalysts, respectively. These rate laws are similar in form to those used in the Michaelis−Menten model describing the reaction velocities of enzymes after applying steady-state (eq 19a) or pre-equilibrium approximations (eq 19b):

$$\upsilon = \frac{V_{max}[S]}{K_M + [S]} \tag{19a}$$

$$\upsilon = \frac{V_{max}[S]}{K_d + [S]} \tag{19b}$$

where υ is the velocity, or rate of the enzymatic reaction, V_{max} is the maximum reaction velocity (which is the product of k_{cat} and the initial/total concentration of enzyme $[E_T]$), $[S]$ is the concentration of substrate, K_d is dissociation constant for the enzyme−substrate complex defined as k_r/k_f (where k_f and k_r are the forward and the reverse rate constants describing the binding and unbinding of the substrate to the enzyme, respectively), and K_M is the Michaelis constant defined as $(k_r + k_{cat})/k_f$.

In the Michaelis−Menten model, the term K_M represents the steady-state concentration of substrate required to achieve half the maximum velocity of an enzyme. Conversely, in the molecular-catalyst-modified semiconductor model, the analogous term, $(k_{-et} + k_{cat})/k_{et}$, represents the steady-state concentration of minority carriers (electrons) at a semiconductor surface required to activate half of the immobilized catalysts.[181] This parameter can be viewed as a PEC counterpart of the parameter $E_{cat/2}$ that is used as a benchmark in homogeneous electrocatalysis and represents the potential required to activate half of the catalyst at the electrode surface and thus achieve half the maximum TOF. In a related vein, the K^{-1} term in eq 18c (an equilibrium constant describing the ratio of reverse and forward electron transfer rate constants under pre-equilibrium conditions) has conceptual parallels with the K_d term in eq 19b (an equilibrium constant describing dissociation of the enzyme substrate complex under pre-equilibrium conditions).

7. EXAMPLES INVOLVING SOLID-STATE PHOTOCATHODES MODIFIED WITH MOLECULAR CATALYSTS

7.1. Photoelectrochemical H_2 Production

Examples of molecular-modified semiconductors for applications involving hydrogen (H_2) evolution are found in work conducted in the 1980s. In an example by Mueller-Westerhoff and co-workers,[185] polymeric materials prepared using methylferrocenophane (MeFCP) and poly(chloromethyl)-styrene (MePS) in a solution of tetrahydrofuran (THF) were deposited as a film onto the (100) or (111) faces of p-type Si electrodes (0.16 cm^2) at a concentration of 2 M, forming Si|MeFCP-MePS electrodes (Figure 7a). In addition to serving as a medium for immobilizing the molecular components at relatively high concentrations as compared to catalysts dissolved in solution, the authors indicated the polymer also provided protection of the semiconductor surface from photocorrosion, a strategy that received increased attention in following years.[186] When exposed to relatively strong acidic conditions (HBF_3OH), the Si|MeFCP-MePS electrodes were proposed to coordinate two protons, forming a dicationic species that liberated H_2 upon reduction. The Si|MeFCP-MePS electrodes were photoelectrochemically characterized utilizing a two-electrode configuration with a Pt anode in neat HBF_3OH under 870 mW cm^{-2} illumination via a Xe light source. The assembly was photoactive for H_2 evolution with stable performance over 5 days. The Si|MeFCP-MePS photocathode reached a saturating photocurrent of 37 mA

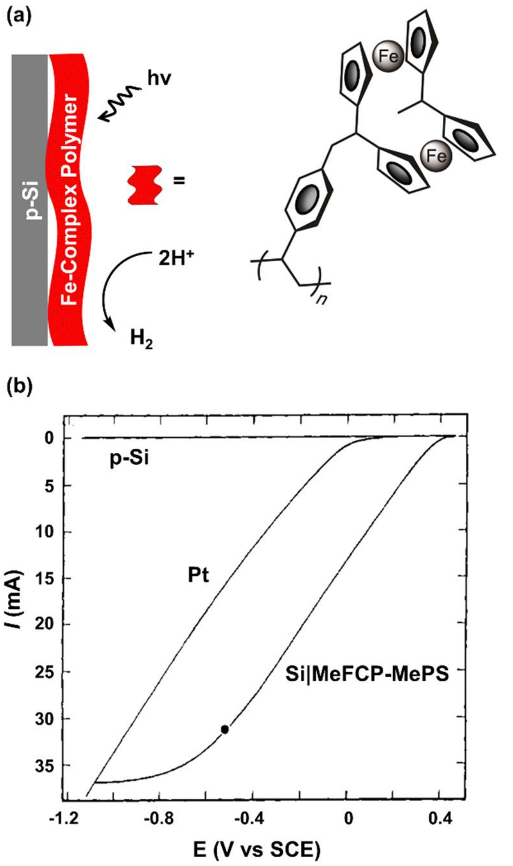

Figure 7. (a) Schematic representation of the methyl-ferrocenophane polymer film on Si. (b) Linear sweep voltammograms of p-Si electrodes with and without the presence of the Fe-complex polymer, as well as a Pt cathode, recorded using a two-electrode configuration (Pt anode) in neat BF_3OH under 870 mW cm^{-2} illumination, at a scan rate of 50 mV s^{-1}. Adapted with permission from ref 185. Copyright 1984 American Chemical Society.

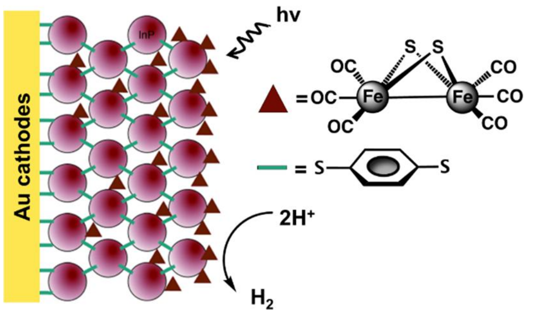

Figure 8. Schematic representation of $[Fe_2S_2(CO)_6]$-modified InP nanocrystal arrays. Adapted with permission from ref 187. Copyright 2010 Wiley-VCH Verlag GmbH & Co.

(231 mA cm^{-2}) when polarized at −1.1 V vs the saturated calomel electrode (SCE) (Figure 7b) and achieved a current of 26 mA (162.5 mA cm^{-2}) when polarized at −0.35 V vs SCE, a potential 0.45 V more positive than that required for a Pt electrode to achieve an equivalent activity (−0.80 V vs SCE). In addition, the polymer-coated Si photocathodes were active for H_2 production in 1 M $HClO_4$, achieving a current of 2 mA (12.5 mA cm^{-2}) when polarized at potentials ~0.25 V positive of the HER equilibrium potential.

In work by Nann, Pickett, and co-workers, H_2-evolving iron-sulfur electrocatalysts, $[Fe_2S_2(CO)_6]$, selected because they contain only earth-abundant elements and mimic structural and functional aspects of the Fe−Fe active site of naturally occurring hydrogenase, were interfaced with indium phosphide (InP) nanocrystals (Figure 8).[187] The molecular array was formed by first adsorbing a 1,4-benzenedithiol layer onto a gold electrode, which enabled the binding of conducting InP nanocrystals (mean diameter of ~5 nm). Alternating exposure to the dithiol solution and an InP nanocrystal solution resulted in a layer-by-layer array. The InP-modified gold electrodes were then immersed into a solution containing $[Fe_2S_2(CO)_6]$, resulting in formation of an inorganic light-harvesting nano-array containing intercalated and adsorbed $[Fe_2S_2(CO)_6]$ clusters. These assemblies were characterized using photoluminescence and diffuse reflectance Fourier-transform infrared (FTIR) spectroscopies to confirm incorporation of the molecular components. The presence of $[Fe_2S_2(CO)_6]$ in these constructs quenched the luminescence of InP, indicating possible charge transfer, nonradiative energy transfer, or defect sites in the InP nanocrystals following immobilization of the catalysts. In addition, structural characterization via FTIR spectra showed an absorption feature assigned to a carbonyl stretching mode of the $[Fe_2S_2(CO)_6]$ species at frequencies similar to those found in FTIR spectra of the homogeneous catalyst dissolved in solution, providing further evidence of surface functionalization. The resulting photocathodes evolved H_2 with a *FE* of 60% and achieved a *J* on the order of 0.1 μA cm^{-2} for at least 1 h without detectable degradation when polarized at a V_b = −0.40 V vs a silver/silver chloride (Ag/AgCl) reference electrode (+0.22 V vs the reversible hydrogen electrode (RHE)[188]) in pH neutral aqueous conditions (0.1 M $NaBF_4$) under illumination with a 395 nm LED.

The sulfur-containing centers of nature's enzymes for H_2 evolution also served as a design inspiration for molecular clusters used by Chorkendorff and co-workers. In this work, nonwater-soluble trinuclear molybdenum cluster salts (Mo_3S_4), examples of cubane-type, molecular metal-sulfide clusters, building blocks central to the cofactors of enzymes, were dropcasted onto hydrogen-terminated planar or pillar-structured p-Si(100) (Figure 9a).[189] Si, with a band gap of 1.2 eV, has the ability to capture photons in the red portion of the solar spectrum. Given their relatively large cross-sections for absorbing light and short, radial minority-carrier transport distances, pillared structures facilitate effective capturing of photons and photocurrent collection, and enable a larger surface area for loading of catalysts. Structural characterization of the functionalized surfaces included use of X-ray photoelectron spectroscopy (XPS), which indicated successful deposition of the clusters. However, XPS analysis performed following PEC experiments indicated dissociation of a relatively large fraction of the clusters from the surface. The Mo_3S_4-modified planar-Si electrodes (planar-Si|Mo_3S_4) were photoelectrochemically characterized in a 1 M aqueous $HClO_4$ solution under illumination with a Xe lamp coupled with an AM 1.5 G filter and a long-pass filter so that samples were illuminated with photons ranging from 620 to 1050 nm (28.3 mW cm^{-2}). Planar-Si|Mo_3S_4 electrodes initially coated with Mo_3S_4 clusters at a loading of 2 nmol cm^{-2} were found to generate H_2 at a *J* = 8 mA cm^{-2} when polarized at 0 V vs RHE (Figure 9b). The loading of Mo_3S_4 clusters determined via analysis of the modified-Si electrodes following PEC operation was 2.6×10^{-13} Mo_3S_4 clusters cm^{-2}. This loading was then used to determine a corresponding TOF of 960 s^{-1} per cluster.

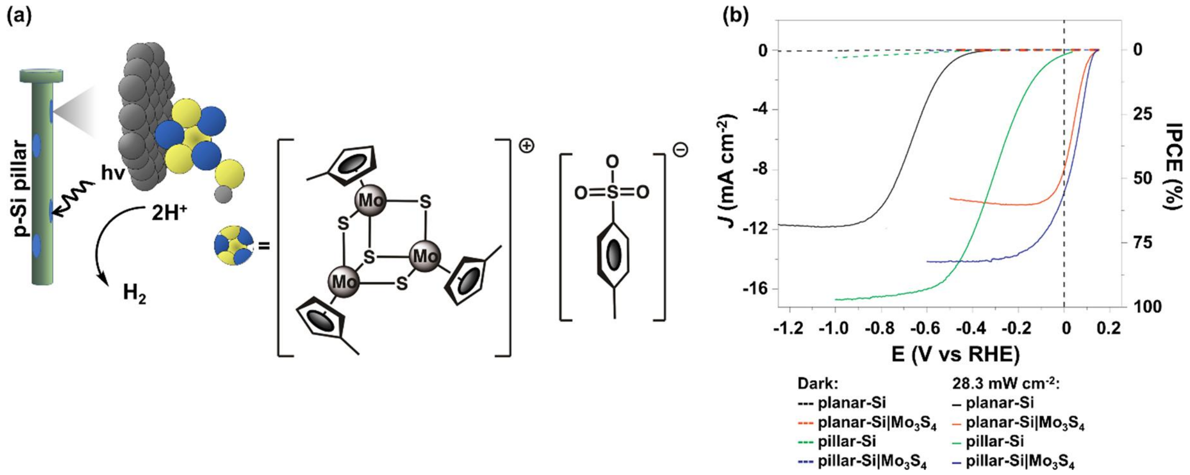

Figure 9. (a) Schematic representation of the Si pillar modified with the adsorbed [Mo_3S_4] cluster. (b) Linear sweep voltammograms of planar-p-Si (black), planar-p-Si|Mo_3S_4 (red), pillar-p-Si (green), and pillar-p-Si|Mo_3S_4 (blue) electrodes recorded in 1 M aqueous $HClO_4$ solution in the dark (dashed lines) or under 28.3 mW cm^{-2} illumination (solid lines). The calculated photon-to-current conversion efficiency is included on the right-coordinate axis. Adapted from ref 189. Copyright 2011 Springer.

Mo_3S_4 clusters were also dropcasted onto nanopillar-structured Si electrodes (pillar-Si|Mo_3S_4) prepared via photolithography, where the electrodes provided a higher surface area in comparison to planar Si electrodes. The pillar-Si|Mo_3S_4 photoelectrodes achieved a J = 9 mA cm^{-2} with unity *FE* for H_2 production when studied under the same illumination, pH, and polarization conditions used to study the planar-Si|Mo_3S_4 assemblies (Figure 9b). Controlled-potential polarization using the pillar-Si|Mo_3S_4 samples polarized at 0 V vs RHE indicated that J remained stable over 1 h with the catalyst operating at an apparent TOF of 65 s^{-1}.

A Ni bisdiphosphine-based functional mimic of the active site of Ni-Fe hydrogenase (a NiP_2N_2 DuBois-type catalyst) was immobilized onto p-type GaP(100) and Si(111) surfaces (Figure 10) by Moore, Sharp, and co-workers.[190] Bisdiphosphines provide a soft ligand environment for stabilizing low-valent Ni during the catalytic cycle, and the GaP and Si conduction bands are negative of the H^+/H_2 redox couple. In a three-step method, UV-induced immobilization of *N*-allyl-2,2,2-trifluoro-acetamide onto the semiconductor surfaces was followed by chemical unmasking of the amines and exposure to the Ni catalysts bearing an activated ester. Successful grafting of the Ni catalyst was confirmed via grazing-angle total reflection Fourier-transform infrared (GATR-FTIR) and XP spectroscopies. On the basis of the latter analysis, the authors proposed that immobilization of the Ni catalyst likely occurred through direct Si−C bonds on Si surfaces and through a bridging oxide layer on GaP surfaces.

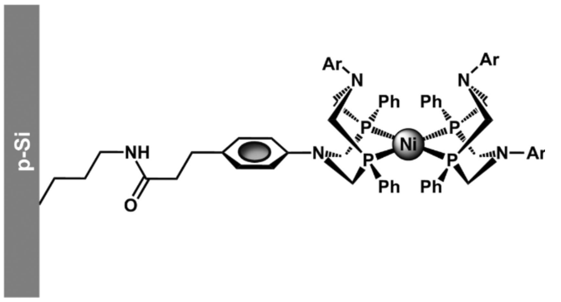

Figure 10. Schematic representation of the Ni catalyst on p-Si. Adapted with permission from ref 190. Copyright 2013 American Chemical Society.

In subsequent work by Yano, Sharp, Moore, and co-workers, the UV-induced immobilization of olefins was used to polymerize 4-vinylpyridine onto p-type GaP, providing surface-attached pyridyl ligands for subsequent assembly of cobaloxime-type catalysts.[191] In these constructs, the polypyridyl (PPy) coating on the GaP surface afforded protection against oxide layer formation, likely by restricting access to GaP(100) surface sites, and provided functional groups for assembly of the cobalt-containing molecular catalysts to form the catalyst-modified semiconductor (GaP|PPy|Cobaloxime) (Figure 11a). This strategy allows for the use of a broad range of vinyl monomers with a variety of functional groups, enabling control over surface loading capacity and attachment stability. The constructs were structurally characterized using GATR-FTIR spectroscopy, XPS, X-ray absorption near edge structure spectroscopy (XANES), and ellipsometry. The GaP|PPy|Cobaloxime photocathodes achieved a J = 2.4 mA cm^{-2} when polarized at a potential 0.31 V positive of the H^+/H_2 equilibrium potential (+0.31 V vs RHE) in pH 7 buffered aqueous solutions (1 M phosphate buffer) under 100 mW cm^{-2} illumination using a Newport Oriel Apex illumination source. In addition, the *FE* as determined via gas chromatography (GC) was shown to be near unity.

Leveraging the surface-grafting chemistry of olefins on GaP semiconductors, Moore and co-workers showcased the modularity of this strategy by modifying the ligand environment of the immobilized catalysts, the structure of the intervening polymer, and the crystal orientation of the underpinning (semi)conductor surface used to prepare the assemblies. For example, GaP electrodes were prepared featuring surface-grafted PPy coatings modified with cobaloxime catalysts containing either a glyoximate capping group (GaP|PPy|Cobaloxime) (Figure 11a) or an analog featuring a boron difluoride moiety (GaP|PPy|Cobaloxime-BF_2) (Figure 11b).[192] The addition of the BF_2 moieties imparts stability under acidic conditions and tunes the catalytic redox features of cobaloximes to less negative values. For both constructs, successful surface attachment was confirmed via GATR-FTIR and XP spectroscopies, and PEC characterization of the

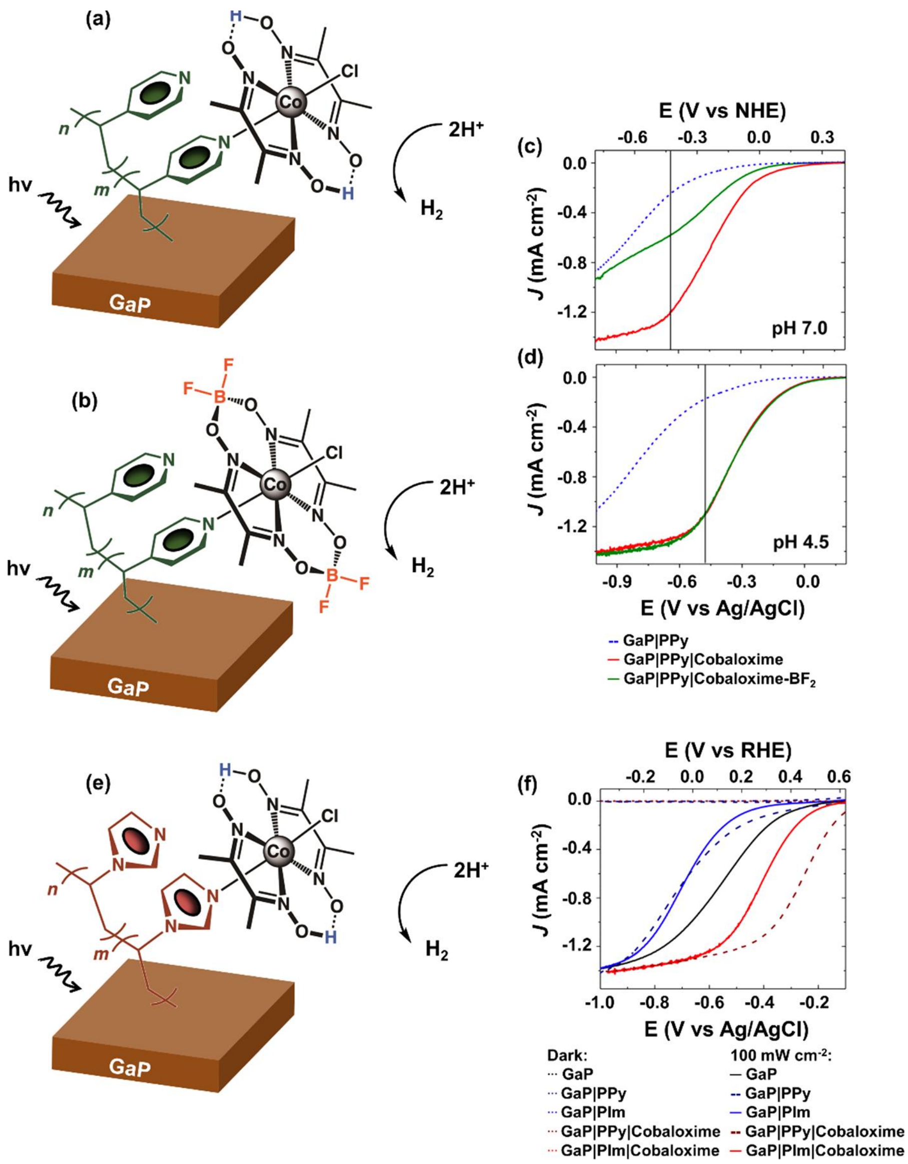

Figure 11. Schematic representation of the cobaloxime catalysts on (a, b) polypyridyl or (e) polyimidazole layers on GaP. (c) Linear sweep voltammograms of GaP|PPy (dashed blue), GaP|PPy|Cobaloxime (solid red), or GaP|PPy|Cobaloxime-BF_2 (solid green) electrodes recorded in 0.1 M phosphate buffer (pH 7) under 100 mW cm^{-2} illumination, at a scan rate of 100 mV s^{-1}. (d) Linear sweep voltammograms of GaP|PPy (dashed blue), GaP|PPy|Cobaloxime (solid red), or GaP|PPy|Cobaloxime-BF_2 (solid green) electrodes recorded in 0.1 M acetate buffer (pH 4.5) under 100 mW cm^{-2} illumination, at a scan rate of 100 mV s^{-1}. (f) Linear sweep voltammograms of GaP (black), GaP|PPy (dark blue), GaP|PIm (blue), GaP|PPy|Cobaloxime (dark red), and GaP|PIm|Cobaloxime (red) electrodes recorded in 0.1 M phosphate buffer (pH 7) in the dark (dotted lines) or under 100 mW cm^{-2} illumination (dashed and solid lines), at a scan rate of 100 mV s^{-1}. (a) Adapted with permission from ref 191. Copyright 2013 American Chemical Society. (b–d) Adapted with permission from ref 192. Copyright 2014 American Chemical Society. (e, f) Adapted with permission from ref 195. Copyright 2016 American Chemical Society.

modified GaP photoelectrodes was conducted in pH 7 (0.1 M phosphate buffer, Figure 11c) or pH 4.5 (0.1 M acetate buffer, Figure 11d) aqueous solutions under simulated AM 1.5 G illumination (100 mW cm^{-2}) using a Newport Oriel Apex light source. The pH response of the PEC activity was consistent with results obtained from electrochemical studies conducted using analogous nonsurface-attached catalysts dissolved in solution, meaning that a relatively lower pH was required to induce HER when using GaP|PPy|Cobaloxime-BF_2. These findings were attributed to a correlation between the $Co^{II/I}$ reduction potential and the basicity of Co^{I} species to form Co^{III} hydride species during the catalytic cycle[193,194] and show that incorporation of a cobaloxime with a ligand macrocycle that is modified at the molecular level affects the PEC response observed at the construct level.

Moore and co-workers have also shown that changing the polymeric interface from surface-grafted PPy to surface-grafted polyimidazole (PIm), while preserving the underpinning GaP substrate and use of immobilized cobaloxime-type catalysts (Figure 11e),[195] results in differences in the PEC activity measured in pH-neutral aqueous conditions (0.1 M phosphate buffer) under 100 mW cm^{-2} illumination using an AM 1.5 G filter and a Newport Oriel Apex illumination source. The cobaloxime-polyimidazole-modified photocathode (GaP|PIm|Cobaloxime) achieved a J = 1 mA cm^{-2} when polarized at +0.07 V vs RHE, a potential 0.17 V more negative than required for the GaP|PPy|Cobaloxime photocathode to achieve an equivalent activity (+0.24 V vs RHE) (Figure 11f). These results are consistent with the difference in reduction potentials measured in cyclic voltammograms recorded using the homogeneous, nonsurface-immobilized cobaloxime model compounds dissolved in organic solvents, where the $Co^{II/I}$ midpoint potential of the cobaloxime complex containing an axial pyridine ligand ($Co(dmgH)_2(Py)Cl$) was 60 mV more positive than the $Co^{II/I}$ couple of the cobaloxime complex containing an axial imidazole ligand ($Co(dmgH)_2(meIm)Cl$). For both heterogeneous assemblies, a near-unity *FE* was achieved, with a HER activity of 2.1 H_2 s^{-1} Co^{-1} for the GaP|PPy|Cobaloxime construct and 2.4 H_2 s^{-1} Co^{-1} for the GaP|PIm|Cobaloxime construct, when polarized at 0 V vs RHE. However, it was noted that the surface-grafted polymeric films differed in thickness (~10 nm PPy films and ~6 nm PIm films), total catalyst loading, and the pK_a of associated nitrogen sites, thus complicating comparisons of the two constructs based on differences in the coordination chemistry between the catalyst and polymer.

In addition to preparing surface-grafted polymer coatings on GaP(100) surfaces, which contain a mixed phase of atop Ga and P sites, Moore and co-workers also showed that UV-induced polymerization of vinylimidazole followed by immobilization of cobaloxime catalysts is applicable to both the (111)A and (111)B faces of GaP (which are composed predominantly of atop Ga or P sites, respectively) with little difference in the surface coverages as measured using ellipsometry, GATR-FTIR spectroscopy, and XPS.[196] Likewise, the GaP|PIm|Cobaloxime photocathodes constructed using either GaP (111)A or (111)B crystal faces exhibited similar PEC responses, yielding V_{oc} of +0.64 ± 0.02 and +0.65 ± 0.02 V vs RHE, respectively, and achieving $J = 0.89 \pm 0.02$ and 0.89 ± 0.03 mA cm^{-2}, respectively, when polarized at 0 V vs RHE in pH neutral (0.1 M phosphate, pH 7) aqueous conditions under AM 1.5 G illumination (100 mW cm^{-2} using Newport Oriel Apex illumination source equipped with an AM 1.5 G filter). These results illustrate the surface chemistry and PEC performance of the cobaloxime-polymer-modified GaP assemblies is not restricted to a single crystal face orientation, a feature that could be useful in interfacing molecular catalysts to nanostructured materials that terminate with a range of Miller indices. In addition, controlled-potential polarization performed at 0 V vs RHE using cobaloxime-polymer-modified GaP assemblies under the same illumination and electrolyte conditions previously mentioned indicated the associated *J* were relatively stable, with a decrease in activity of less than 1% over ~1 h of testing following an initial 5% loss during the first 5 min of the experiment. This initial loss was attributed to desorption of loosely bound catalysts. Combining results obtained from ellipsometry, XPS, and PEC characterization enabled estimation of a HER activity of 7000 H_2 h^{-1} Co^{-1} (1.94 H_2 s^{-1} Co^{-1}) with near-unity *FE*. The ability to functionalize both the Ga-rich (111)A and the P-rich (111)B faces, combined with the XPS evidence of an intervening ~2 nm thick oxide layer present on the polymer-functionalized samples, indicated the grafting chemistry on both crystal faces involved attachment to a relatively thin oxide layer. Prompted by these findings, the Moore group has also shown that related attachment chemistries can be extended to other oxide-coated materials, including transparent conducting oxides, which enabled direct measurements of the optical and electrochemical properties of cobaloxime and Co porphyrin catalysts immobilized within the surface-grafted polymer matrices.[30,197]

Voelcker, Nann, and co-workers immobilized bioinspired $Fe_2S_2(CO)_6$ catalysts and InP quantum dots (QDs) onto a p-Si(100) semiconductor to photoelectrochemically drive H_2 production (Figure 12a).[198] This catalyst was chosen since it effectively binds to InP QDs and is active for HER. In this work, the hydrogen-terminated p-Si surface was initially capped with an electrochemically grafted methyl layer to avoid formation of an insulating surface oxide. The InP QDs (average size of 5−9 nm diameter) were then physisorbed onto the Si semiconductor, and the QD-modified electrode was immersed into a toluene solution containing the $Fe_2S_2(CO)_6$ catalysts. Structural characterization of the $Fe_2S_2(CO)_6$-modified photocathodes was performed using scanning electron microscopy (SEM), energy-dispersive X-ray spectroscopy (EDX), and time-of-flight secondary ion mass spectrometry (TOF-SIMS). Photoelectrochemical characterization was performed in a 0.1 M H_2SO_4 solution under simulated 1-sun illumination (AM 1.5 G, 100 mW cm^{-2} using a Xe lamp). The generation of H_2 was confirmed via GC. After ramping up the V_b from 0 to −0.50 V vs Ag/AgCl (equating to +0.27 to −0.23 V vs RHE),[199] *J* increased from ~0.05 to ~1.25 mA cm^{-2} (Figure 12b).

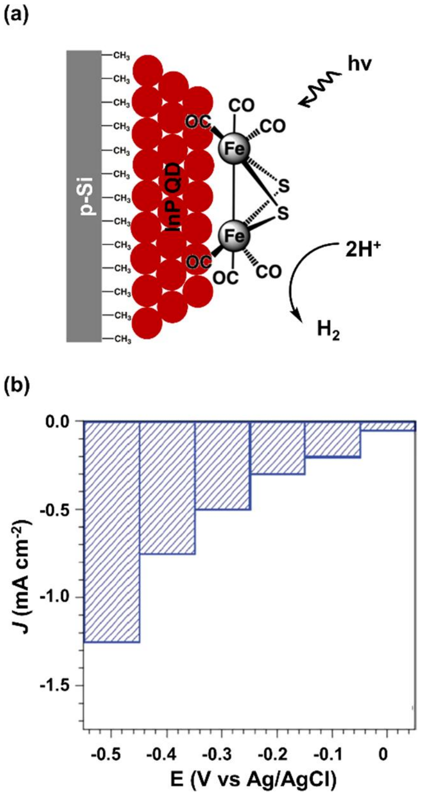

Figure 12. (a) Schematic representation of a $[Fe_2S_2(CO)_6]$-InP quantum dots-modified Si photoelectrode. (b) Photocurrent response of a p-Si electrode with electrochemically grafted methyl layer, physisorbed InP quantum dots, and functionalized with $Fe_2S_2(CO)_6$, recorded in 0.1 M H_2SO_4 under 100 mW cm^{-2} illumination. Adapted from ref 198.

Functionalization of n-type Si(111) surfaces was reported by Brunschwig, Lewis, Gray, and co-workers using mixed methyl/bipyridyl monolayers that chelate metal centers such as Rh, Ir, and Ru, forming assemblies that can be used in PEC devices.[200] In this approach, hydrogen-terminated Si(111) surfaces were subject to an initial chlorination treatment followed by partial methylation, which protected the surfaces against ambient or electrochemical oxidation. The remaining chlorinated sites were then functionalized with bipyridyl ligands via UV-induced olefin grafting of 4-vinyl-2,2′-bipyridine. The resulting bipyridyl-modified Si surfaces were then treated with appropriate metal-containing reagents to assemble analogs of pentamethylcyclopentadienyl rhodium, iridium, and ruthenium complexes ([Cp*Rh], [Cp*Ir], and [Ru(acac)$_2$], respectively, where Cp* is pentamethylcyclopentadienyl and acac is acetylacetonate). The assemblies were structurally characterized using XP and X-ray absorption spectroscopic (XAS) analysis. Surface-recombination velocities associated with the functionalized Si(111) electrodes were assessed using microwave conductivity measurements. These studies showed a decrease in the surface-recombination velocities from 2600 cm s^{-1} for Si samples containing a native oxide layer to values ranging between 23 and 41 cm s^{-1} for the methylated and methyl/chelated-bipyridyl monolayers, confirming the Si surfaces were well-passivated and capable of relatively facile charge transfer between the Si substrate and immobilized redox-active species. Although the immobilized complexes were electrochemically active in acetonitrile (MeCN), they rapidly dissociated from the Si surface upon redox cycling, complicating further PEC studies of the assemblies.

Functionalization of p-type Si(111) surfaces, uniquely suited for molecular modification due to the rigidly perpendicular orientation of its Si-X bonds, with DuBois-type H_2 evolution catalysts[125,201,202] was reported by Rose and co-workers. This work involved initial Negishi coupling of a PNP ligand (PNP = $Ph_2PCH_2NCH_2PPh_2$) with a hydrogen-terminated Si(111) surface.[203] The resulting PNP-modified surface was then treated with a Ni salt dissolved in MeCN before being exposed again to excess PNP to incorporate a second PNP ligand onto the immobilized Ni centers yielding samples of Si|PNP|Ni. The attachment chemistry at each step of the surface-modification procedure was confirmed using XP spectroscopic analysis. Photoelectrochemical characterization, performed using Si|PNP|Ni working electrodes (with surface coverage of 0.25 nmol Ni cm^{-2}) immersed in MeCN solutions (containing 0.2 M $LiClO_4$ as the supporting electrolyte and concentrations of trifluoroacetic acid (TFA) ranging from 0 to 91 mM) under broadband LED illumination (33 mW cm^{-2}) and a N_2 atmosphere, indicated the Si|PNP|Ni photocathodes were capable of generating H_2, as confirmed via gas chromatography−mass spectrometry (GC−MS). Under the electrolyte and illumination conditions mentioned above, an apparent TOF of 285 s^{-1} per catalytic species was reported when the Si|PNP|Ni working electrodes were polarized at −0.67 V vs the normal hydrogen electrode (NHE) in the presence of 91 mM TFA. In control experiments performed using methylated Si working electrodes immersed in a 0.2 M $LiClO_4$ in MeCN solution containing a nonsurface-attached analog of the Ni catalyst (2 μM), the potential required to reach 0.05 mA cm^{-2} was −0.26 V vs NHE, a potential 0.20 V more negative than that required when using the Si|PNP|Ni photocathodes measured under otherwise identical conditions. The authors postulated that this result was due to expedited electron transfer from the semiconductor to the catalyst species by the conjugated and covalently attached linker. In a related vein, work by Yang and co-workers on the interfacial electron-transfer kinetics of ferrocene-modified indium tin oxide (ITO) electrodes indicated that interfacial electron-transfer kinetics associated with constructs featuring noncovalent immobilization strategies could be similar to or even improved relative to those associated with constructs featuring covalent immobilization strategies.[204] In their work, attachment of the ferrocene units was achieved using either thermally induced grafting of vinylferrocene or a noncovalent attachment featuring $\pi-\pi$ interactions between pyrene-modified ITO surfaces and 1-pyrenylferrocene.

Marinescu and co-workers have reported on H_2-producing PEC assemblies that feature Co dithiolene (an efficient catalyst for HER) in a polymeric form that maintains catalytic activity and is relatively stable in acidic aqueous conditions. The polymer was dropcasted on planar p-type Si(100) (Figure 13a).[205] Using this method, a metal site loading of up to 6.3 × 10^3 nmol Co cm^{-2}, as determined via inductively coupled plasma mass spectrometry (ICP-MS), could be achieved. These electrodes produced J = 3 mA cm^{-2} or 8 mA cm^{-2} when polarized at 0 or −0.3 V vs RHE, respectively. These activities were at least 25% lower than those obtained using electrodes with loadings of 4 × 10^3 nmol Co cm^{-2} (producing 4 mA cm^{-2} when polarized at 0 V vs RHE and 13 mA cm^{-2} when polarized at −0.3 V vs RHE). The authors attributed the lower activities obtained using electrodes with higher Co loading to increased screening of light by the immobilized catalysts. Photoelectrochemical experiments were performed using pH 1.3 aqueous solutions (0.05 M H_2SO_4) under 1-sun illumination from a Xe lamp equipped with an AM 1.5 G filter. The Co dithiolene-modified working photoelectrodes achieved a J = 1 mA cm^{-2} when polarized at +0.13 V vs RHE, a potential 0.43 V more positive than that required to achieve an

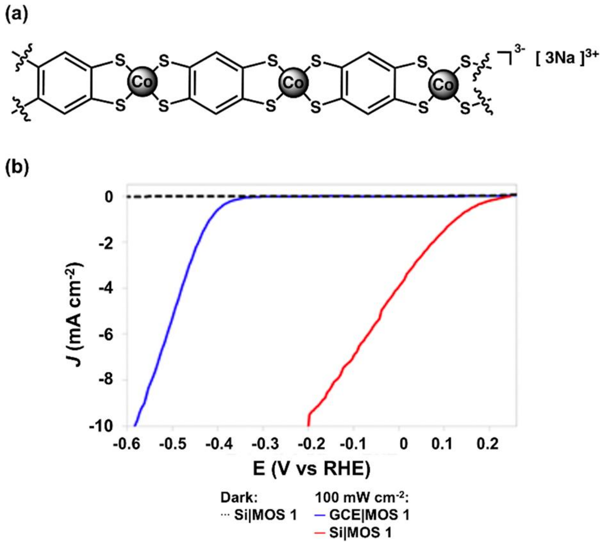

Figure 13. (a) Structure of cobalt-based coordination polymers based on benzene-1,2,4,5-tetrathiolate. (b) Linear sweep voltammograms of p-Si electrodes functionalized with Co-based coordination polymers based on benzene-1,2,4,5-tetrathiolate (MOS 1) recorded in 0.05 M H_2SO_4 in the dark (dashed black) or under 100 mW cm^{-2} illumination (solid red), at a scan rate of 10 mV s^{-1}, as well as a glassy carbon electrode functionalized with cobalt-based coordination polymers based on benzene-1,2,4,5-tetrathiolate (solid blue) recorded in 0.05 M H_2SO_4 under 100 mW cm^{-2} illumination, at a scan rate of 10 mV s^{-1}. Adapted with permission from ref 205. Copyright 2015 American Chemical Society.

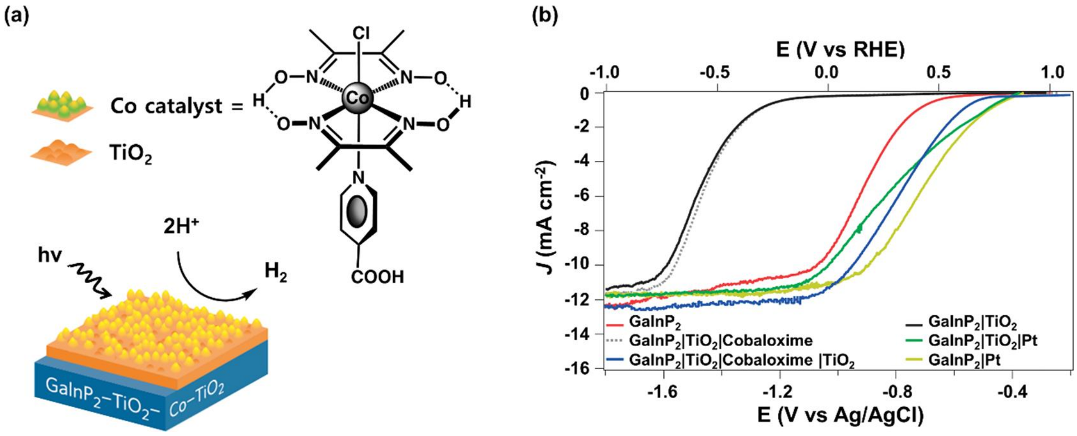

Figure 14. (a) Schematic representation of immobilization of cobaloxime onto $GaInP_2$ through a TiO_2 interface. (b) Linear sweep voltammograms of $GaInP_2$ electrodes (red), $GaInP_2$ electrodes with a TiO_2 protective layer (black), $GaInP_2$ electrodes with a TiO_2 protective layer and functionalized with cobaloxime catalyst (dotted gray), $GaInP_2$ electrodes with a TiO_2 protective layer and functionalized with Pt particles (green), $GaInP_2$ electrodes with a TiO_2 protective layer, functionalized with cobaloxime catalyst, and with a final TiO_2 layer (blue), and $GaInP_2$ electrodes with Pt particles (yellow) recorded in 0.1 M NaOH (pH 13) under 100 mW cm^{-2} illumination (solid red), at a scan rate of 20 mV s^{-1}. Adapted from ref 206. Copyright 2016 Springer.

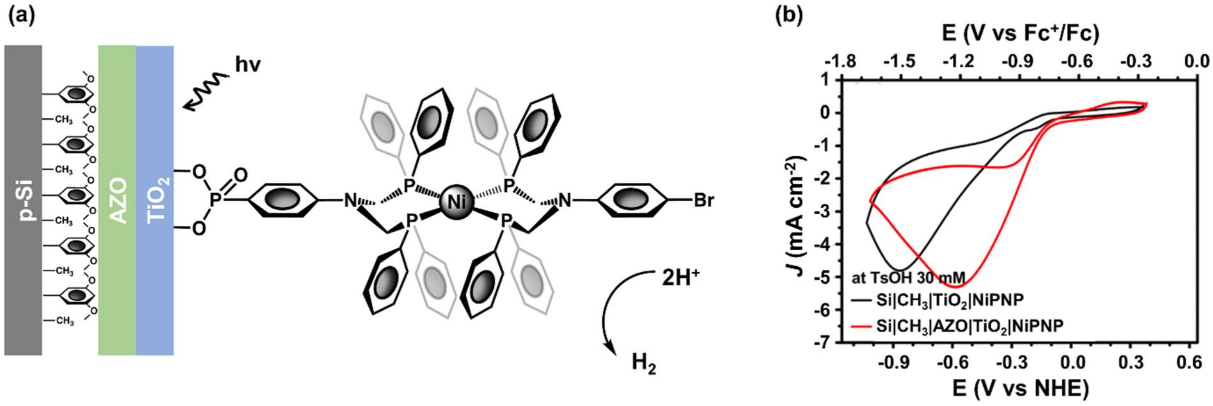

Figure 15. (a) Schematic representation of p-Si electrode modified with a layer of a dimethoxyphenyl/methyl groups, coated with an AZO|TiO_2 layer and NiPNP catalysts. (b) Cyclic voltammograms of Si|CH_3|TiO_2|NiPNP (black) and Si|CH_3|AZO|TiO_2|NiPNP (red) measured in 0.2 M $LiClO_4$ and 30 mM tosylic acid in MeCN under 33 mW cm^{-2} illumination, at a scan rate of 100 mV s^{-1}. Adapted with permission from ref 207. Copyright 2016 American Chemical Society.

equivalent activity when using unmodified Si working photoelectrodes, and 0.55 V more positive than that required to achieve an equivalent activity when using a glassy carbon electrode modified with the same Co dithiolene polymer (Figure 13b) at a surface loading of 7.6×10^2 nmol Co cm^{-2}. When polarized at 0 V vs RHE, the Co dithiolene-modified Si photocathodes (with loading of $\sim 4 \times 10^3$ nmol Co cm^{-2}) achieved a $J = 3.8$ mA cm^{-2} and were stable over 20 min with a reported *FE* of 80 ± 3%. Control experiments performed using unmodified Si working photoelectrodes immersed in electrolyte solutions with or without dissolved Co dithiolene precursors showed negligible J (<1 mA cm^{-2}) when polarized at 0 V vs RHE. Core level Co 2p, Na 1s, S 2s, and S 2p XP spectra of Co dithiolene-modified Si surfaces following PEC operation were similar to those collected using freshly prepared samples, suggesting the photocathodes were relatively stable during operation. However, core level Si 2p XP spectra collected following PEC operation showed the presence of both Si-H and Si-O species, indicating the presence of an interfacial oxide layer.

The use of atomic layer deposition (ALD) to deposit TiO_2 as a protective coating on $GaInP_2$ semiconductors (with a band gap of 1.83 eV) and as an interface material for immobilizing molecular catalysts was described by Turner and co-workers.[206] ALD TiO_2 can be deposited with controlled thickness, and adds stability under basic operating conditions. In this approach, a ∼35 nm thick TiO_2 coating was used to assemble cobaloxime catalysts (selected because they contain only earth-abundant elements) bearing an iso-nicotinic acid ligand as a surface-attachment group (Figure 14a). The modified semiconductors were characterized using attenuated total-reflection infrared (ATR-IR) and XP spectroscopies, which confirmed the presence of vibrational frequencies associated with the intact cobaloxime and the presence of Co species in a +3 oxidation state. ICP-MS analysis indicated a Co surface loading of 12.7 ± 1.2 nmol of Co cm^{-2}, a value in agreement with the loading determined using ultraviolet−visible (UV−vis) spectroscopic techniques (12.8 nmol of Co cm^{-2}). Additional TiO_2 (∼0.4 nm and achieved via an additional 10 cycles of ALD) was deposited on top of the cobaloxime-modified semiconductors as a strategy to further stabilize the attachment between the cobaloxime catalysts and initial TiO_2 coating. The modified photocathodes produced H_2 in basic aqueous conditions (0.1 M NaOH, pH 13) at a $J \approx 9$ mA cm^{-2}

when polarized at 0 V vs RHE under simulated 1-sun illumination using a Xe lamp, an activity relatively close ($J \approx 5$ mA cm^{-2}) to that achieved using GaInP$_2$-TiO$_2$ electrodes coated with Pt nanoparticles at a surface loading of 13 nmol cm^{-2} (Figure 14b). The TON for the cobaloxime catalysts over 20 h was 139,000, with a reported TOF of 1.9 s^{-1} per site when polarized at 0 V vs RHE. This work features a relatively early example of using ALD surface coatings to leverage the wealth of molecular attachment chemistries developed for applications on metal oxide surfaces.

Rose and co-workers expanded their previous work involving immobilization of DuBois-type Ni catalysts by developing a strategy for attaching an analog of this complex containing a phosphonated anchoring group (PNP) onto aluminum-doped zinc oxide (AZO) thin films (Figure 15a).[207] The phosphonate anchoring groups were selected since they yield relatively stable attachment of molecular species to metal oxide surfaces, while the AZO stabilizes the function of the device in aqueous conditions, expands the window of operation, and beneficially modulates the band-edge position. Using ALD, the AZO metal oxide was deposited onto p-Si(111) modified with either methyl (Si|CH$_3$|AZO) or a mixture of methyl and dimethoxyphenyl (Si|diMeOPh|AZO) moieties, surface linkers that effectively modulate the p−n heterojunction and onset potential (V_{onset}) values. Successful functionalization was confirmed via XPS, and Mott−Schottky analysis showed that addition of the AZO to methylated Si surfaces resulted in a 0.1 V positive shift of the $V_{flatband}$ (from +0.49 V vs NHE to +0.59 V vs NHE). Photoelectrochemical measurements were conducted by immersing modified Si electrodes in MeCN solutions containing 0.2 M LiClO$_4$ as the supporting electrolyte and increasing amounts of tosylic acid (TsOH) (up to 50 mM) under broadband LED illumination at 33 mW cm^{-2}. These experimental conditions were similar to those used in the previously described example from the Rose group,[203] but TsOH, instead of TFA, was used as the source of protons. The effect of the AZO interface was examined in control experiments where the PEC performance of AZO-modified methylated Si photocathodes coated with an amorphous TiO$_2$ layer that were further functionalized with the DuBois-type Ni catalysts, to form Si|CH$_3$|AZO|TiO$_2$|NiPNP, was compared with the PEC performance of the analogous assembly that did not contain the intervening AZO coating (Si|CH$_3$|TiO$_2$|NiPNP). Photoelectrochemical experiments conducted in MeCN solutions containing 0.2 M LiClO$_4$ and 30 mM TsOH showed the Si|CH$_3$|AZO|TiO$_2$|NiPNP photocathodes displayed a 70 mV positive shift in their V_{onset} (defined in their work as the potential required to achieve 0.5 mA cm^{-2}) as compared to those recorded using samples of Si|CH$_3$|TiO$_2$|NiPNP (with V_{onset} of −0.12 V vs NHE versus −0.19 V vs NHE, respectively) (Figure 15b). In addition, Si|CH$_3$|AZO|TiO$_2$|NiPNP achieved a saturating J at −0.6 V vs NHE, a potential 300 mV more positive than that measured for Si|CH$_3$|TiO$_2$|NiPNP. Finally, the effect of the organic layer between the Si surface and AZO metal oxide layer was studied by comparing the PEC performance of assemblies that contained Si surfaces modified with dimethoxyphenyl groups (Si|diMeOPh|AZO|TiO$_2$|NiPNP) in place of methyl groups. Experiments conducted in MeCN solutions containing 0.2 M LiClO$_4$ and 10 mM TsOH indicated that the V_{onset} of Si|diMeOPh|AZO|TiO$_2$|NiPNP was −0.07 V vs NHE, a value +0.10 V more positive than the V_{onset} of Si|CH$_3$|AZO|TiO$_2$|NiPNP (−0.17 V vs NHE). This report demonstrated that band edge energetics of photocathodes could be modulated by varying the molecular components of the semiconductor|catalyst interface. In more recent work by Gurrentz and Rose, the authors showed that upon binding a metal ion to a bisPNP ligand attached to a p-Si(111) surface, an enhanced band-bending (thermodynamics) was the primary contributor to the increased HER activity, whereas catalytic effects (kinetics) were minimal.[208] These results indicate that dipole and band-edge engineering should be a primary consideration when designing hybrid photoelectrosynthetic assemblies.

Reisner and co-workers have shown that TiO$_2$ films can be used as a biocompatible interface for assembling redox-active enzymes onto semiconducting materials, forming PEC assemblies capable of driving H$_2$ production under visible-light illumination.[111] These films also provide a protecting layer for the semiconductor surface. In this work, H$_2$-evolving [NiFeSe]-hydrogenases, isolated from *Desulfomicrobium baculatum*, were interfaced with TiO$_2$-coated p-Si(100) surfaces forming Si|TiO$_2$|[NiFeSe]H$_2$ase assemblies (Figure 16a). This enzyme is known to display a bias toward HER even in the presence of O$_2$. The amorphous TiO$_2$ films (~500 nm) were formed by dropcasting a solution of TiCl$_4$ in toluene on a hydrogen-terminated Si surface followed by hydrolysis in air. Preparation of the Si|TiO$_2$|[NiFeSe]H$_2$ase electrodes was achieved by dropcasting 3 μL of an 8 μM stock solution containing the enzyme onto a 1 cm^2 Si|TiO$_2$ electrode (this

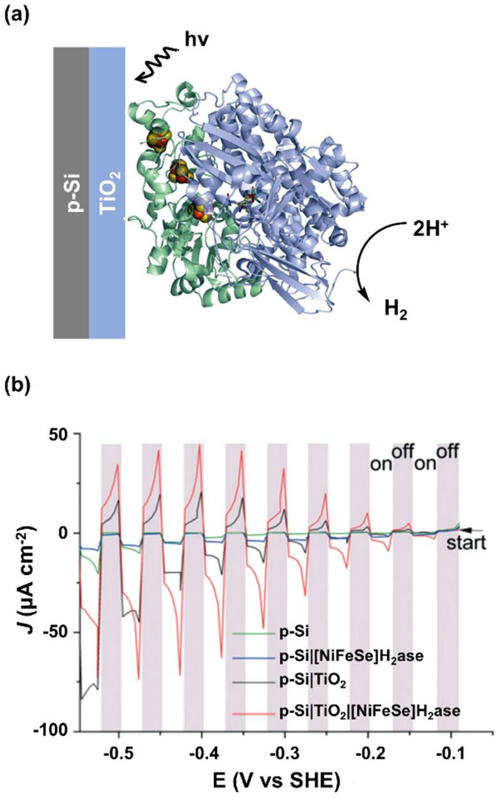

Figure 16. (a) Schematic representation of the [NiFeSe]-hydrogenase-immobilized TiO$_2$-coated p-Si photocathode. (b) Linear sweep voltammograms of p-Si (green), p-Si|[NiFeSe]H$_2$ase (blue), p-Si|TiO$_2$ (black), and p-Si|TiO$_2$|[NiFeSe]H$_2$ase (red) electrodes recorded in 0.50 M 2-(N-morpholino)ethanesulfonic acid (pH 6) under 10 mW cm^{-2} illumination, at a scan rate of 10 mV s^{-1}. Adapted with permission from ref 111. Copyright 2016 Wiley-VCH Verlag GmbH & Co.

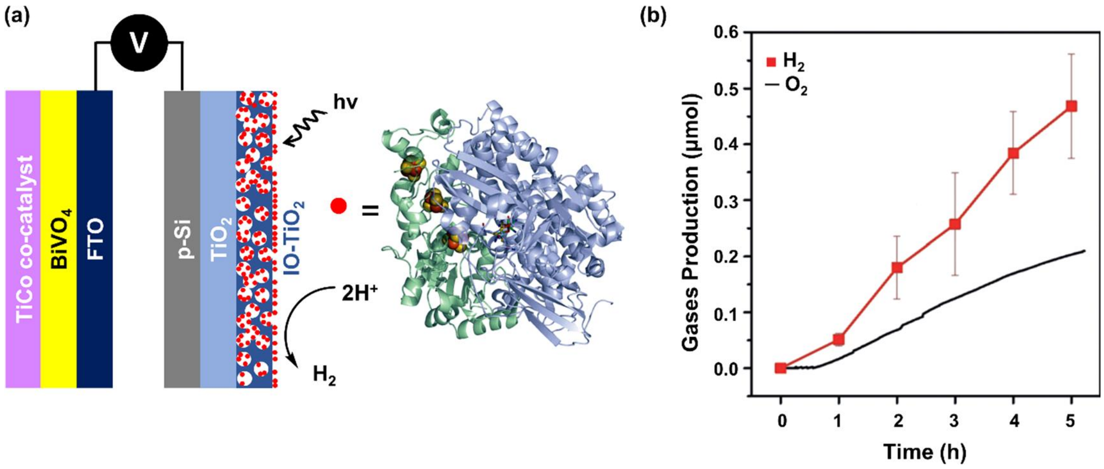

Figure 17. (a) Schematic representation of photoelectrochemical cell containing a p-Si photocathode modified with a hierarchical IO-TiO_2 layer decorated with [NiFeSe]-hydrogenases and a photoanode consisting of fluorine-doped tin oxide (FTO) electrode decorated with $BiVO_4$ and a TiCo precatalyst. (b) Amount of H_2 (red) and O_2 (black) produced by the two-electrode configuration cell with a p-Si|IO-TiO_2|[NiFeSe]H_2ase photocathode and an FTO|$BiVO_4$|TiCo photoanode in 0.50 M MES and 50 mM KCl solution (pH 6) under 100 mW cm^{-2} illumination for 5 h with no applied bias potential. Adapted with permission from ref 209. Copyright 2018 Wiley-VCH Verlag GmbH & Co.

equated to a per geometric area surface loading of 0.024 nmol cm^{-2}). For these assemblies, the authors postulated that photoexcited electrons are transferred from the Si E_{CB} via the TiO_2 layer to the active site of the NiFeSe enzyme. Photoelectrochemical experiments were performed using a nitrogen-saturated solution containing 50 mM of 2-(N-morpholino)ethanesulfonic acid (MES) at pH 6 under 10 mW cm^{-2} LED illumination. The *J* response of Si|TiO_2|[NiFeSe]H_2ase was recorded while polarizing the electrodes from +0.25 V to −0.20 V vs RHE and alternating between illuminated and nonilluminated conditions every 25 mV (2.5 s illuminated/2.5 s nonilluminated cycles and a scan rate of 10 mV s^{-1}). Although control experiments performed using Si|TiO_2 electrodes showed a photoresponse at −0.15 V vs RHE, the authors attributed this result to charging of the TiO_2 E_{CB}. Also, the *J* measured using the Si|TiO_2|[NiFeSe]H_2ase photocathodes were significantly higher than those measured using Si|TiO_2 electrodes in all experiments (Figure 16b). For example, when polarized at 0 V vs RHE under 10 mW cm^{-2} illumination for 1 h, the *J* produced by Si|TiO_2|[NiFeSe]H_2ase reached a stable value of 1 μA cm^{-2} after 15 min, and H_2 was generated with a near-unity *FE*. In control experiments using Si|TiO_2 photocathodes, the *J* was half that measured when using the Si|TiO_2|[NiFeSe]H_2ase photocathodes, and no H_2 was detected. Controlled-potential polarization experiments were also performed under alternating nitrogen and 10% CO in nitrogen atmospheres. CO is a reversible inhibitor of the hydrogenase active site, and in these experiments, the presence of CO reduced the *J* response by about half. However, the *J* recovered after the solution was flushed with nitrogen. Although the authors indicated that the performance of the hybrid construct was limited by the suboptimal loading of hydrogenase on the TiO_2 layer and the relatively low light intensity used in these experiments, the concept highlights an approach of using enzymes to construct semibiological assemblies.

Continuing their work involving hydrogenases, Reisner and co-workers investigated the activity of a boron-doped p-Si(100) photocathode modified with an inverse opal (IO) TiO_2 layer that was functionalized with [NiFeSe]-hydrogenases.[209] These constructs were prepared by depositing an initial layer of TiO_2 (~4 nm as measured using atomic force microscopy (AFM)) onto Si electrodes (0.178 cm^2) via ALD, followed by application of an additional layer of IO-TiO_2 (~10 μm) by co-assembly of TiO_2 NPs (P25, 21 nm) with polystyrene beads (750 nm), followed by heating at 450 °C. Hydrogenase enzymes isolated from *Desulfomicrobium baculatum* were then dropcasted onto the TiO_2-coated Si surfaces, resulting in an enzyme surface loading of 80 pmol (equivalent to 0.45 nmol cm^{-2}) as determined using quartz crystal microbalance. These loadings on IO-TiO_2 were three and 27 times higher than those obtained using mesoporous and planar TiO_2, respectively. ATR-IR spectra of the hydrogenase-modified assemblies (Si|IO-TiO_2|[NiFeSe]H_2ase) contained diagnostic signals assigned to NH and CO vibrational modes associated with the enzyme backbone. Controlled-potential polarization of the Si|IO-TiO_2|[NiFeSe]H_2ase photocathodes was performed in a three-electrode configuration using a 50 mM MES buffer (pH 6) and 50 mM KCl electrolyte solution under simulated 1-sun illumination using a Xe lamp equipped with an AM 1.5 G filter, an IR short-pass filter, and a 420 nm long-pass filter. The Si|IO-TiO_2|[NiFeSe]H_2ase photocathodes generated 17 ± 3 μmol cm^{-2} of H_2 (0.94 nmol H_2 cm^{-2} s^{-1}) at a *FE* of 86% as determined via GC analysis when polarized at 0 V vs RHE for 5 h. Control experiments conducted using Si|IO-TiO_2 modified with Pt nanoparticles in place of the hydrogenase enzymes indicated the two assemblies achieved similar activities and PEC performance. In addition, full water splitting was achieved using a two-electrode configuration where a Si|IO-TiO_2|[NiFeSe]H_2ase photocathode was connected to a photoanode composed of a fluorine-doped tin oxide (FTO) electrode decorated with $BiVO_4$ and TiCo (Figure 17a). In the absence of an externally applied voltage, the PEC cell achieved a *J* of 1 μA cm^{-2} that remained stable over 5 h, generating 0.47 ± 0.03 μmol of H_2 and 0.20 μmol of O_2 (0.15 nmol H_2 cm^{-2} s^{-1} and 0.06 nmol O_2 cm^{-2} s^{-1}) (Figure 17b). These values correspond to a *FE* of 98% ± 14 for H_2 production and 84% for O_2 production. Application of an external bias (up to 0.40 V) resulted in an increased *J* and quantity of H_2 formed, with a *FE* of H_2 evolution that remained above 80%.

Another example of successful immobilization of hydrogenase enzymes onto an inorganic semiconductor surface for applications in artificial photosynthesis was reported by Neale, King, Branz, and co-workers.[210] Native [Fe-Fe]-hydrogenases from *Clostridium acetobutylicum* ([FeFe]H_2ase) were adsorbed onto nanoporous black p-Si(100) (b-Si). This semiconductor was chosen over planar Si due to its inherent antireflection properties and ability to suppress adhesion of H_2 bubbles. The hydrogenase-modified photoelectrodes (b-Si|[FeFe]H_2ase) were shown to be active for H_2 production in a neutral aqueous solution (1 M phosphate buffer, pH 6.8) under illumination using a tungsten arc lamp equipped with a fiber-optic cable (10 mW cm^{-2}). V_{onset} (defined in their work as the potential required to achieve 0.1 mA cm^{-2}) of the b-Si|[FeFe]H_2ase photocathodes was −0.22 V vs Ag/AgCl (equating to + 0.39 V vs RHE),[188] 280 mV more positive than the V_{onset} recorded using unmodified b-Si, and the J reached a limiting value of 35 mA cm^{-2} at −0.10 V vs RHE. Upon increasing the intensity of illumination (from 5 to 50 mW cm^{-2}) or increasing the geometric area loading of hydrogenases (from 6 to 24 pmol cm^{-2}), the J measured at −0.60 V vs Ag/AgCl (+0.01 V vs RHE) increased linearly. Mass-transfer of protons became a limiting factor when lower concentrations (between 0.1 to 0.5 M) of buffer were used. When polarized at −0.50 V vs Ag/AgCl (+0.11 V vs RHE) and under 10 mW cm^{-2} illumination, the b-Si|[FeFe]H_2ase photocathodes evolved H_2 at a $J \approx 1.4$ mA cm^{-2} with a *FE* of 35% recorded over 60 min of operation. In these studies, a decay in J over the initial 10 min was attributed to desorption or deactivation of the hydrogenase complexes. In control experiments performed using b-Si samples modified with Pt nanoparticles (b-Si|Pt NP) instead of hydrogenases, a similar activity for H_2 production was achieved. The b-Si|[FeFe]H_2ase electrodes with a loading of 12 pmol cm^{-2} achieved a $J \approx 3$ mA cm^{-2} when polarized at −0.5 V vs Ag/AgCl (+0.11 V vs RHE) under 50 mW cm^{-2} illumination. Given the loading of enzyme, this equates to a TOF of ∼1300 s^{-1} per site. In addition, a TON above 9.9×10^6 was reported for the immobilized enzymes following 5 h of illumination at 10 mW cm^{-2}. Further, electrochemical impedance spectroscopy (EIS) performed at a $V_b = -0.35$ V vs Ag/AgCl (+0.26 V vs RHE) and using 5 mW cm^{-2} illumination indicated the interfacial charge-transfer resistance was 0.6 kΩ for the b-Si|[FeFe]H_2ase photocathodes (a value similar to the 1 kΩ measured when using b-Si|Pt NP photocathodes) and 32 kΩ for unmodified b-Si photoelectrodes.

Reisner and co-workers immobilized analogs of DuBois-type Ni catalysts bearing phosphonic acid anchoring groups (NiP) or diamine-dioxime cobaloxime catalysts bearing phosphonic acid anchoring groups (CoP^3) to p-type Si electrodes modified with mesoporous metal oxide overcoatings.[128] In this work, mesoporous TiO_2, selected to increase the loading capacity, was spin-coated onto Si surfaces followed by annealing in air to give a 6 μm thick TiO_2 coating (Si|mesoTiO_2). The metal oxide films were imaged using SEM, and electrode surfaces modified with Ni- or Co-based catalysts were studied using ATR-IR and XP spectroscopies. The mesoporous nature of the metal oxide films resulted in relatively high surface areas as compared to planar Si wafers and enabled catalyst surface loadings of 38.3 ± 4.2 nmol cm^{-2} for the Ni catalyst and 93.9 ± 8.9 nmol cm^{-2} for the Co catalyst. Three-electrode voltammetry measurements were conducted in aqueous HCOOH solutions (0.1 M, pH 4.5) under 1-sun illumination using a Newport Oriel lamp equipped with AM 1.5 G and 400 nm long-pass filters, and alternating between illuminated and nonilluminated conditions in 5 s intervals, at a scan rate of 10 mV s^{-1}. Voltammograms of Si|mesoTiO_2 electrodes (with and without catalysts) showed an V_{onset} (defined in their work as the potential required to achieve a $J = 10$ μA cm^{-2}) at + 0.4 V vs RHE. However, addition of the molecular catalysts to Si|mesoTiO_2 photocathodes (forming Si|mesoTiO_2|NiP or Si|mesoTiO_2|CoP^3) resulted in an increase in J recorded at 0 V vs RHE from 0.1 mA cm^{-2} for Si|mesoTiO_2 electrodes to 0.34 mA cm^{-2} for the catalyst-modified Si|mesoTiO_2 electrodes. Controlled-potential polarization experiments performed at 0 V vs RHE using Si|mesoTiO_2|NiP under continuous illumination for 24 h indicated a TON of 646 ± 141 with a *FE* up to 87% after 6 h and 76% after 24 h. Structural analysis following 24 h of PEC operation via ATR-IR and XP spectroscopy indicated the NiP catalysts maintained their molecular integrity, with no evidence of nonmolecular Ni species on the surface. In contrast, the Si|mesoTiO_2|CoP^3 photoelectrodes lacked the diagnostic spectral signals of the molecular species, indicating potential instability of the cobaloxime catalysts following 24 h of PEC operation.

Following on their earlier work using cobaloxime-type catalysts, Moore and co-workers showed that Co and Fe porphyrins (electrocatalysts able to reduce H^+ and CO_2) can be directly immobilized onto the surface of p-GaP(100) using metalloporphyrins that were synthetically modified to include a covalently attached vinylphenyl group at the periphery (β-position) of the porphyrin macrocycle (Figure 18a).[211] Successful immobilization of both Co and Fe porphyrins following UV-induced grafting chemistry was confirmed using GATR-FTIR and XP spectroscopies. ICP-MS indicated a Co porphyrin loading of 0.59 ± 0.03 nmol cm^{-2}. The Co porphyrin-modified photocathodes (GaP|CoP) were active for stable solar H_2 production in neutral aqueous conditions (0.1 M phosphate buffer, pH 7) under simulated 1-sun illumination using Oriel Solar Simulator equipped with an AM 1.5 G filter, while the analogous assembly containing Fe porphyrins (GaP|FeP) showed significant diminution of PEC performance (Figure 18b) including a rapid loss in J following illumination during controlled-potential polarization measurements. Both electrodes displayed an V_{oc} of +0.61 V vs RHE (0.04 V more positive than unmodified GaP electrodes). When polarized at 0 V vs RHE, GaP|CoP achieved a $J = 1.31$ mA cm^{-2} and GaP|FeP obtained a $J = 1.29$ mA cm^{-2}. However, the FE for H_2 production when using GaP|FeP was only 45%, while the FE for H_2 production when using GaP|CoP was near unity (equating to an HER activity of 3.9 H_2 s^{-1} Co^{-1}). Considering only photons within the actinic range of GaP (280−549 nm), an EQE of 19% was measured using GaP|CoP electrodes polarized at 0 V vs RHE. Using either the enthalpy of H_2 combustion (higher heating value of 286 kJ mol^{-1}) or change in Gibbs free energy (237 kJ mol^{-1}), yields an optical to chemical power conversion efficiency (which is the ratio of the output chemical power to the spectral irradiance from 280−549 nm) of 11% and 9%, respectively.

In more recent work, Moore and co-workers published an analysis of charge recombination kinetics involving metalloporphyrin-modified semiconductors used for PEC hydrogen generation.[212] The constructs used in this report were prepared via the previously reported one-step photochemical grafting method,[211] which does not rely on the coordination chemistry of a specific metal site and thus enables

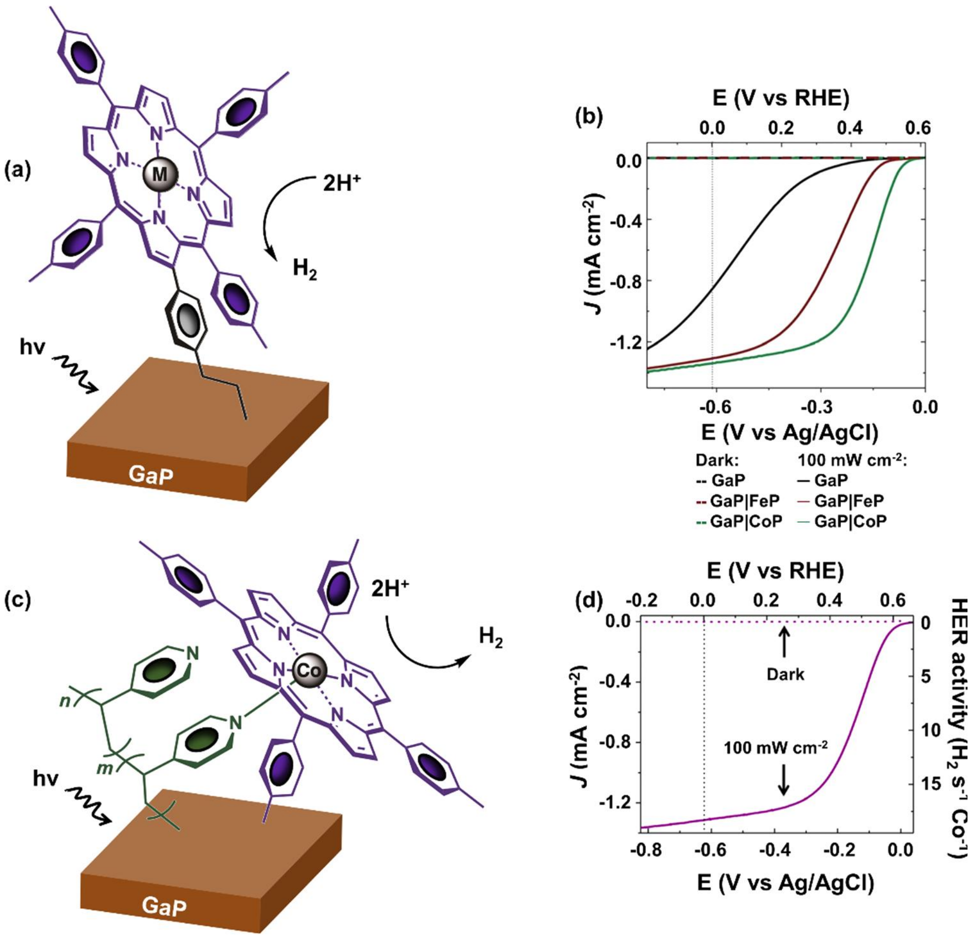

Figure 18. Schematic representation of metalloporphyrin-modified GaP using a (a) direct attachment strategy or (c) polymeric interface. (b) Linear sweep voltammograms of GaP (black), GaP|FeP (brown), and GaP|CoP (green) recorded in 0.1 M phosphate buffer (pH 7) in the dark (dashed lines) or under 100 mW cm^{-2} illumination (solid lines), at a scan rate of 100 mV s^{-1}. (d) Linear sweep voltammograms of GaP|PPy|CoP electrodes recorded in 0.1 M phosphate buffer (pH 7) in the dark (dotted purple) or under 100 mW cm^{-2} illumination (solid purple), at a scan rate of 100 mV s^{-1}. The calculated HER activity per cobalt center is included on the right-coordinate axis. (a, b) Adapted with permission from ref 211. Copyright 2017 Royal Society of Chemistry. (c, d) Adapted with permission from ref 213. Copyright 2017 American Chemical Society.

functionalization of GaP semiconductors with a range of metalloporphyrins featuring different metal centers including Fe, Co, Ni, Cu, or Zn complexes. Linear sweep voltammograms recorded in pH-neutral aqueous solutions under simulated solar illumination showed the metalloporphyrin-modified GaP electrodes displayed relatively similar values of J_{sc}, but significantly varied in their values of V_{oc} and fill factor, and displayed overall different waveform shapes for their respective J−V curves. These results set the stage for better understanding structure−function relationships governing the performance of molecular-modified photoelectrodes as well as strategies to optimize their architectures and performance.

In addition to the direct grafting of metalloporphyrins containing 'built-in' vinylphenyl surface-attachment functional groups, Moore and co-workers also showed that Co porphyrins can be immobilized on p-GaP(100) surfaces using an initially applied PPy surface coating similar to that used in previous work from their group for immobilizing cobaloxime-type catalysts (Figure 18c).[213] Following wet chemical processing of GaP|PPy surfaces featuring a relatively thin-film PPy coating (1.45 ± 0.17 nm), analysis via ICP-MS, ellipsometry, and XPS, indicated 25% of the pyridyl nitrogens coordinated to Co porphyrin metal centers, yielding a surface concentration of ~0.39 Co cm^{-2}. When photoelectrochemically characterized in neutral aqueous conditions (0.1 M phosphate buffer, pH 7) under simulated AM 1.5 G illumination (Oriel Solar Simulator, 100 mW cm^{-2}), the cobalt porphyrin-polypyridyl-modified photocathodes (GaP|PPy|CoP) achieved an V_{oc} of +0.65 V vs RHE (80 mV more positive than that recorded using unmodified GaP electrodes) and a J = 1.27 mA cm^{-2} when polarized at 0 V vs RHE (Figure 18d). Given the near-unity (93%) *FE* of these assemblies for H_2 production, this equates to an HER activity of 10 μL min^{-1} cm^{-2} or 17.6 H_2 s^{-1} Co^{-1}. Comparison of GATR-FTIR spectra collected before and after 60 min of PEC operation indicated that the molecular integrity of the surface-immobilized Co porphyrin species remained intact.

Moore and co-workers developed GaAs (with a smaller band gap of 1.43 eV as compared to the GaP band gap of 2.26 eV used in their previous works) photoelectrosynthetic assemblies featuring polymeric coatings containing cobaloxime-type HER catalysts (GaAs|PPy|Cobaloxime) (Figure 19a).[214] When used as a working electrode wired in a three-electrode assembly under simulated AM 1.5 G illumination in 0.1 M phosphate buffer (pH 7), the construct achieved J > 20 mA cm^{-2}, enabling identification of fundamental performance-limiting factors encountered at relatively high rates of fuel formation. Experiments conducted under varying V_b, pH, illumination

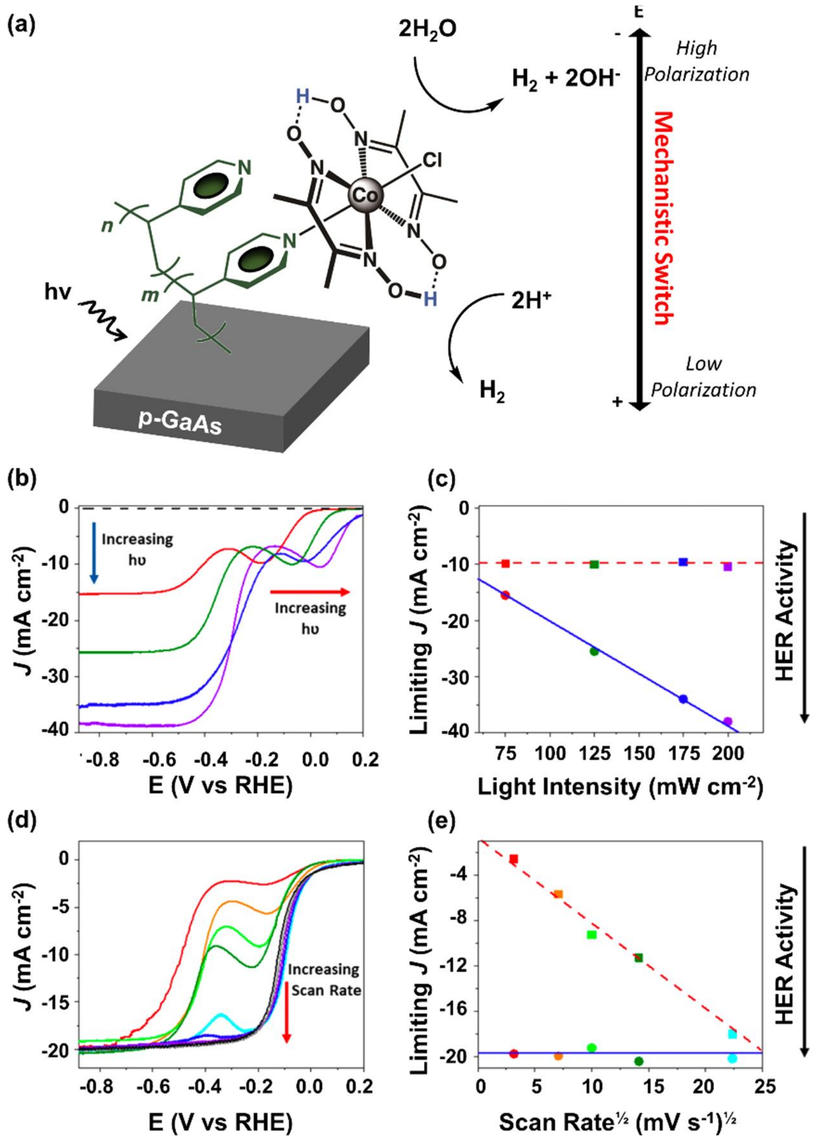

Figure 19. (a) Schematic representation of a cobaloxime-type catalyst immobilized onto a GaAs electrode via an intervening thin-film polypyridyl coating. (b) Linear sweep voltammograms of GaAs|PPy|Cobaloxime electrodes recorded in 0.1 M phosphate buffer (pH 7) in the dark (dashed black) or under 75 (red), 125 (green), 175 (blue), and 200 (violet) mW cm^{-2} illumination and at 100 mV s^{-1}. (c) Limiting current densities recorded at less negative bias potentials (squares) and more negative bias potentials (circles) versus the illumination intensities from (b). (d) Linear sweep voltammograms of GaAs|PPy|Cobaloxime electrodes recorded in 0.1 M phosphate buffer (pH 7) under 100 mW cm^{-2} illumination and at scan rates of 10 (red), 50 (orange), 100 (light green), 200 (green), 500 (light blue), 700 (blue), 1000 (violet), 1200 (gray), and 1500 (black) mV s^{-1}. (e) Limiting current densities recorded at less negative bias potentials (squares) and more negative bias potentials (circles) versus the square root of the scan rates from panel d. Adapted with permission from ref 214. Copyright 2021 American Chemical Society.

intensity, and scan rate, indicated a potential-dependent switching of the mechanism of PEC H_2 production. At relatively low polarization and pH, the limiting photoactivity was independent of illumination conditions and attributed to a mechanism involving reduction of substrate protons (Figure 19b,c). At relatively high polarization or pH, the limiting photoactivity showed a linear response to increasing photon flux and was attributed to a mechanism involving reduction of substrate water. Contributions from surface states to the waveforms of the linear sweep voltammograms were not ruled out. Nonetheless, this work highlights diagnostic tools for better understanding these processes and illustrates the complex interplay between transport of photons, electrons, and chemical substrates in photoelectrosynthetic reactions.

As an alternative strategy to immobilizing molecular electrocatalysts to the surfaces of semiconductors to improve their PEC performance, Neale and co-workers have attached fluorinated aromatic compounds with strong dipoles to the semiconductor surfaces to tune the V_{onset} of zinc-doped p-GaAs(100) photocathodes (Figure 20) and thus reduce η associated with H_2 production.[215] The attachment was performed via salt-metathesis chemistry using Grignard reagents or lithiated precursors, and the molecular-modified surfaces were characterized by XPS. In general, the samples featuring surface modification via use of lithiated precursors yielded higher surface coverages of immobilized aromatic compounds than those prepared using Grignard reagents, and displayed relatively greater shifts in V_{onset} (defined in their work as the zero-photocurrent density point of a linear regression fit to the linear portion of each current−potential curve). For example, when GaAs electrodes functionalized using the lithiated 4-(trifluoromethyl)phenyl precursor were characterized in pH −0.5 electrolyte (3 M H_2SO_4) under simulated 1-sun illumination using a quartz tungsten halogen lamp, the V_{onset} was +0.04 V vs RHE, a potential 0.14 V more positive than that achieved using unmodified GaAs electrodes under otherwise identical experimental conditions. Conversely, when using GaAs electrodes functionalized via the related Grignard reagent (4-(trifluoromethyl)phenyl magnesium bromide) and otherwise identical experimental conditions, the V_{onset} was 0.10 V more positive than that achieved using unmodified GaAs electrodes. Molecular modification of the GaAs surfaces also resulted in delayed surface oxide formation. Although the immobilized molecular species were unstable after 50 h of controlled-potential polarization at −0.50 V vs RHE, a J = 20.5 mA cm^{-2} was achieved during these experiments.

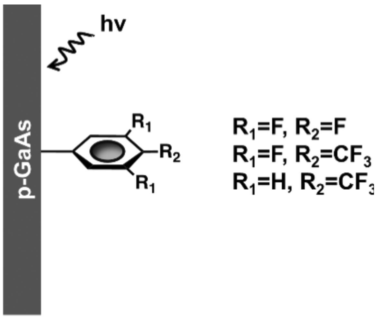

Figure 20. Schematic representation of molecular-modified p-GaAs surface using fluorinated aromatic molecules. Adapted with permission from ref 215. Copyright 2017 Wiley-VCH Verlag GmbH & Co.

Reisner, Domen, and co-workers have interfaced TiO_2-coated $La_5Ti_2Cu_{0.9}Ag_{0.1}S_5O_7$ (LTCA) (chosen because of its relatively broad range of light absorption, including wavelengths up to 710 nm) with H_2-evolving DuBois-type Ni bis(diphosphine)-based catalysts (NiP) (used to exploit its activity under mildly acid operating conditions), forming LCTA|TiO_2|NiP assemblies.[216] The nanostructured LTCA surfaces were stabilized with a thin TiO_2 layer (∼2 nm), deposited using reactive radio frequency magnetron sputtering followed by annealing under air. The initially applied TiO_2 layer minimized charge recombination and provided a platform with a high affinity for attachment to the phosphonic acid anchoring groups of the Ni-catalyst. The rod-like morphology of the LTCA nanostructures enabled a catalyst loading of 33.7 ± 2.4 nmol cm^{-2}, as determined via SEM studies and UV−vis spectroscopic analysis of a solution containing Ni catalysts desorbed from the semiconductor surface. During controlled-potential polarization experiments performed in aqueous solutions (0.1 M Na_2SO_4, pH 3) under simulated 1-sun illumination using a SAN-EI solar simulator equipped with an AM 1.5 G filter and a 300 nm long-pass filter, the LCTA|TiO_2|NiP constructs achieved an initial J = 0.20 mA cm^{-2} when polarized at +0.30 V vs RHE. A decrease in the J by ∼50% following 3 h of controlled-potential polarization was attributed to catalyst desorption or degradation, consistent with the ∼50% loss of catalyst from the surface measured following PEC operation over the same 3 h duration. H_2 was detected via GC analysis, and the associated FE was 87%. A TON of 50 per site was calculated for the immobilized Ni catalysts in these assemblies.

Artero and co-workers reported a PEC assembly consisting of a boron-doped p-Si(100) surface protected with a 15 nm layer of TiO_2 deposited via ALD (to passivate the semiconductor surface) and a second layer of mesoporous TiO_2 nanoparticles deposited using spin-coating (to protect the catalyst-surface linkage).[217] Cobalt diamine-dioxime molecular catalysts bearing decylphosphonate anchoring groups (Co_{C11P}) were then immobilized onto the mesoporous TiO_2 surface coating, followed by deposition of an additional 0.2 nm TiO_2 layer via ALD to prevent hydrolysis of the phosphonate anchoring groups (Figure 21a). The Co catalyst-TiO_2-modified Si photocathodes (Si|ALD-TiO_2|SC-TiO_2|Co_{C11P}|ALD-TiO_2) were structurally characterized via FTIR and XP spectroscopies, and the per geometric area catalyst loading was 67.4 ± 0.42 nmol cm^{-2} as determined using inductively coupled plasma atomic emission spectrometry (ICP-AES). Linear sweep voltammetry experiments conducted in neutral pH (1 M phosphate buffer) under simulated 1-sun illumination using a Xe lamp showed the Si|ALD-TiO_2|SC-TiO_2|Co_{C11P}|ALD-TiO_2 electrodes were active for H_2 production, achieving a J = 1.25 mA cm^{-2} when polarized at 0 V vs RHE (Figure 21b). In comparison, control experiments performed using photoelectrodes without the 0.2 nm TiO_2 overlayer (Si|ALD-TiO_2|SC-TiO_2|Co_{C11P}) yielded a J = 0.5 mA cm^{-2} when polarized at the same potential. Controlled-potential polarization at 0 V vs RHE using Si|ALD-TiO_2|SC-TiO_2|Co_{C11P}|ALD-TiO_2 electrodes indicated the J remained at ∼1.25 mA cm^{-2} and generated 17.3 μmol H_2 cm^{-2} (4.8 nmol cm^{-2} s^{-1}) over the course of 1 h with a FE of 84% as determined via GC analysis. Given the reported catalyst loading, this yields an apparent TOF of 0.071 s^{-1} per site and the TON for the immobilized Co catalysts over 1 h was estimated to be 260.

Artero and co-workers also reported covalent attachment of a cobaloxime catalyst bearing an axial 4,4′-pyridine ligand functionalized with two carboxylic acid anchoring groups (CoHEC) (Figure 22) onto $CuFeO_2$ delafossite, a material with a band gap of ∼1.5−1.6 eV and based on earth-abundant elements.[218] In this work, copper-iron oxide ($CuFe_xO_y$) films (denoted here as $CuFe_xO_{yFLAT}$) were prepared via spin coating a mixture of 0.2 M $Cu(NO_3)_2{\cdot}3H_2O$ and 0.2 M $Fe(NO_3)_3{\cdot}9H_2O$ onto a glass|FTO substrate followed by heating up to 200 °C in air for 30 min to stabilize the films. This process was repeated five times, and at the last annealing step the substrate was heated at 450 °C for 30 min and then at 600 °C for 2 h under argon flow to eliminate all organic residues, reduce Cu(II) to Cu(I), and crystallize the Cu-Fe oxide films. On one batch of samples, amorphous TiO_2 was deposited using ALD to form samples of $CuFe_xO_y$|TiO_2. On another batch, the $CuFe_xO_{yFLAT}$ surface was nanostructured using a F108 triblock copolymer template to form samples of $CuFe_xO_{ySTRUCT}$. Characterization of the $CuFe_xO_{yFLAT}$ and $CuFe_xO_{ySTRUCT}$ surfaces was performed using SEM, X-ray powder diffraction (XRD) analysis, and EDX as well as Raman spectroscopies. XRD analysis showed the presence of $CuFeO_2$, $CuFe_2O_4$, and Fe_2O_3 phases on $CuFe_xO_{yFLAT}$, whereas $CuFe_xO_{ySTRUCT}$ was composed of only $CuFe_2O_4$. According to the Tauc plots generated from UV−vis absorption measurements, $CuFe_xO_{yFLAT}$ exhibited an indirect band gap and two direct band gaps associated with $CuFeO_2$ and $CuFe_2O_4$ phases, as

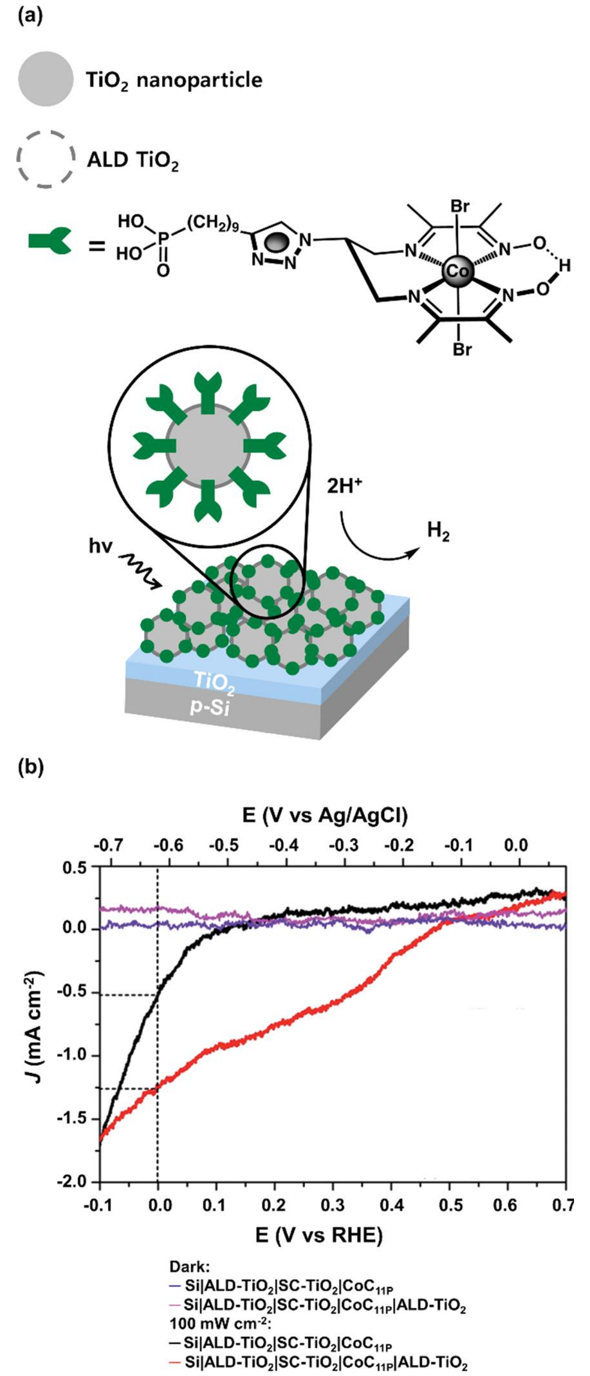

Figure 21. (a) Schematic representation of a cobalt catalyst-functionalized Si. (b) Linear sweep voltammograms of Si|ALD-TiO_2|SC-TiO_2|Co_{C11P}|ALD-TiO_2 electrodes recorded in 1 M phosphate buffer (pH 7) in the dark (magenta) or under 100 mW cm^{-2} illumination (red), at a scan rate of 10 mV s^{-1}, as well as Si|ALD-TiO_2|SC-TiO_2|Co_{C11P} electrodes recorded in 1 M phosphate buffer (pH 7) in the dark (violet) or under 100 mW cm^{-2} illumination (black), at a scan rate of 10 mV s^{-1}. Adapted with permission from ref 217. Copyright 2019 Royal Society of Chemistry.

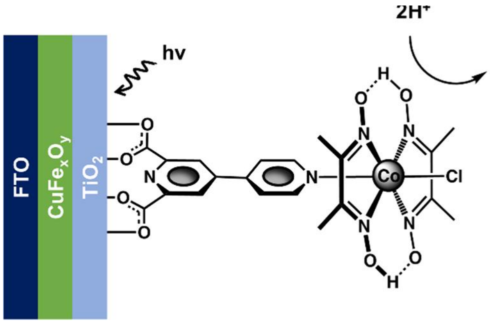

Figure 22. Schematic representation of a cobaloxime-functionalized $CuFe_xO_y$. Adapted from ref 218. Copyright 2020 Royal Society of Chemistry.

well as another indirect band gap associated with an Fe_2O_3 parasitic phase. A $V_{flatband}$ of ∼+0.70 V vs RHE was estimated for $CuFe_xO_{yFLAT}$ from EIS data performed in the dark and V_{oc} measurements performed under illumination (65 mW cm^{-2} using a filtered light source that included only the 400−780 nm portion of the solar spectrum), both performed using 0.2 M phosphate buffer as the electrolyte. Assuming the E_{VB} of $CuFe_xO_{yFLAT}$ is located ∼0.1−0.2 V positive of $V_{flatband}$,[219] E_{VB} was determined to be +0.8 to +0.9 V vs RHE. Considering the indirect band gap of 1.6 eV, the authors placed the E_{CB} potential at −0.7 to −0.8 V vs RHE. $CuFe_xO_y$|TiO_2 electrodes were characterized using ellipsometry, SEM, XRD analysis, and EDX as well as XPS. CoHEC was grafted onto $CuFe_xO_{ySTRUCT}$ and $CuFe_xO_y$|TiO_2 via soaking in methanolic solutions containing 0.7 mM of CoHEC overnight to yield $CuFe_xO_{ySTRUCT}$|CoHEC and $CuFe_xO_y$|TiO_2|CoHEC, respectively, and the presence of the Co catalyst was evidenced using UV−vis spectroscopy, ICP-AES, and XPS. Linear sweep voltammograms recorded using $CuFe_xO_{ySTRUCT}$|CoHEC electrodes under illumination (65 mW cm^{-2}, 400−780 nm) in 0.2 M phosphate buffer (pH 6.7) yielded an V_{onset} (defined by the authors as "the potential at which the semiconductor starts to show photocurrents") of +0.7 V vs RHE. Although grafting CoHEC on the surface of $CuFe_xO_{ySTRUCT}$, to form $CuFe_xO_{ySTRUCT}$|CoHEC, approximately doubled the J recorded in linear sweep voltammetry experiments and quadrupled the J recorded in controlled-potential polarization experiments, desorption of the catalyst and degradation of the electrode occurred during these measurements. Conversely, the $CuFe_xO_y$|TiO_2|CoHEC electrodes, featuring a TiO_2 protection layer, displayed a relatively stable J when polarized at +0.40 V vs RHE over 20 min with values of 7.6 ± 2 nmol H_2 cm^{-2}, a *FE* of 54%, a TON of 90 ± 30, and a TOF of 0.08 s^{-1}. Under slightly higher illumination intensities (100 mW cm^{-2}, 400−780 nm), the construct yielded a *FE* of 88% and a TON of 90 within 20 min. Although the J achieved using TiO_2-protected photoelectrodes were significantly lower than those measured using electrodes without TiO_2 layers, the authors noted that the presence of TiO_2 significantly and positively affected the *FE* for H_2 evolution and prevented at least partially the photocorrosion of the semiconductor. However, as noted by the authors, the stability of $CuFe_xO_y$ material remains challenging and must be further improved for PEC applications.

Yang, Neale, and co-workers have reported the use of four different aromatic-molecular layers (pyrene (Pyr), naphthalene (Nap), styrene (Sty), and 4-trifluoromethylstyrene ($StyCF_3$)) to immobilize Co bis(benzene-dithiolate) ([Co]) through noncovalent $\pi-\pi$ interactions on nanoporous b-Si photoelectrodes.[220] b-Si was selected because it has a surface area five times higher than its projected area due to its nanostructure. [Co] was used because of its ability to engage in $\pi-\pi$ interactions with the aromatic layers. The aromatic

Table 2. Summary of Data from Yang, Neale, and Co-workers[a]

sample	φ (eV)	V_{flatband} (V vs RHE)	V_{onset} (V vs RHE)	pseudo fill factor
b-Si	3.99	+0.18 ± 0.01	−0.31 ± 0.01	
b-Si|Pyr	4.04	+0.25 ± 0.01	−0.38 ± 0.01	
b-Si|Nap	4.03	+0.21 ± 0.01	−0.40 ± 0.02	
b-Si|Sty	3.93	+0.26 ± 0.02	−0.52 ± 0.01	
b-Si|StyCF$_3$	4.19	+0.23 ± 0.02	−0.61 ± 0.02	
b-Si|[Co]		+0.24 ± 0.01	−0.17 ± 0.02	0.55 ± 0.02
b-Si|Pyr|[Co]	3.73	+0.24 ± 0.01	−0.21 ± 0.02	0.57 ± 0.02
b-Si|Nap|[Co]	3.89	+0.22 ± 0.01	−0.19 ± 0.02	0.63 ± 0.02
b-Si|Sty|[Co]	3.93	+0.20 ± 0.01	−0.27 ± 0.04	0.52 ± 0.03
b-Si|StyCF$_3$|[Co]	3.92	+0.20 ± 0.01	−0.21 ± 0.02	0.55 ± 0.01

[a] Adapted with permission from ref 220. Copyright 2020 American Chemical Society.

moieties were covalently attached to hydrogen-terminated b-Si surfaces via thermally induced grafting of vinyl-modified analogs (e.g., 1-vinylpyrene or 2-vinylnaphthalene). Successful modification of the aromatic-molecular coatings was confirmed via FTIR spectroscopy. Although a surface coverage of the molecular layers was not determined, the authors hypothesized that the surface coverage depended on the size of the molecular moieties. Thus, the authors indicated the surface coverage of the modified b-Si electrodes should be as follows: b-Si|Pyr < b-Si|Nap < b-Si|StyCF$_3$ < b-Si|Sty. Catalyst immobilization on the b-Si|Aromatic electrodes was confirmed using XPS, and from these data the work function (φ, energy difference between E_F and vacuum) was determined. The φ values of b-Si|Pyr and b-Si|Nap were 50 meV positive of the φ associated with unmodified b-Si (3.99 eV), whereas the φ of b-Si|Sty was 50 meV negative of the φ associated with unmodified b-Si. However, the φ of b-Si|StyCF$_3$ was 200 meV positive of the φ associated with unmodified b-Si, which was attributed to the induction of a strong, positive dipole at the b-Si|StyCF$_3$ surface (Table 2). After [Co] immobilization, the φ for all samples was 3.9 eV except b-Si|Pyr|[Co], where φ was 3.73 eV (Table 2). This difference was attributed to a relatively smaller surface coverage in b-Si|Pyr|[Co] samples that resulted in placement of the Co catalysts closer to the b-Si surface, ultimately changing its energetics. Photoelectrochemical characterization of all samples was performed in acidic aqueous conditions (0.1 M H_2SO_4, pH 1.5) under simulated 1-sun illumination using an ABET Technologies Sun 3000 Solar Simulator. In the dark, all electrodes (unmodified, aromatic-modified, and [Co] catalyst-aromatic-modified) showed negligible J (<2.5 mA cm^{-2}). V_{onset} (defined in their work as the potential required to achieve 1 mA cm^{-2}) was observed at relatively more negative potentials for all the b-Si|Aromatic electrodes in comparison with the unmodified b-Si electrodes (−0.31 V vs RHE). V_{onset} values of b-Si|Pyr and b-Si|Nap were −0.38 V vs RHE and −0.40 V vs RHE, respectively (<100 mV more negative than unmodified b-Si), and V_{onset} values of b-Si|Sty and b-Si|StyCF$_3$ were −0.52 V vs RHE and −0.61 V vs RHE, respectively (>200 mV more negative than unmodified b-Si) (Table 2). Additionally, b-Si|Pyr and b-Si|Nap electrodes reached a light-limited J of 35 mA cm^{-2} when polarized at potentials between −1.0 and −1.2 V vs RHE, while b-Si|Sty and b-Si|StyCF$_3$ approached a light-limited J of 35 mA cm^{-2} near −1.7 V vs RHE. Following immobilization of [Co] on the aromatic-modified b-Si photocathodes, V_{onset} values associated with the Co catalyst-aromatic-modified b-Si photocathodes were approximately −0.2 V vs RHE (Table 2). The authors indicated this observation was consistent with the V_{onset} being independent of the identity of the aromatic layer when the [Co] catalyst was present. At any given potential, voltammograms of b-Si|Aromatic|[Co] photocathodes showed no greater than 20 mA cm^{-2} of additional J compared to voltammograms of b-Si|Aromatic photocathodes. Assuming a surface coverage of 1 nmol cm^{-2} (similar to a reported b-Si|Ferrocene assembly),[221] the authors indicated that a TOF of at least 110 s^{-1} for the immobilized molecular catalysts would be required to sustain the additional J. In addition, intensity-modulated high-frequency resistivity was used to measure the V_{flatband}. Following modification of the b-Si surfaces with the aromatic layers and [Co] catalyst, V_{flatband} of all samples varied from +0.20 V to +0.26 V vs RHE (Table 2), indicating these surface modifications had minimal impact on the thermodynamics of the semiconductor band positions. These results indicate that kinetics associated with interfacial catalytic reactions can be decoupled from thermodynamics associated with underlying semiconductor, which the authors state is governed mainly by the molecular surface coverage. The values of V_{onset} and V_{flatband} measured using b-Si photocathodes modified only with the [Co] catalyst (b-Si|[Co]) (i.e., without the intervening aromatic molecular layer) were −0.17 V and +0.24 V vs RHE, respectively. Pseudo fill factors (pFF) were calculated to compare corrected and normalized J−V curves of b-Si|Aromatic|[Co] photocathodes against b-Si|[Co] photocathodes. Samples of b-Si|Nap|[Co] were the most kinetically competent with a pFF of 0.63, while samples of b-Si|Pyr|[Co], b-Si|CF$_3$|[Co], and b-Si|Sty|[Co] had pFFs of 0.57, 0.55, and 0.52, respectively. For comparison, samples of b-Si|[Co] had a pFF of 0.55 (Table 2). The authors proposed variations in pFF across samples were likely due to differences in surface coverages and π-coupling interactions, the latter of which has been shown to improve charge-transfer kinetics at the metal|molecule junctions. The authors indicated the degree of π-coupling depends on the size of the aromatics involved (where larger aromatics exhibit stronger coupling) and the electron density between them (where electron-rich/electron-poor pairs exhibit stronger coupling than electron-rich/electron-rich or electron-poor/electron-poor). Hence, b-Si|Nap|[Co] and b-Si|Pyr|[Co] displayed relatively higher pFFs due to the strong degree of π-coupling, and the pFF of b-Si|Nap|[Co] was larger than b-Si|Pyr|[Co] likely due to the relatively larger surface coverages associated with samples of Si|Nap|[Co] versus b-Si|Pyr|[Co]. The authors also hypothesized that π-coupling should be weaker in b-Si|Sty|[Co] and b-Si|StyCF$_3$|[Co] compared to the b-Si|Nap|[Co] and b-Si|Pyr|[Co] constructs due to the smaller size of the aromatic in the molecular layer, but b-Si|StyCF$_3$|[Co] contains stronger coupling due to the electron-poor nature of this moiety. These variations in pFFs for the b-Si|Aromatic|[Co] samples compared to pFF of b-Si|[Co] samples highlight the importance of additional interactions such as Van der Waals forces between the [Co] catalyst and aromatic layer.

Wang and co-workers covalently immobilized a Co tetraazamacrocyclic complex, an efficient and stable catalyst for HER, featuring a DCP (2,6-dicarboxypyridin-4-yl) anchoring group (denoted as Co(CR-DCP)) onto a TiO_2-protected p-Si electrode.[222] The TiO_2 was deposited onto p-Si via doctor-blading a paste of TiO_2 nanoparticles (18−20 nm) followed by annealing. Field-emission SEM images indicated the porous microstructure of the TiO_2 film had a film thickness of about 5.0 μm. The Si|TiO_2 electrode was then functionalized with the catalyst by soaking the electrode in a methanolic solution containing 1.0 mM of Co(CR-DCP) for 16 h to form the hybrid construct Si|TiO_2|Co(CR-DCP) (Figure 23a). XPS confirmed the presence of the catalyst on the surface, and inductively coupled plasma optical emission spectrometry (ICP-OES) analysis yielded a catalyst loading of 37.8 ± 5.8 nmol cm^{-2}. ATR-IR measurements further confirmed characteristic signals associated with the DCP anchor, pyridyl moieties, and Schiff base ligand. Linear sweep voltammetry was recorded using a three-electrode assembly in 0.1 M acetate buffer (pH 4.5) under 100 mW cm^{-2} illumination generated by a simulated-solar-light source equipped with a 400 nm long-pass filter. Under these conditions, Si|TiO_2|Co(CR-DCP) achieved a J = 682 μA cm^{-2} when polarized at 0 V vs RHE (Figure 23b) and an V_{onset} (defined in this work as the potential required to achieve a J = 0.01 mA cm^{-2}) of +0.37 V vs RHE. When the acetate buffer was replaced with phosphate buffer (pH 7) or borate buffer (pH 9), the J values when polarized at 0 V vs RHE were ∼0.15 and ∼0.10 mA cm^{-2}, respectively. In addition, replacement of the 5 μm TiO_2 porous layer with a 5 nm TiO_2 film deposited using ALD resulted in a decrease of J to 90 μA cm^{-2}, which was attributed to a relatively lower catalyst loading. EIS was performed at 0 V vs RHE under the same illumination condition used in the linear sweep voltammetry experiments. The Nyquist impedance data were modeled using a Randles equivalent circuit consisting of the solution resistance, interfacial electron transfer resistance (R_{ct}), and constant phase element to show the calculated value of R_{ct} decreased from 3336 Ω for bare Si|TiO_2 to 646 Ω for Si|TiO_2|Co(CR-DCP). Further, intensity modulated photocurrent spectroscopy, using electrodes polarized at 0 V vs RHE, indicated immobilization of Co(CR-DCP) on the surface of Si|TiO_2, yielded a surface electron transfer rate constant that was a factor of 10 higher, and a charge recombination rate constant that was decreased by the factor of 2. Controlled-potential polarization measurements performed at 0 V vs RHE under the same illumination conditions used in the linear sweep voltammetry and EIS experiments showed the Si|TiO_2|Co(CR-DCP) electrodes displayed a relatively steady J = 527 ± 35 μA cm^{-2} over 10 h. During the first 2 h of the controlled-potential polarization, this electrode yielded a FE of 80 ± 4% for H_2 evolution. Experiments recorded using Si|TiO_2|Co(CR-DCP) polarized at 0 V vs RHE, and illumination with monochromatic light from a LED lamp with wavelengths ranging from 420 to 800 nm, yielded EQE values ranging from 10.34−13.50%. ICP-OES, XPS, and ATR-IR results showed that 83% of the loaded Co catalysts remained intact on the TiO_2 surface after 10 h of controlled-potential polarization, and the authors ascribed this durability to the relatively stable attachment of the DCP anchoring group to the TiO_2 surface, where DCP can not only covalently bond to the Brønsted-acid sites (Ti-OH) of the surface through two carboxyl groups but also form coordination bonds involving pyridyl nitrogens and Lewis-acid sites of unsaturated surface titanium ions (i.e., exposed Ti^{n+} cations).

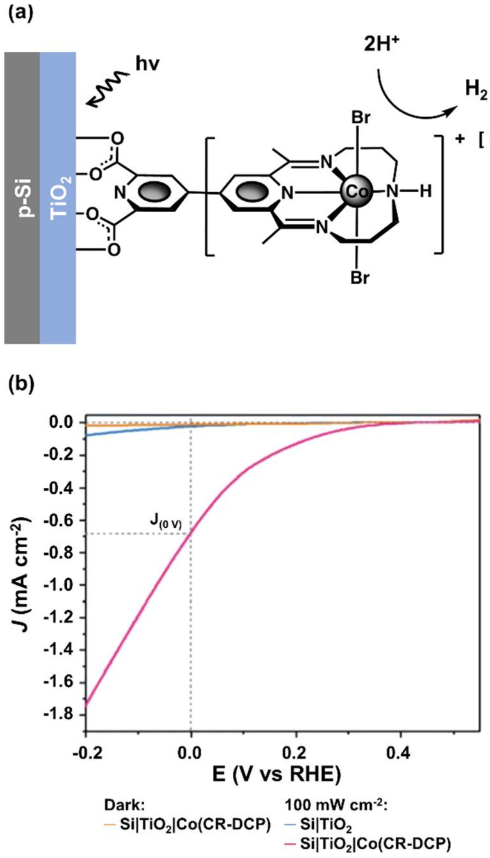

Figure 23. (a) Schematic representation of a cobalt-tetra-azamacrocyclic-functionalized Si photocathode. (b) Linear sweep voltammograms of Si|TiO_2 (blue) and Si|TiO_2|Co(CR-DCP) (pink) recorded in 0.1 M acetate buffer (pH 4.5) under 100 mW cm^{-2} illumination, at a scan rate of 10 mV s^{-1}, as well as Si|TiO_2|Co(CR-DCP) (yellow) recorded in 0.1 M acetate buffer (pH 4.5) in the dark, at a scan rate of 10 mV s^{-1}. Adapted from ref 222. Copyright 2021 Royal Society of Chemistry.

7.2. Photoelectrochemical CO_2 Reduction

One of the original reports on PEC reduction of CO_2 was by Parkinson and Weaver.[223] The authors describe the coupling of a p-type InP semiconductor, where the E_{CB} in aqueous solutions between pH 6 and 8 is more negative than the thermodynamic potential required for the reduction of CO_2, with formate dehydrogenase enzymes, which are selective for the formation of $HCOO^-$. This work showed that photogenerated electrons from a semiconductor could be transferred, via use of an electron mediator (methyl viologen), to the enzyme dissolved in solution, resulting in selective reduction of CO_2 to $HCOO^-$.

Arai, Sato, and co-workers described the PEC conversion of CO_2 to HCOOH in aqueous conditions using a Zn-doped p-type InP photocathode modified with a Ru-based polymer, $[Ru(L-L)(CO)_2]_n$ (RCP), where L-L is a diamine ligand

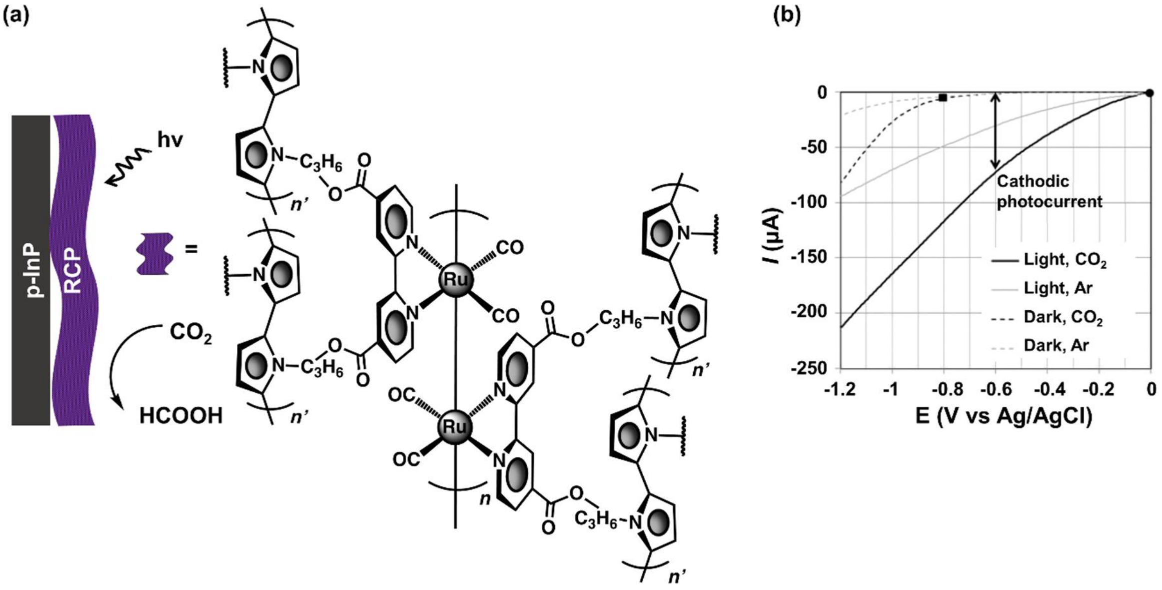

Figure 24. (a) Schematic representation of a Ru-based polymeric film on p-InP. (b) Linear sweep voltammograms of InP|RCP electrodes recorded in Ar-saturated aqueous media (pH 4) in the dark (dashed gray) or under visible light (400 < λ < 800 nm) illumination (solid gray), as well as of InP|RCP electrodes recorded in CO_2-saturated aqueous media (pH 4) in the dark (dashed black) or under visible light (400 < λ < 800 nm) illumination (solid black). Adapted from ref 224. Copyright 2010 Royal Society of Chemistry.

(Figure 24a).[224] The polymeric film was formed on the InP surfaces through photoelectropolymerization of Ru[(L-L)-$(CO)_2Cl_2$] in a 0.1 M tetrabutylammonium perchlorate MeCN solution. Controlled-potential polarization at −0.60 V vs Ag/AgCl was performed using an RCP-modified p-InP (InP|RCP) electrode immersed in CO_2-saturated aqueous media (pH 4) under visible-light irradiation from a Xe lamp equipped with an optical 400 nm long-pass filter. Under these conditions, the InP|RCP photocathodes achieved a current of 75 μA (Figure 24b) and produced 0.14 mM of $HCOO^-$ over 3 h, with a *FE* of 34% and a TON for HCOOH formation from CO_2 per RCP of >12. In addition, a higher *FE* for $HCOO^-$ production (62%) was obtained using InP|RCP photocathodes prepared via an alternative polymerization process, where the surface-attached polymer films were formed via a two-step process that included cathodic photoelectropolymerization and anodic electropolymerization of Ru[(L-L)$(CO)_2Cl_2$]. During this two-step process, the authors postulated that Ru−Ru bonds were formed within the polymeric film via the cathodic photoelectropolymerization process, and the pyrrole polymerization was accelerated by the anodic electropolymerization process, with the pyrrolic polymerization further reinforcing the contact between the molecular coating and the semiconductor surface. Photoelectrochemical experiments conducted using $^{13}CO_2$ and D_2O isotopes indicated that $HCOO^-$ was indeed formed from CO_2 and water, as only isotope-labeled products were detected using liquid chromatography time-of-flight mass spectrometry.

To improve the aforementioned construct, Sato, Arai, and co-workers deposited a polymer formed from a mixture containing two Lehn-type Ru-based catalysts, one bearing a diphosphonate-anchoring moiety (Ru(4,4′-diphosphate-ethyl-2,2′-bipyridine)$(CO)_2Cl_2$) (abbreviated here as RuCA) to facilitate surface attachment and improve electron transfer from the semiconductor to Ru catalysts, and another bearing a pyrrolyl unit (Ru[4,4′-di(*1H*-pyrrolyl-3-propylcarbonate)-2,2′-bipyridine][CO][MeCN]Cl_2) (abbreviated here as RuCE) onto an InP surface (Figure 25a).[225] Upon chemical polymerization of RuCA and RuCE in solution (forming polyRuCA+polyRuCE), aliquots of the polymeric solution were dropcasted onto InP, resulting in a total catalyst loading of 0.324 μmol per 3 cm^{-2} semiconductor sample (equivalent to 108 nmol cm^{-2}). The polyRuCA+polyRuCE-modified InP photocathodes (InP|polyRuCA+polyRuCE) were immersed in a CO_2-saturated aqueous solution, under simulated solar illumination (Xe light source at an intensity of 70 suns with an optical 400 nm long-pass filter) and polarized at −0.40 V vs Ag/AgCl for 1 h. The assembly was capable of reducing CO_2 to $HCOO^-$ (Figure 25b), as confirmed using ion chromatography time-of-flight mass spectroscopy (IC TOF-MS), with a *FE* of 78%. The InP|polyRuCA+polyRuCE photocathode was also coupled with a water-oxidizing photoanode (P25 TiO_2, anatase) to drive CO_2 reduction in the absence of an external bias. Under simulated 1-sun illumination (AM 1.5 G, 100 mW cm^{-2}) and in the presence of a CO_2-saturated 10 mM $NaHCO_3$ aqueous solution, the photocathode was stable for 24 h, yielding a per Ru catalyst TON of >17 for $HCOO^-$ formation from CO_2. Although additional products were detected (H_2 and CO), the *FE* of the InP|polyRuCA+polyRuCE photocathode in the two-electrode configuration was 70% for $HCOO^-$. PEC experiments conducted using $^{13}CO_2$ and D_2O isotopes confirmed that $HCOO^-$ was indeed generated from the input CO_2 and water, and the STF conversion efficiency was 0.04%.

Following on their previous efforts, Arai and co-workers constructed PEC constructs for CO_2 reduction by substituting the InP light-absorbing material with Cu_2ZnSnS_4 (CZTS), which consists of abundant and relatively low-cost elements.[226] The relatively narrow-band gap (1.5 eV) CZTS semiconductor was modified with the same Ru-containing polymer described in the previous example.[225] Aliquots of the Ru-containing polymer were deposited on the CZTS surfaces following chemical polymerization of a mixture containing RuCA and RuCE (structures in Figure 25a). The polyRuCA+polyRuCE-modified CZTS constructs (CZTS|polyRuCA+polyRuCE)

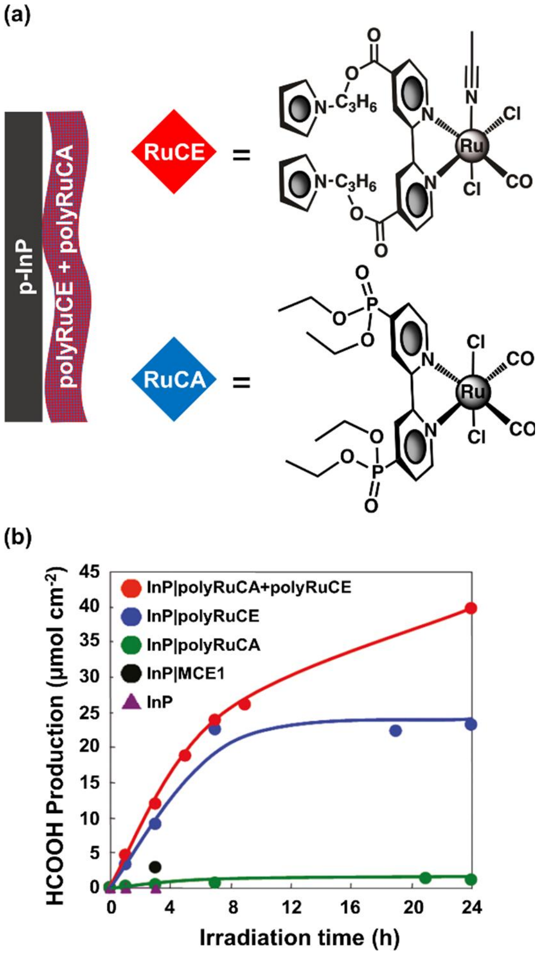

Figure 25. (a) Schematic representation of a polymeric film composed of a mixture of two Lehn-type Ru-based molecular complexes. (b) Amount of HCOOH produced by InP|polyRuCA+polyRuCE (red circles), InP|polyRuCE (blue circles), InP|polyRuCA (green circles), InP|MCE1 (*MCE1* is an analog polymer of polyRuCE, but with two Cl and two CO ligands on its monomer) (black circles), and unmodified InP (purple triangles) electrodes in a CO_2-saturated aqueous solution under 70-sun illumination for 24 h and polarized at −0.40 V vs Ag/AgCl. Adapted with permission from ref 225. Copyright 2011 American Chemical Society.

were characterized using XRD, X-ray fluorescence, electron probe X-ray microanalysis, SIMS, and photoelectron spectroscopy in air (PESA), yielding a Ru surface loading of 0.33 μmol cm^{-2}. Controlled-potential polarization using the CZTS|polyRuCA+polyRuCE photocathodes was performed in CO_2-saturated water under visible-light irradiation (Xe lamp with an optical 400 nm long-pass filter, with the light intensity adjusted to an intensity of ∼70 suns) at $V = -0.40$ V vs Ag/AgCl. Under these conditions, the CZTS|polyRuCA+polyRuCE photocathodes achieved a $J \approx 0.25$ mA cm^{-2} and produced 0.29 mM of $HCOO^-$ over 3 h, corresponding to a *FE* of 82% for $HCOO^-$ formation and a reported per Ru TON of >5. In addition, the authors demonstrated that hole mobility of the sulfide semiconductors could be improved by introducing Se atoms (<0.1%) into the material during fabrication.[227] Ru polymer-modified assemblies formed using $Cu_2ZnSnSe_4$ (CZTSe|polyRuCA+polyRuCE) and tested under identical experimental conditions achieved twice the *J* as compared to the CZTS|polyRuCA+polyRuCE assemblies, thus doubling the amount of $HCOO^-$ generated over 3 h, while achieving a *FE* for $HCOO^-$ production of 82%.

Arai and co-workers also developed a device composed of a dropcasted polyRuCE (as a CO_2 reduction catalyst) and IrO_x (as a H_2O oxidation catalyst), with each catalyst coating one side of a triple-junction amorphous silicon-germanium (SiGe-jn) semiconductor (Figure 26a).[228] The E_{CB} and E_{VB} values (−0.52 V vs RHE and 1.58 V vs RHE, respectively) of SiGe-jn are thermodynamically adequate for driving the catalytic reactions, and its p−i−n and tunnel junctions facilitate charge separations and transfer of photoexcited electrons and holes. Photoelectrochemical characterization of the hybrid PEC cell (IrO_x|SiGe-jn|polyRuCE) submerged in a CO_2-saturated aqueous solution (0.1 M phosphate buffer, pH 6.4) under simulated 1-sun illumination (AM 1.5 G, 100 mW cm^{-2}) indicated the PEC cell produced $HCOO^-$, as evidenced using IC TOF-MS and GC, with a STF of 4.6%. Under the conditions stated above, the *FE* for $HCOO^-$ production was 93% (Figure 26b); however, the PEC cell was also capable of generating $HCOO^-$ with a *FE* of 76% when subject to gas streams containing a mixture of CO_2 (93%) and O_2 (7%).

Mayer, Grätzel, and co-workers demonstrated that CO_2 reduction can be photoelectrochemically driven using photocathodes composed of Lehn-type Re-based catalysts that were covalently attached through phosphonate linking groups to a mesoporous-TiO_2 coating deposited onto an AZO-modified FTO substrate interfaced with a Cu_2O semiconductor (Cu_2O|FTO|AZO|$TiO_{2,meso}$|Re) (Figure 27a).[229] The TiO_2 layer acts as a protective coating and as a scaffold to support molecular catalysts, while the AZO layer was included to create a p−n junction with Cu_2O. Additionally, a methylene bridge was added between the phosphonate and bipyridyl moieties to minimize the modification of the electronic structure of the catalyst. The Cu_2O|FTO|AZO|$TiO_{2,meso}$|Re surfaces were characterized with ATR-IR and XP spectroscopies, confirming the presence of the immobilized Re catalysts before and after PEC operation in a MeCN solution containing 0.1 M tetrabutylammonium hexafluorophosphate ($TBAPF_6$) as the supporting electrolyte under a CO_2 atmosphere and 1-sun intensity illumination using a Xe lamp equipped with a metal grid (serving as a neutral density filter) and a KG3 filter. The highly porous structure of the mesoporous-TiO_2 film (4.5−5 μm thickness) enabled a relatively high loading of the rhenium catalyst (∼85 nmol Re cm^{-2} as determined using ICP-OES), resulting in a J = 2.5 mA cm^{-2} when a Cu_2O|FTO|AZO|$TiO_{2,meso}$|Re photocathode was polarized at −1.90 V vs Fc^+/Fc, a value 40 times higher than that achieved using analogous assemblies containing a planar-TiO_2 coating (Cu_2O|FTO|AZO|$TiO_{2,flat}$|Re) in place of the mesoporous-TiO_2 coating (Figure 27b). The molecular-modified construct generated CO with a *FE* of 80−95% as confirmed using GC, with a per Re TON for CO production exceeding 70. However, controlled-potential polarization conducted using a Cu_2O|FTO|AZO|$TiO_{2,meso}$|Re photocathode polarized at −1.90 V vs Fc^+/Fc indicated there was a gradual decrease in activity after 2 h under chopped (1 Hz) simulated 1-sun illumination (AM 1.5 G, 100 mW cm^{-2}). XPS analysis of the Cu_2O|FTO|AZO|$TiO_{2,meso}$|Re photocathodes following 2 h of PEC operation indicated no changes in the oxidation state of the Re and confirmed the persistence of elements attributable to the immobilized catalyst species. ICP-OES also confirmed the amount of Re on the samples prior to and following PEC operation was unchanged, and the ATR-IR spectrum showed

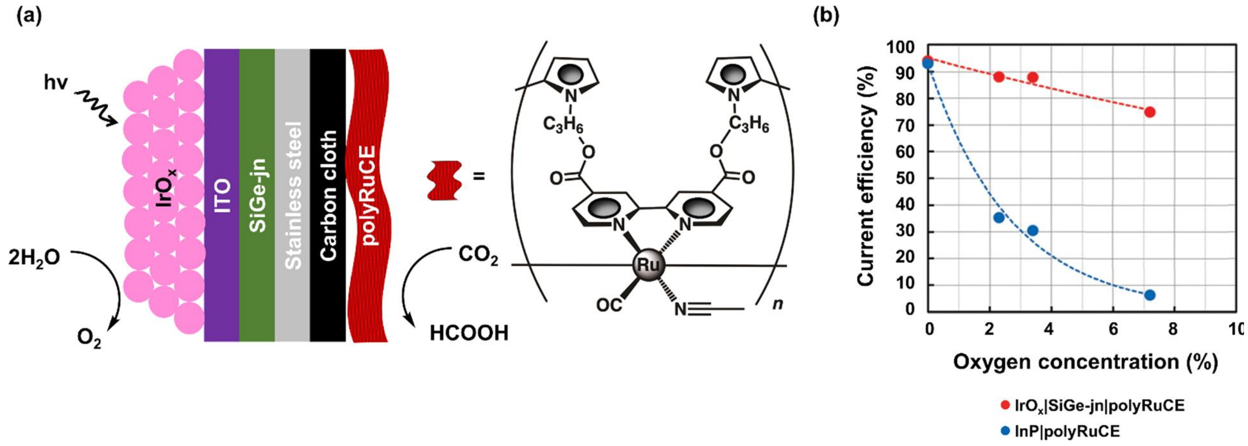

Figure 26. (a) Schematic representation of a photoelectrochemical cell containing triple-junction amorphous SiGe-jn photocathode interfaced with a Ru polymer catalyst layer and a photoanode consisting of ITO anode decorated with IrO_x. (b) Current efficiency for $HCOO^-$ formation of InP|polyRuCE (blue) electrode and IrO_x|SiGe-jn|polyRuCE (red) cell in 0.1 M phosphate buffer (pH 6.4) saturated with CO_2 with different O_2 concentrations, under 100 mW cm^{-2} illumination for 1 h with no applied bias potential. Adapted with permission from ref 228. Copyright 2015 Royal Society of Chemistry.

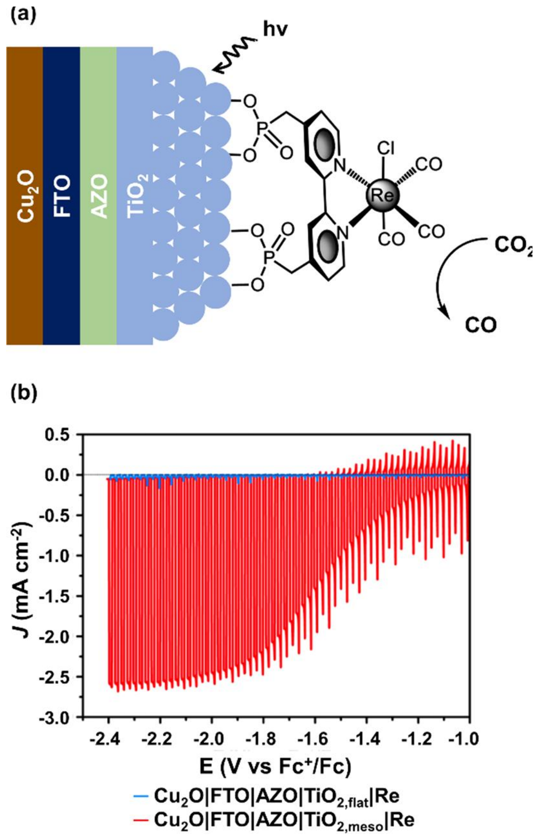

Figure 27. (a) Schematic representation of a phosphonate-modified Lehn-type Re-based catalyst on Cu_2O photocathodes. (b) Linear sweep voltammograms of $Cu_2O|FTO|AZO|TiO_{2,flat}|Re$ (blue) and $Cu_2O|FTO|AZO|TiO_{2,meso}|Re$ (red) recorded in CO_2-saturated MeCN under 100 mW cm^{-2} illumination with a chopper at a frequency of 1 Hz and at 10 mV s^{-1}. Adapted with permission from ref 229. Copyright 2016 American Chemical Society.

no changes in the carbonyl stretches frequencies. However, there was a bleaching of the bipyridine signals in the ATR-IR spectrum, suggesting the immobilized catalysts underwent structural changes involving the bipyridine ligand.

ReCl(*N*-methyl-*N*′-2-pyridyl-benzimidazol-2-ylidine)$(CO)_3$ and ReCl(*N*-methyl-*N*′-2-pyrimidyl)-benzimidazol-2-ylidine)-$(CO)_3$ complexes, known electrocatalysts for CO_2 reduction,[230−232] were studied by Wang, Li, and co-workers by coupling Si nanowire photocathodes (to leverage its nanostructured morphology) with an organic electrolyte solution containing the Re catalysts.[233] Controlled-potential polarization using the Si nanowire photocathodes immersed in a CO_2-saturated MeCN solution containing 5% H_2O, 0.1 M $TBAPF_6$ as the supporting electrolyte and 1 mM of the Re-based pyrimidyl analog and polarized at −1.51 V vs Fc^+/Fc for 4 h under illumination (Xe lamp, 113 mW cm^{-2}) generated CO with a *FE* of 68%, a per Re TON for CO of 20.4, and a J = 0.2 mA cm^{-2}. However, experiments performed using identical conditions except for the use of the Re-based pyridyl analog instead of the pyrimidyl analog resulted in a *FE* of 20%, a TON per Re of 18.1, and a J = 1.4 mA cm^{-2}. The selectivity of the Re catalysts to drive CO_2 reduction decreased when the Si nanowire photocathode was replaced with $[Ru(4,4'\text{-dimethyl-}2,2'\text{-bipyridine})_3]^{2+}$ as a molecular photosensitizer and triethanolamine (TEOA) as a sacrificial electron donor. While the molecular Re catalysts were not purposefully attached to the semiconductor in this report, analysis of the Si nanowires following PEC operation using diffuse reflectance FTIR spectroscopy indicated the Re-based pyrimidyl analogs were adsorbed onto the nanowire surfaces, a result the authors associated with the activity and selectivity of CO_2 reduction. In the case of the Re-based pyridyl analogs, negligible amounts of the surface-adsorbed catalyst were found on the Si nanowire surfaces following PEC operation.

Sekizawa and co-workers developed PEC assemblies each featuring a multiheterojunction composed of Cr_2O_3, N,Zn-codoped Fe_2O_3, and TiO_2 as well as four separate dropcasted Ru-based Lehn-type catalysts at a loading of 70 nmol cm^{-2}.[234] Fe_2O_3 is an abundant material and relatively low-cost semiconductor, whose band gap is 2.1 eV and therefore can absorb a substantial amount of solar light. Both Cr_2O_3 and TiO_2 were present with the intention of tuning the band bending of the N,Zn-codoped Fe_2O_3, with the former improving hole transfer processes, and the latter protecting the unstable Fe_2O_3 surface as well as improving electron transfer rates by forming a p−n junction.[235] The Ru catalyst-modified constructs were characterized via SEM, scanning transmission electron microscopy (STEM), EDX, and XRD. Controlled-potential polarization using the Ru catalyst-modified photocathodes immersed in a CO_2-saturated aqueous solution (0.1 M $KHCO_3$, pH 6.6) and polarized at +0.10 V vs RHE for 1 h under simulated 1-sun illumination (AM 1.5 G, 100 mW cm^{-2}) indicated the photocathodes reduced CO_2 to HCOOH and CO and cogenerated H_2. Among the four monomeric Ru catalysts used in this study, each featuring different substituents on the metal center and on the 4,4′-positions of bipyridine ligands, photocathodes modified with Ru catalysts bearing a MeCN ligand on the metal and pyrrolyl-3-propylcarbonates on the bipyridine ligands exhibited the highest activity. Nonetheless, for all assemblies that contained one of the four monomeric catalysts, the maximum *J* of about 0.1 mA cm^{-2} decreased by 50% within 1 h while operating at +0.10 V vs RHE under continuous illumination. In contrast, a Ru polymer-modified photocathode, constructed by depositing a Ru polymer formed via polymerization of the monomeric Ru catalyst analog featuring the MeCN ligand and pyrrolyl substituent onto the semiconductor surface, displayed a stable $J \approx 0.15$ mA cm^{-2} when studied under otherwise identical conditions, resulting in an overall higher catalytic activity and increased amount of CO_2 reduction products (HCOOH and CO). Controlled-potential polarization using the Ru polymer-modified photocathode immersed in a CO_2-saturated aqueous solution (0.1 M $KHCO_3$, pH 6.6) and polarized at $V = +0.10$ V vs RHE for 13 h under illumination resulted in the generation of 12 μmol cm^{-2} (0.25 nmol cm^{-2} s^{-1}) of HCOOH, 9.2 μmol cm^{-2} (0.19 nmol cm^{-2} s^{-1}) of CO, and 1.9 μmol cm^{-2} (0.4 nmol cm^{-2} s^{-1}) of H_2, as well as a calculated per Ru TON for CO_2 reduction of 304. Combination of the Ru polymer-modified photocathode with a $SrTiO_3$ photoanode allowed water splitting in a two-electrode configuration without the need of an external bias. The PEC cell displayed a stable *J* with an average value of 102 μA cm^{-2} over 3 h of operation. After 1 h of illumination, the *FE* were 79% for HCOOH, 16% for CO, and 6% for H_2. This two-electrode PEC cell achieved a STF conversion efficiency of 0.15%.

Meyer and co-workers prepared photocathodes capable of reducing CO_2 to $HCOO^-$ using a binary p−n junction consisting of n-type GaN nanowire arrays deposited on n^+−p−p^+ Si (forming a p−n junction) with a ∼0.25 nm NiO overlayer deposited via ALD.[236] The NiO-coated surfaces were functionalized using a layer-by-layer assembly method where the NiO-coated electrodes were immersed sequentially in solutions containing a phenylene diamine modified with carboxylic acid groups, $ZrOCl_2$, a phosphonic acid-modified Ru polypyridyl chromophore, $ZrOCl_2$, and finally a carboxylic acid-modified Ru-based Lehn-type catalyst to obtain the desired molecular assembly (Figure 28). A final ∼1.2 nm overlayer of NiO was added via ALD to stabilize the carboxylate binding groups and the Zr bridging groups from decomposition in aqueous media. The Ru catalyst loading was determined to be 17 nmol cm^{-2} using UV−vis absorption spectroscopy of solutions of the Ru catalysts following desorption from the surface in a 1 M NaOH solution. The molecular-modified photocathodes achieved a $J \approx 1.1$ mA cm^{-2} over 20 h in a CO_2-saturated aqueous solution (50 mM $NaHCO_3$, pH 6.8) under simulated AM 1.5 G illumination (Xe Lamp, 100 mW cm^{-2}) when polarized at −0.25 V vs RHE. This resulted in a *FE* for $HCOO^-$ production of up to 64%.

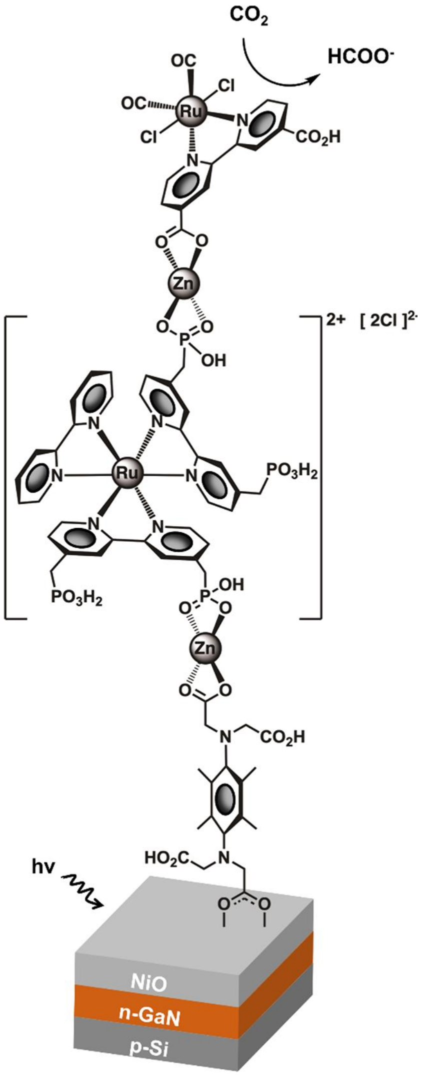

Figure 28. Schematic representation of a multimolecular system on n-GaN nanowires grown on p-Si. Adapted from ref 236.

A recent report by Reisner and co-workers described a precious-metal-free molecular-modified photocathode for solar driven reduction of CO_2 to CO and $HCOO^-$ in aqueous conditions.[237] Modification of Si surfaces with a mesoporous-TiO_2 layer (∼6 μm thick) provided a protective coating as well as a high-surface area scaffold for achieving relatively high loadings of Co(II) bis(terpyridine) catalysts bearing phosphonate functional groups (CotpyP). In this work, CotpyP modification was achieved by exposing mesoporous TiO_2-coated Si to a methanolic solution containing the catalyst precursors. The E_{CB} of the mesoporous TiO_2-modified Si photoelectrode (Si|mesoTiO$_2$) is positioned at −0.10 V vs NHE, and the midpoint potential associated with the active form of CotpyP occurs at −1.40 V vs NHE, highlighting the thermodynamic mismatch of the component parts. Nonetheless, the authors postulated that following photoexcitation, electrons were transferred from the Si substrate through the TiO_2 layer to the anchored Co catalysts. The loading of Co catalysts was determined to be 45 ± 7.4 nmol cm^{-2} via ICP-OES. Linear sweep voltammograms of the CotpyP-mesoporous TiO_2-modified Si photocathodes (Si|mesoTiO$_2$|CotpyP) recorded in a 6:4 MeCN:H_2O solution containing 0.1 M tetrabutylammonium tetrafluoroborate as the supporting electrolyte and under UV-filtered illumination (Newport Oriel Xe lamp with an AM 1.5 G, an infrared water filter, and a 400 nm long-pass filter, 100 mW cm^{-2}) reached a saturated $J \approx 225$ μA cm^{-2} at −0.85 V vs Fc$^+$/Fc. Controlled-potential polarization using Si|mesoTiO_2|CotpyP photocathodes subjected to the same electrolyte and illumination conditions previously listed and polarized at −1.0 V vs Fc$^+$/Fc resulted in the formation of CO, H_2, and $HCOO^-$. The overall *FE* was 77% for all products, with a *FE* for CO of 48%, a TON per Co for CO of 159, and a TOF for CO of 16 h^{-1} (0.0044 s^{-1}) over 8 h. The molecular integrity of the Co catalysts was addressed via ATR-IR and XPS measurements, which showed unchanged ATR-IR and XP spectra collected before and after PEC operation. The latter method revealed no detectable presence of reduced/elemental Co species on the Si|mesoTiO_2 surfaces.

A QD-based photoelectrode for CO_2 reduction was constructed by Tian, Hammerström, and co-workers, where $CuInS_2$ QDs (4 nm diameter), materials free of heavy metals, were adsorbed onto mesoporous NiO-coated FTO electrodes, followed by functionalization with Lehn-type Re catalyst containing phosphonate anchoring groups (Figure 29a).[238] Immobilization of the QDs and Re catalysts was confirmed using UV−vis spectroscopy, FTIR spectroscopy, SEM, and EDX, and a loading of 8.2 nmol cm^{-2} was determined for the Re catalyst. The Re catalyst-$CuInS_2$ QD-modified NiO photocathodes (NiO|$CuInS_2$-QD|Re) achieved a $J = 25$ μA cm^{-2} when studied in a CO_2-saturated dimethylformamide (DMF) solution containing 0.1 M $TBAPF_6$ as the supporting electrolyte and polarized at −0.87 V vs NHE for 5 min under simulated solar illumination (1 sun from a 17 W LED, 420−750 nm), alternating between illuminated and nonilluminated conditions in ~30 s intervals (Figure 29b). A *J* of ~10 μA cm^{-2} was observed using NiO sensitized by $CuInS_2$ QDs without the Re catalyst (NiO|$CuInS_2$-QDs), whereas negligible *J* was observed using NiO functionalized with the Re catalyst without $CuInS_2$ QDs (NiO|Re). CO was the only product detected via GC analysis of the headspace gas after 100 min of PEC operation using NiO|$CuInS_2$-QD|Re, with a *FE* of 32% and a per Re TON for CO of 11.

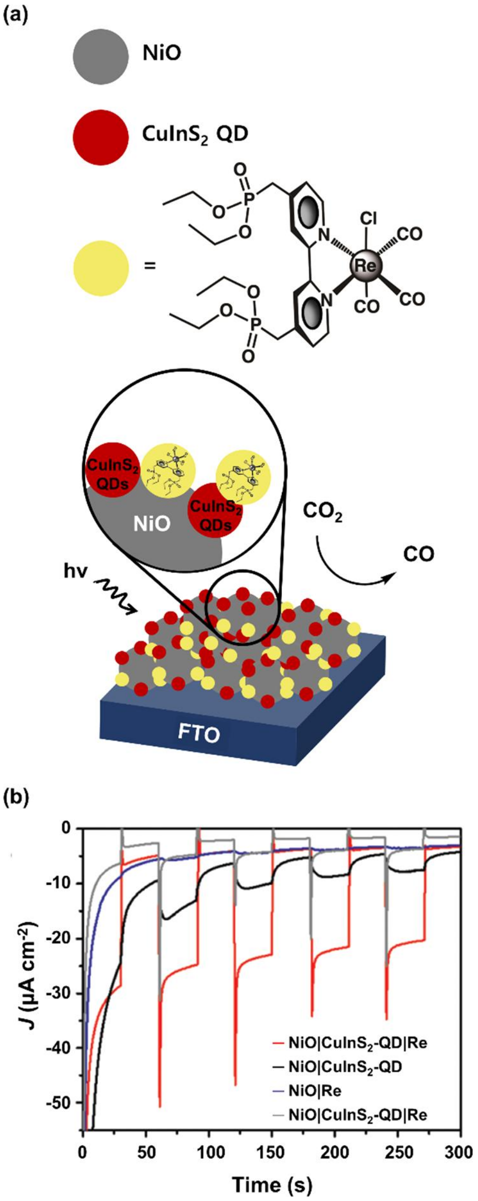

Figure 29. (a) Schematic representation of NiO photocathode functionalized with $CuInS_2$ quantum dots and Lehn-type Re-based catalysts. (b) Controlled-potential polarization of NiO|$CuInS_2$-QD|Re (red), NiO|$CuInS_2$-QD (black), and NiO|Re (blue) electrodes recorded in CO_2-saturated dimethylformamide under 1-sun illumination (alternating between illuminated and nonilluminated conditions in ~30 s intervals) and polarized at −0.87 V vs NHE. Controlled-potential polarization of NiO|$CuInS_2$-QD|Re recorded under Ar in place of CO_2 (gray) is also included. Adapted with permission from ref 238. Copyright 2019 Royal Society of Chemistry.

8. EXAMPLES INVOLVING LIGHT-ABSORBING NANOPARTICLES AND NANORODS MODIFIED WITH MOLECULAR CATALYSTS

The following examples describe molecular-catalyst-modified semiconductor nanoparticles or nanorods (NRs) suspended in solutions containing sacrificial sources of electrons. Unlike the 'type-1' photosynthetic assemblies described thus far, which spatially separate the cathodic and anodic half-reactions, the systems described in this section are either 'type-2' photosynthetic assemblies that employ charge-transfer selectivity, photocatalytic assemblies that drive energetically downhill reactions without storing photochemical energy, or, under some circumstances, a combination of both.[42]

8.1. Molecular-Catalyst-Modified Semiconductor Nanoparticles and Nanorods for H_2 Production

Mulfort, Chen, and co-workers have reported the application of molecular-catalyst-modified nanoparticle semiconductors for H_2 production. In this work, CdSe QDs were initially coated with a ZnS shell (for enhanced photostability) and then functionalized with a pyridine-phosphonate cobaloxime catalyst (Figure 30a).[239] A maximum average surface coverage of 66 catalyst molecules per QD was estimated using UV−vis absorption measurements. In addition, transient absorption spectroscopy measurements (Ti:sapphire, pump pulse 415 nm, and 300 μm in diameter) conducted using the cobaloxime-modified QDs suspended in toluene indicated electron transfer from excited QDs to cobaloxime catalysts occurred in ~105 ps, with a charge recombination time of ≫3 ns. Proton reduction experiments were carried out in toluene containing triethylamine (TEA) hydrochloride as a proton source, TEOA as a sacrificial electron donor, and the cobaloxime-modified QDs at a concentration of 10 μM under illumination for 10 h using a 100 W Xe lamp equipped with a 29 cm water column used as a

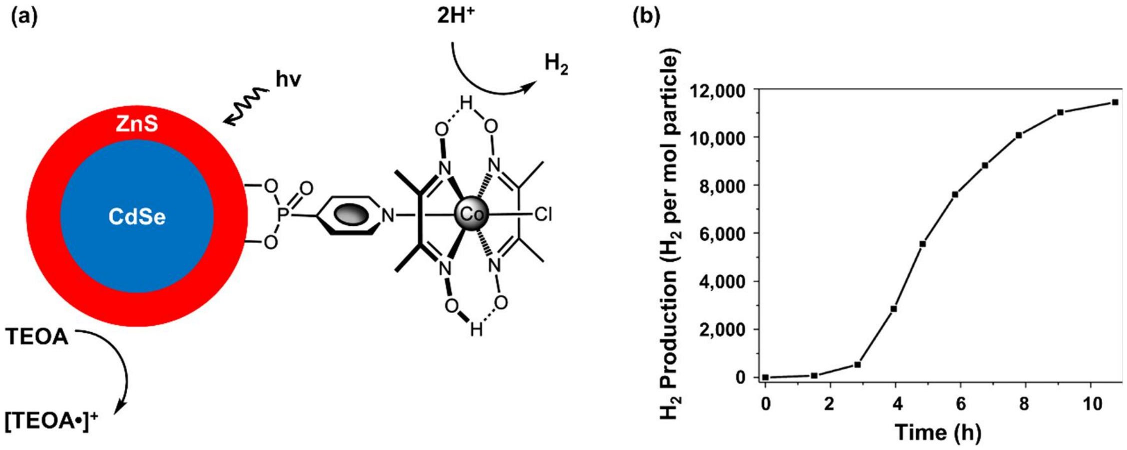

Figure 30. (a) Schematic representation of a CdSe quantum dot, protected with a ZnS shell and a phosphonate-functionalized cobaloxime. (b) Amount of H_2 produced by CdSe quantum dots (10 μM) protected with a ZnS shell and a phosphonate-functionalized cobaloxime in toluene with triethylamine (TEA) and triethanolamine (TEOA) illuminated for 10 h with a 100 W Xe lamp equipped with a 400 nm long-pass filter. Adapted with permission from ref 239. Copyright 2012 American Chemical Society.

400 nm long-pass filter. GC analysis of the headspace gas indicated that ~11,000 mol of H_2 per mole of QD particles were generated after 10 h of illumination (Figure 30b), equivalent to a TON of 10,000 per QD. Absence of either the QD or cobaloxime catalyst resulted in no detectable H_2 production. The authors reported that during the first 2 h of the experiment there was a relatively low rate of H_2 production (<1,000 mol of H_2 per mol of QD particles), consistent with multiple equilibria involved in the conversion of Co^{III} to Co^{II} followed by a secondary electron transfer from Co^{II} to Co^{I} to generate the active cobalt species. Following these experiments, toluene was replaced with methanol (MeOH) to precipitate and remove the QDs, and the UV−vis spectra of the resulting solution containing the cobaloxime catalysts indicated degradation of the complexes. However, EDX and transmission electron microscopy (TEM) revealed that no Co nanoparticles were formed. Comparisons of absorption spectra collected after photochemical operation to those collected before showed a blue shift of the lowest energy exciton peak of the QD and reduced intensities at higher energy absorption bands. These results indicated a decrease of the average QD size due to photocorrosion.

Dukovic, King, and co-workers adsorbed a [FeFe]-hydrogenase I purified from *Clostridium acetobutylicum* (abbreviated by the authors as CaI), onto CdS NRs capped with 3-mercaptopropionate (MPA), which promoted the adsorption of CaI on the QD and stabilized inorganic materials in aqueous buffers (Figure 31a).[26] The CdS NRs had an average diameter of 4.5 nm and length of 30 nm, as measured using TEM. Photochemical experiments were carried out in a pH 7 buffer solution containing 50 mM Tris-HCl, 5 mM NaCl, 100 mM ascorbic acid (AA) as a sacrificial donor, 5% glycerol, and varying concentrations of the suspended hydrogenase-modified CdS NRs under illumination from a 405 nm LED. The headspace H_2 produced in these experiments was analyzed using GC following 10 min of illumination. When the CdS NRs, AA, or hydrogenases were absent, no H_2 production was observed. Electron transfer between the CdS NRs and the surface-adsorbed hydrogenases was optimized by varying the CdS:CaI ratios, and the maximum amount of H_2 was produced at concentrations of 19 nM CdS and 12.5 nM CaI (ratio 1 CdS:0.67 CaI). Similarly, hole-transfer was optimized by varying the concentration of AA and measuring TOFs at two different light intensities (800 and 2000 μE m^{-2} s^{-1}). These results indicated that a minimum concentration of 10−25 mM in AA was required to achieve maximal photochemical rates of H_2 production. The system displayed a linear relationship between the illumination intensity (up to ~3000 μE m^{-2} s^{-1})

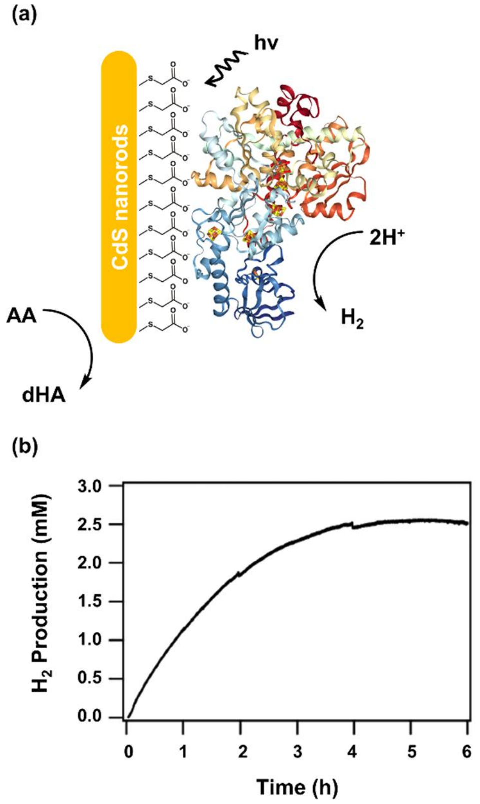

Figure 31. (a) Schematic representation of 3-mercaptopropionate capped CdS nanorods containing a surface-immobilized [Fe-Fe]-hydrogenase. (b) Amount of H_2 produced by 3-mercaptopropionate capped CdS nanorods (14 mM) containing a surface-immobilized [Fe-Fe]-hydrogenase (9 nM) in 50 mM Tris-HCl buffer (pH 7) with 100 mM ascorbic acid, under 800 μE m^{-2} s^{-1} illumination for 6 h. Adapted with permission from ref 26. Copyright 2012 American Chemical Society.

and the TOF of the hydrogenase-modified CdS NPs while maintaining a constant quantum yield of 20%. These results indicate the TOF is limited by the photon flux. The highest TOF measured was ~350 s^{-1} at ~3000 μE m^{-2} s^{-1}. Longer term photochemical H_2 evolution activity was assessed using a pH 7 buffer solution containing 50 mM Tris-HCl, 5 mM NaCl, 5% glycerol, 100 mM AA, 14 nM CdS, and 9 nM CaI, under 800 μE m^{-2} s^{-1} (approximately AM 1.5 G) illumination for 6 h. The peak rate of H_2 production occurred within the first 30 min, followed by a slow decrease in rate, until at 4 h there was no further accumulation of product (Figure 31b). The TON for H_2 production under these experimental conditions was calculated to be 10^6 per CdS:CaI. UV−vis spectroscopy indicated that the AA was oxidized only in the presence of CaI; however, control experiments showed that when the CdS:CaI complex was illuminated for the same 4 h time period, there was profound inactivation (80% reduction) of the enzyme with a kinetic profile similar to the previously described decline in H_2 production rate. Further control experiments showed that increasing the concentration of MPA had an adverse effect on the rate of H_2 production, while increasing the concentrations of Cd^{2+} had no effect, leading the authors to hypothesize that prolonged illumination resulted in loss of MPA from the NR surface, which in turn led to loss of CaI activity. Yet, this loss was not affected by AA. Thus, if MPA is oxidized from the surface by photoexcited holes, this process could be in competition with hole-scavenging by AA, and the resulting defect sites may act as "electron sinks".

Dukovic, King, and co-workers have also reported the use of MPA-capped CdS nanocrystals and a [Mo-Fe] nitrogenase from *Azotobacter vinelandii* for photoactivating the reduction of nitrogen to ammonia.[240−242] Although the conversion of nitrogen to ammonium is an exothermic process (Table 1), and hence technically not a photosynthetic or fuel forming reaction, it is a reaction of significant biological and industrial importance. Together with climate change and biodiversity loss, the nitrogen cycle is one of three planetary systems that have exceeded the boundaries of a safe operating space for humanity.[243,244]

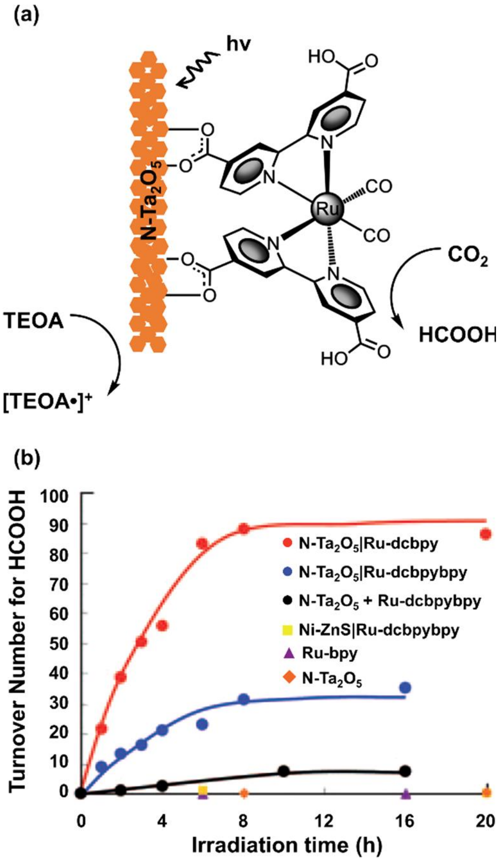

Figure 32. (a) Schematic representation of p-type N-Ta_2O_5 nanoparticle with a carboxilate-modified Lehn-type Ru-based catalyst. (b) Turnover number for HCOOH formation by N-Ta_2O_5|Ru-dcbpy (red circles), N-Ta_2O_5|Ru-dcbpybpy (blue circles), Ni-ZnS|Ru-dcbpybpy (yellow squares), and N-Ta_2O_5 (orange diamonds) nanoparticles as well as N-Ta_2O_5 nanoparticles with Ru-dcbpybpy in solution (back circles) and 0.05 mM Ru-bpy (purple triangles) in CO_2-saturated 5:1 v/v acetonitrile:triethanolamine solution illuminated for 20 h by a Xe lamp equipped with a UV long-pass filter and a UV-and-IR cutoff filter. Adapted with permission from ref 245. Copyright 2010 Wiley-VCH Verlag GmbH & Co.

8.2. Molecular-Catalyst-Modified Semiconductor Nanoparticles and Nanorods for CO_2 Reduction

Sato and co-workers reported on the reduction of CO_2 using a hybrid construct composed of p-type N-doped Ta_2O_5 (N-Ta_2O_5) functionalized with Lehn-type Ru electrocatalysts (Figure 32a).[245] Three different catalysts, each featuring a different ligand set, were compared in this work including $[Ru(dcbpy)(bpy)(CO)_2]^{2+}(PF_6^-)_2$, $[Ru(dcbpy)_2(CO)_2]^{2+}(Cl^-)_2$, and $[Ru(bpy)_2(CO)_2]^{2+}(Cl^-)_2$ (abbreviated as Ru-dcbpybpy, Ru-dcbpy, and Ru-bpy, respectively), where dcbpy stands for 4,4′-dicarboxy-2,2′-bipyridine and bpy stands for 2,2′-bipyridine. Ta_2O_5 powder with an orthorhombic crystalline structure (absorbing light with λ < 520 nm) was prepared and doped with nitrogen (8.9% weight, as calculated using XRD and PESA). Following doping, the N-Ta_2O_5 powder had p-type semiconductor characteristics, and the lowest energy absorption band was red-shifted by 200 nm. XRD indicated an average crystal size of 20 nm, and the E_{CB} minimum was determined to be −1.3 V vs NHE using PESA. The N-Ta_2O_5 powder was modified with Ru-dcbpybpy (N-Ta_2O_5|Ru-dcbpybpy) or Ru-dcbpy (N-Ta_2O_5|Ru-dcbpy), yielding Ru loadings of 0.8% weight for N-Ta_2O_5|Ru-dcbpybpy and 0.25% weight for N-Ta_2O_5|Ru-dcbpy. Solutions containing N-Ta_2O_5 powder and Ru-bpy were used as a control, as Ru-bpy does not contain the 4,4′-dicarboxy-2,2′-bipyridine functional group for anchoring to N-Ta_2O_5. Photochemical experiments were performed in 4 mL of a CO_2-saturated 5:1 v/v MeCN:TEOA solution containing either 5 mg of N-Ta_2O_5|Ru-dcbpybpy in suspension, 5 mg of N-Ta_2O_5|Ru-dcbpy in suspension, or 0.05 mM of Ru-bpy and 5 mg of N-Ta_2O_5 in suspension under illumination for 20 h using a Xe lamp equipped with a UV long-pass filter and UV-and-IR cutoff filter to produce light in the range 410−750 nm. All three constructs described in this report (N-Ta_2O_5|Ru-dcbpybpy, N-Ta_2O_5|Ru-dcbpy, and Ru-bpy with N-Ta_2O_5) were active for CO_2 reduction to HCOOH and removing the Ru-based catalyst, N-Ta_2O_5 semiconductor, or TEOA components resulted in zero or negligible product formation (Figure 32b). The N-Ta_2O_5|Ru-dcbpy assemblies achieved the highest rate of HCOOH generation as confirmed using IC TOF-MS, reaching a TON of 89 per metal complex for HCOOH after 8 h of operation, a value almost three times higher than that achieved using N-Ta_2O_5|Ru-dcbpybpy assemblies. Other products such as glycolic acid ($OHCH_2COO^-$), H_2, and CO were also detected (with the last two products being quantified using GC); however, the selectivity (defined as the ratio of moles of each product to the total moles of all products) for HCOOH was more than 75%. The amount of HCOOH produced increased linearly with the amount of semiconductor|catalyst assembly, with the highest rate of formation reaching 3.5 μmol h^{-1} when using 50 mg of the N-Ta_2O_5|Ru-dcbpy suspended in solution. Isotopic-labeling experiments conducted using nuclear magnetic resonance (NMR) spectroscopy and IC TOF-MS indicated the carbon source for HCOOH was indeed CO_2, which was not the case for other products such as CH_2OHCOO^- and bicarbonate (HCO_3^-). Likewise, the proton source required for formation of HCOOH was determined to be TEOA (which also served as the sacrificial electron donor in these systems). Quantum yields were determined using a Xe lamp equipped with either a 405, 436, or 480 nm band-pass filter and a 5 cm long $CuSO_4$ solution filter. The quantum yield of HCOOH generation was dependent on the optical absorption of the N-Ta_2O_5 semiconductor, achieving a maximum value of 1.9% at 405 nm.

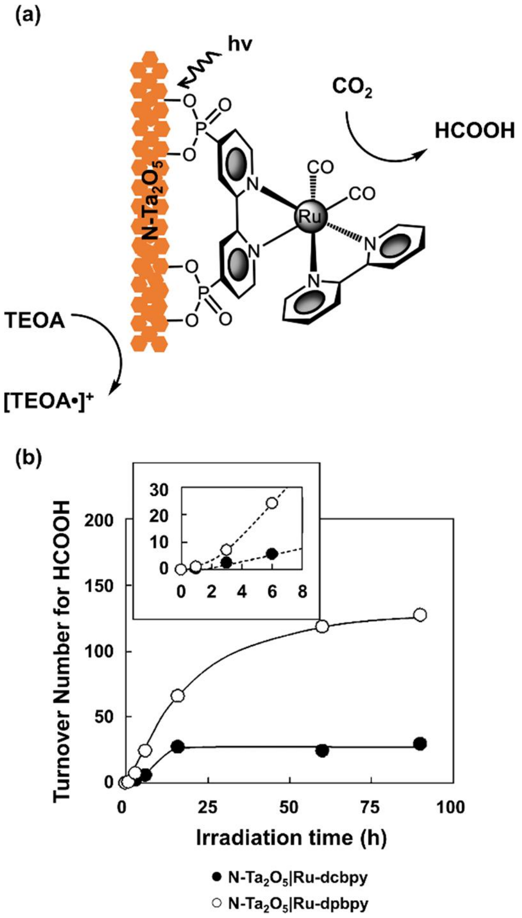

Figure 33. (a) Schematic representation of p-type N-doped Ta_2O_5 nanoparticle with a phosphonate-modified Lehn-type Ru-based catalyst. (b) Turnover number for HCOOH formation by N-Ta_2O_5|Ru-dcbpy (black circles) and N-Ta_2O_5|Ru-dpbpy (white circles) in CO_2-saturated 5:1 v/v acetonitrile:triethanolamine solution illuminated for 60 h by a Xe lamp equipped with a UV long-pass filter and a UV-and-IR cutoff filter. The inset shows the turnover number for HCOOH formation in the first 6 h. Adapted from ref 246. Copyright 2011 The Royal Society of Chemistry.

Suzuki and co-workers have also studied the effect of altering the surface-anchoring functional groups of the Lehn-type Ru catalysts. This included immobilizing Ru-based catalysts via surface-anchoring dcbpy groups as well as a 4,4′-diphosphate-2,2′-bipyridine (dpbpy) surface-anchoring groups onto N-Ta_2O_5 powder (Figure 33a).[246] The particle sizes of the N-Ta_2O_5 were determined to be 20−40 nm using SEM. A difference between this example and that described in the previous section is the N-Ta_2O_5 particles used in this subsequent work were functionalized in a two-step process, where a bidentate bipyridine ligand containing carboxylic acid or phosphonic acid anchoring groups (dcbpy or dpbpy) were initially deposited onto N-Ta_2O_5 and then the Ru-based catalysts were assembled via coordination of Ru to the pyridyl nitrogens of the immobilized ligands. Successful assembly of the Ru catalysts was confirmed using ATR-IR spectroscopy and TOF-SIMS, and surface loadings of 0.1% and 0.04% weight were determined for the N-Ta_2O_5|Ru-dcbpy and N-Ta_2O_5|Ru-dpbpy samples, respectively, via ICP analysis. As a control, the authors also prepared Ru-dcbpy-modified N-Ta_2O_5 in a single step by combining Ru-dcbpy and N-Ta_2O_5 in solution. To differentiate this construct from the related assembly formed via the two-step process, this construct is referred to as adsorbed N-Ta_2O_5|Ru-dcbpy. A surface loading of 0.07% weight was determined for adsorbed N-Ta_2O_5|Ru-dcbpy. Photochemical experiments were performed by suspending 10 mg of a Ru-catalyst-modified N-Ta_2O_5 sample in a CO_2-saturated organic solvent solution containing a sacrificial electron donor (5:1 MeCN:TEOA) at room temperature, and illuminating with a 500 W Xe lamp equipped with filters that produced light in the range 410−750 nm. In this report, four different constructs were investigated for CO_2 reduction. These constructs included (1) N-Ta_2O_5|Ru-dcbpy, (2) N-Ta_2O_5|Ru-dpbpy, (3) adsorbed N-Ta_2O_5|Ru-dcbpy, and (4) a mixture of nonsurface-adsorbed Ru-bpy and N-Ta_2O_5. For all constructs, following 60 h of illumination, the major product generated was HCOOH, as detected using GC and ion-exchange chromatography, and CO was also detected as another two-electron reduction product. However, control experiments conducted using N-Ta_2O_5 without Ru catalysts or Ru-bpy in solution without N-Ta_2O_5 did not result in detectable HCOOH generation. The TON associated with HCOOH production (defined in their work as the ratio of the concentration of HCOOH to the concentration of Ru after 60 h of photochemical operation) was 26 for the adsorbed N-Ta_2O_5|Ru-dcbpy construct, 19 for the mixture of nonsurface adsorbed Ru-bpy and N-Ta_2O_5, and 24 for the assembled N-Ta_2O_5|Ru-dcbpy, although the authors noted that the preparation of N-Ta_2O_5|Ru-dcbpy was "quicker and simple". Finally, the TON for HCOOH when using N-Ta_2O_5|Ru-dpbpy was 118, almost five times higher than the carboxylate-anchored Ru catalysts. The TON associated with HCOOH production was analyzed as a function of irradiation time for both N-Ta_2O_5|Ru-dcbpy and N-Ta_2O_5|Ru-dpbpy (Figure 33b). The former assembly no longer formed HCOOH after 16 h, while the N-Ta_2O_5|Ru-dpbpy assembly continued forming HCOOH after 60 h. During the first 6 h, N-Ta_2O_5|Ru-dpbpy also showed a faster rate of HCOOH formation in comparison to N-Ta_2O_5|Ru-dcbpy, indicating that anchoring with phosphonate groups enhances the overall reaction rate and reduces instability. To further investigate the enhanced performance of N-Ta_2O_5|Ru-dpbpy, electrochemical experiments were conducted using Ru-dcbpy or Ru-dpbpy immobilized onto TiO_2-coated (20 nm) FTO substrates (FTO|TiO_2|Ru-dcbpy or FTO|TiO_2|Ru-dpbpy, respectively). The Ru catalysts were immobilized using the previously

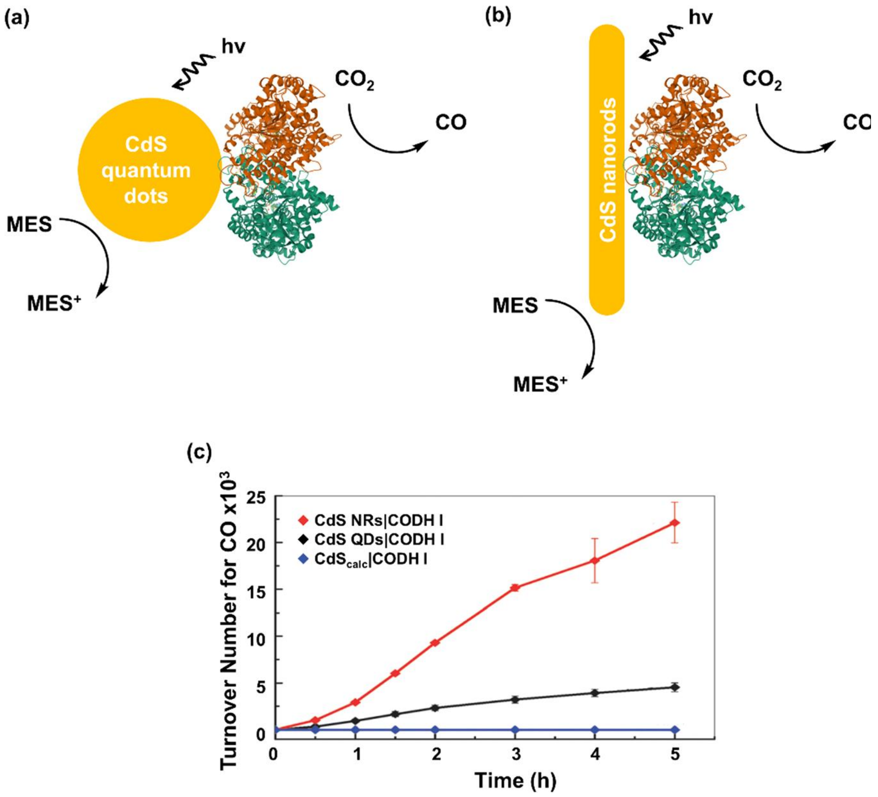

Figure 34. Schematic representation of a carbon monoxide dehydrogenase adsorbed on CdS (a) quantum dots and (b) nanorods. (c) Turnover number for CO formation by CdS NRs|CODH I (red), CdS QDs|CODH I (black), and CdS$_{calc}$|CODH I (where CdS$_{calc}$ represents CdS quantum dots calcinated at 450 °C for 45 min to obtain larger particle/clusters of irregular shape) (blue) in CO$_2$-saturated 0.35 M 2-(N-morpholino)ethanesulfonic acid solution under 23 mW cm^{-2} illumination for 5 h. Adapted from ref 247. Copyright 2012 The Royal Society of Chemistry.

described two-step assembly method, and their attachment was confirmed via ATR-IR spectroscopy. Cyclic voltammograms of the Ru catalyst-TiO$_2$-modified FTO electrodes were recorded in argon and CO$_2$-saturated MeCN solutions containing 0.1 M tetraethylammonium tetrafluoroborate as the supporting electrolyte. The authors reported the reduction potential values of FTO|TiO$_2$|Ru-dpbpy and FTO|TiO$_2$|Ru-dcbpy were ∼−1.35 V and −1.45 V vs I$_2$/I$_3^-$, respectively, and suggested the free energy difference between the E_{CB} minimum of N-Ta$_2$O$_5$ (−1.86 V vs I$_2$/I$_3^-$) and the Ru complex reduction potentials could be a determining factor of the electron-transfer rate from the semiconductor to the Ru complexes and may explain the enhanced CO$_2$ reduction activity observed when using Ru-dpbpy-based assemblies.

Armstrong and co-workers have reported biohybrid assemblies featuring [Ni4Fe-4S] carbon monoxide dehydrogenase (CODH I) enzymes that were isolated from *Carboxydothermus hydrogenoformans* and then adsorbed onto either CdS QDs or CdS NRs.[247] The E_{CB} of bulk CdS lies at −0.87 V vs SHE at pH 6, providing sufficient driving force to reduce CO$_2$ to CO (−0.46 V vs SHE at pH 6). TEM analysis indicated that the CdS QDs used in this work were mostly spherical in shape with an average particle size of 5.8 ± 1.8 nm. Conversely, the CdS NRs had average dimensions of 42 ± 10 nm in length and 10 ± 1 nm in width. The CODH I-modified QDs (CdS QDs|CODH I) (Figure 34a) and CODH I-modified NRs (CdS NRs|CODH I) (Figure 34b) were prepared via suspending 10 mg of the respective CdS nanocrystal powder in 5 mL of a 0.35 M MES buffer solution (pH 6) and then adding 13.9 μL of 184 μM CODH I (2.56 nmol) under an inert atmosphere. After 20 min of stirring, a supernatant was obtained by centrifugation followed by filtration. The amount of CODH I coattached with CdS QDs or CdS NRs was determined using UV−vis spectroscopy. In a typical sample, 10 mg of CdS QDs was coattached with 0.59 ± 0.032 nmol of CODH I, and 10 mg of CdS NRs was coattached with <0.1 nmol CODH I. Photochemical experiments were performed in the 0.35 M MES buffer solution (where MES served as sacrificial electron donor) at 20 °C, under an atmosphere of 98% CO$_2$/2% CH$_4$, with illumination over 5 h from a tungsten-halogen bulb equipped with a 420 nm long-pass filter (incident light intensity of 23 mW cm^{-2}). Product analysis was performed using GC, and CO was detected as the main product in experiments performed using either CdS QDs|CODH I or CdS NRs|CODH I. Despite the relatively higher loading of enzyme for the modified QD versus NR samples, the amount of CO produced during photochemical experiments performed using either of these hybrid materials (CdS QDs|CODH I or CdS NRs|CODH I) was nearly identical. These results indicate a nearly 5-fold difference in TOF of CODH I (with a calculated TOF per molecule of coattached enzyme of 0.25 s^{-1} for the CdS QDs|CODH I and a TOF of 1.23 s^{-1} for CdS NRs|CODH I) (Figure 34c), which the authors attribute to a curtailment of exciton recombination probability arising from the lower dimensionality of the NRs (40 nm in length and 10 nm width) over QDs (6 nm diameter).

Li and co-workers have reported TiO$_2$ NPs (P25, 80% anatase and 20% rutile) modified with [Co(cyclam)Cl$_2$]Cl catalyst (where cyclam is 1,4,8,11-tetraazacyclotetradecane).

The hybrid material (denoted as $TiO_2|Co^{III}(cyclam)X$, where X is Cl or OH) (Figure 35a) was prepared via refluxing the TiO_2 NPs and $[Co(cyclam)Cl_2]Cl$ in a mixture of MeCN with TEA under aerobic atmospheric conditions for 24 h to yield samples with a Co loading of 0.11 μmol mg^{-1}.[248] Control samples (to test the role of TiO_2 as the photosensitizer) of unimmobilized $Co^{III}(cyclam)X$ and $Silica|Co^{III}(cyclam)X$ (with a Co loading of 0.16 μmol mg^{-1}) were prepared via analogous synthetic methods performed in the absence of TiO_2 NPs and using silica in place of TiO_2 NPs, respectively. $TiO_2|Co^{III}(cyclam)X$ was also prepared via synthetic methods involving application of microwaves with heating at 80 °C for 2 h instead of refluxing for 24 h, yielding a Co loading of 0.06 μmol mg^{-1}. All materials were characterized via SEM and TEM, which indicated that $Co^{III}(cyclam)X$ formed a thin layer on the surface of TiO_2 NPs. In addition, NMR, FTIR, and XP spectroscopies as well as electrochemical measurements indicated that $Co^{III}(cyclam)X$ maintained a macrocyclic structure similar to $[Co(cyclam)Cl_2]Cl$, but XPS showed the presence of a Co-O bond in $Co^{III}(cyclam)X$, likely due to the majority of Cl ligands in the starting material being replaced with O-containing ligands (possibly OH) during the synthesis of $Co^{III}(cyclam)X$. Photochemical experiments were performed using 1 mg of $TiO_2|Co(cyclam)Cl_2]Cl$ dispersed in 4 mL of a CO_2-saturated 4:1:1 v/v MeCN:TEOA:MeOH solution (with TEOA as an electron donor), under illumination using a mercury lamp equipped with a water filter (100 mW cm^{-2}) for 4 h. CO and H_2 were determined via GC analysis to be the main photoproducts and were produced in near equimolar amounts. Furthermore, no significant production of HCOOH was detected via NMR analysis. Control experiments using either 1 mg of unmodified TiO_2 NPs, a mixture of 1 mg of $[Co(cyclam)Cl_2]Cl$ and 1 mg of TiO_2 NPs, or 1 mg of $Silica|Co^{III}(cyclam)X$, yielded no detectable CO after 4 h of light irradiation. Mixing 1 mg of $Co^{III}(cyclam)X$ with 1 mg of TiO_2 NPs yielded a TON (defined as the ratios between the amounts of CO produced and the amounts of Co present in reaction solutions) of 1.3 after 4 h of illumination. Alternatively, under otherwise identical conditions, using 1 mg of $TiO_2|Co^{III}(cyclam)X$ synthesized by the reflux method yielded a TON of 12.2 after 4 h of illumination, and using $TiO_2|Co^{III}(cyclam)X$ synthesized by the microwave method resulted in a TON of 19.7 after 4 h of illumination (Figure 35b). Diffuse reflectance FTIR spectroscopy was performed with $TiO_2|Co^{III}(cyclam)X$ in powder form (no solvent or TEOA), purged with Ar and then exposed to CO_2 prior to UV irradiation. After 150 min illumination, the formation of surface adsorbed carbonate species and CO adsorbed on Co^{3+} was observed, suggesting that CO_2 reduction might proceed via a formate-bridged dimer. Control experiments performed using TiO_2 NPs in place of $TiO_2|Co^{III}(cyclam)X$ yielded no significant formation of surface adsorbed CO, indicating $Co^{III}(cyclam)X$ was the active CO_2-reduction catalyst.

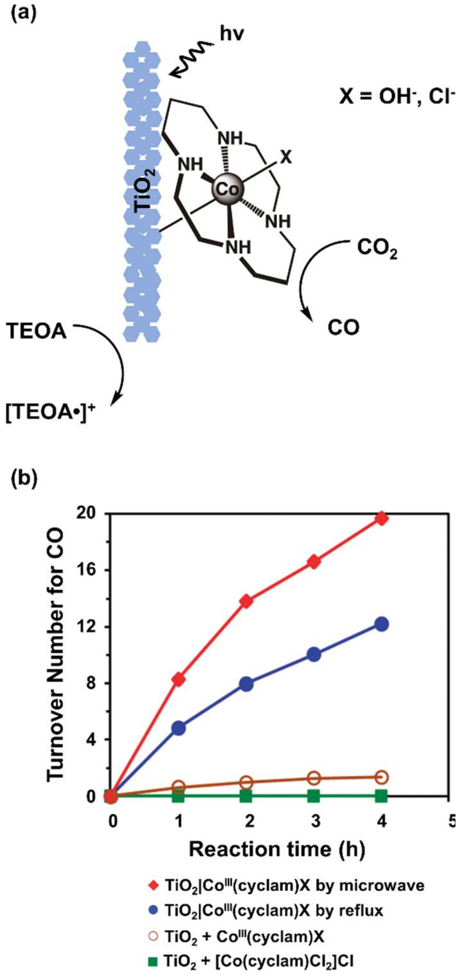

Figure 35. (a) Schematic representation of TiO_2 nanoparticles with an adsorbed cobalt-based cyclam catalyst. (b) Turnover number for CO formation by TiO_2 and $[Co(cyclam)Cl_2]Cl$ (green squares), TiO_2 and $Co^{III}(cyclam)X$ (brown circles), $TiO_2|Co^{III}(cyclam)X$ prepared by the reflux method (blue circles), and $TiO_2|Co^{III}(cyclam)$-X prepared by the microwave method (red diamonds) in CO_2-saturated 4:1:1 v/v acetonitrile:triethanolamine:methanol solution under 100 mW cm^{-2} illumination for 4 h. Adapted from ref 248. Copyright 2014 The Royal Society of Chemistry.

Maeda and co-workers developed a hybrid construct consisting of mesoporous-graphitic carbon nitride (mpg-C_3N_4) modified with Lehn-type Ru catalysts containing phosphonate anchoring groups, *cis,trans*-$[Ru\{4,4'-(CH_2PO_3H_2)_2-2,2'\text{-bipyridine}\}(CO)_2Cl_2]$, abbreviated here as RuCP (Figure 36a).[249] The pore size and specific surface area of the mpg-C_3N_4 as measured using adsorption–desorption experiments were 12 nm and 180 m^2 g^{-1}, respectively, and EIS was used to determine the semiconducting material had n-type character. Ru catalyst immobilization via phosphonic acid anchoring groups (forming mpg-C_3N_4|RuCP) was confirmed via FTIR spectroscopy, and the loading was determined to be 39.2 μmol RuCP g^{-1}. Photochemical CO_2 reduction experiments were conducted in a 4 mL CO_2-saturated 4:1 v/v MeCN:TEOA solution containing 8 mg of mpg-C_3N_4|RuCP in suspension under illumination for 5 h using a 450 W Hg lamp equipped with an aqueous $NaNO_2$ solution 400 nm long-pass filter. The main CO_2-reduction product detected using capillary electrophoresis was HCOOH. However, CO and H_2 were also detected using GC. Control experiments indicated that mpg-C_3N_4, RuCP, CO_2, and TEOA were all necessary to yield detectable amounts of reduced-carbon products. Isotope-labeling experiments conducted using GC–MS and ^{13}C NMR confirmed the carbon-containing products were derived primarily from CO_2 and not from the C_3N_4 semiconductor. Approximately 87% of the CO formed during these experiments was from gaseous CO_2, and the authors speculated the remaining 13% resulted

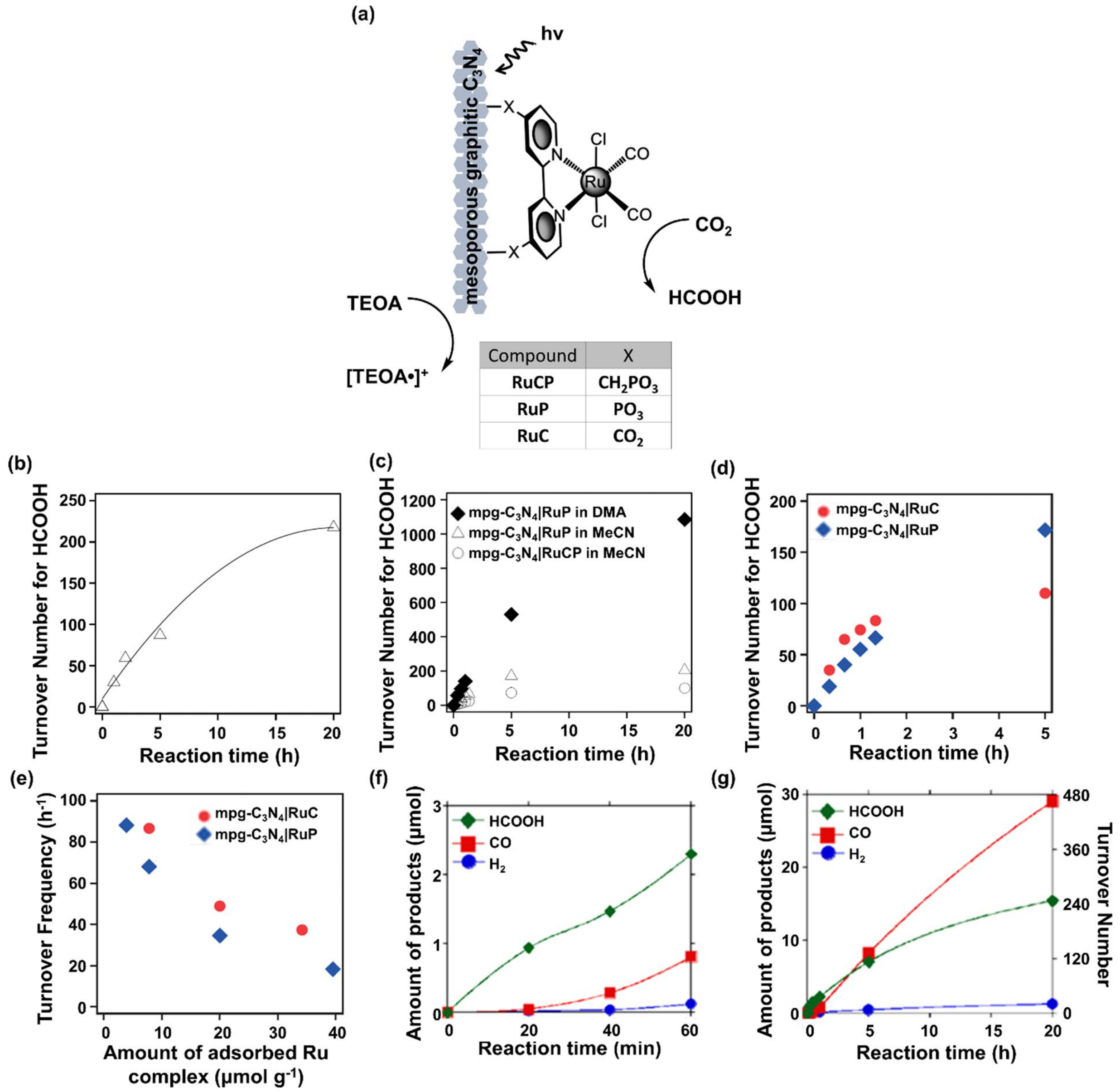

Compound	X
RuCP	CH_2PO_3
RuP	PO_3
RuC	CO_2

Figure 36. (a) Schematic representation of carbon nitride with phosphonate- or carboxylate-modified Lehn-type Ru-based catalyst. (b) Turnover number for HCOOH formation by mpg-C_3N_4|RuCP in CO_2-saturated 4:1 v/v acetonitrile:triethanolamine solution illuminated for 5 h with a 450 W Hg lamp equipped with a 400 nm long-pass filter. (c) Turnover number for HCOOH formation by mpg-C_3N_4|RuCP in CO_2-saturated 4:1 v/v acetonitrile:triethanolamine (white circles), mpg-C_3N_4|RuP in CO_2-saturated 4:1 v/v acetonitrile:triethanolamine (white triangles), and mpg-C_3N_4|RuP in CO_2-saturated 4:1 v/v dimethylacetamide:triethanolamine (dark diamonds) solution illuminated for 20 h with a 400 W Hg lamp equipped with a 400 nm long-pass filter. (d) Turnover number for HCOOH formation by mpg-C_3N_4|RuC (red circles) and mpg-C_3N_4|RuP (blue diamonds) in CO_2-saturated 4:1 v/v acetonitrile:triethanolamine solution illuminated for 5 h with a 400 W Hg lamp equipped with a 400 nm long-pass filter. (e) Turnover frequencies for HCOOH formation by mpg-C_3N_4|RuC (red circles) and mpg-C_3N_4|RuP (blue diamonds) at different complex loadings in CO_2-saturated 4:1 v/v acetonitrile:triethanolamine solution illuminated for 5 h with a 400 W Hg lamp equipped with a 400 nm long-pass filter. Amount of HCOOH (green diamonds), CO (red squares), and H_2 (blue circles) by mpg-C_3N_4|RuCP in CO_2-saturated 4:1 v/v dimethlylacetamide:triethanolamine solution illuminated with a 400 W Hg lamp equipped with a 400 nm long-pass filter for (f) 60 min and (g) 20 h. For (g), the calculated TON is included on the right-coordinate axis. (a, b) Adapted from ref 249. (c) Adapted with permission from ref 250. Copyright 2015 Wiley-VCH Verlag GmbH & Co. (d, e) Adapted with permission from ref 251. Copyright 2016 Chemical Society of Japan. (f, g) Adapted with permission from ref 252. Copyright 2016 American Chemical Society.

from degradation of the ligands associated with the Ru molecular catalyst, which was observed using FTIR spectroscopy. The amount of HCOOH produced was dependent on both irradiation time (ranging from 0 to 20 h) and amount of mpg-C_3N_4|RuCP used in these experiments (ranging from 1.6 to 80 mg), with the selectivity for HCOOH production ranging between 74 and 89% in these experiments. Following photochemical experiments conducted in a CO_2-saturated 4:1 v/v MeCN:TEOA solution containing 8 mg of the mpg-C_3N_4|RuCP under illumination for 20 h, the TON associated with HCOOH production was determined to exceed 200 (Figure 36b). However, UV−vis spectroscopy following photochemical operation indicated that some Ru catalysts desorbed from the C_3N_4 surface.

Further studies by Maeda and co-workers using mpg-C_3N_4 modified with Lehn-type Ru catalysts showed modification of the solvent and the catalyst's ligand structure can improve the TON by a factor of >5.[250] As an example, the methylphosphonic acid groups of the bipyridine ligand were replaced with phosphonic acid groups (yielding the catalyst abbreviated as RuP) (Figure 36a). Photochemical experiments using mpg-C_3N_4 modified with RuP (mpg-C_3N_4|RuP) in dispersion were performed in dimethylacetamide (DMA), instead of MeCN as used in previous studies of mpg-C_3N_4|RuCP, and illumination with a 400 W Hg lamp equipped with a 400 nm long-pass filter. In these studies, all other experimental conditions were kept the same as those used in their previously reported experiments using mpg-C_3N_4|RuCP. After 20 h, the per amount of RuP TON was ~1100 (Figure 36c), and the selectivity was 80% (67.7 μmol HCOOH, 17.7 μmol CO, and 0.9 μmol H_2). The apparent external quantum yield, as determined following 20 h of 400 nm illumination, was 5.7%.

Maeda and co-workers also compared the anchoring of RuP and its carboxylic-acid analog (RuC) onto mpg-C_3N_4 (Figure 36a).[251] Adsorption isotherms recorded using catalyst-modified samples of mpg-C_3N_4 with a surface area of 200 m^2 g^{-1} and average pore size 12 nm showed that RuC saturated at 30 μmol g^{-1} and RuP saturated at 40 μmol g^{-1}. Photochemical experiments using either mpg-C_3N_4|RuC or mpg-C_3N_4|RuP (catalyst loadings of 7.8 μmol g^{-1}) were conducted under similar conditions (8 mg suspended in 4 mL of CO_2-saturated 4:1 v/v MeCN:TEOA illuminated for 5 h using a 400 W Hg lamp with a 400 nm long-pass filter) and both constructs yielded HCOOH as the main product. During the first 2 h of illumination, RuC displayed a higher TON than RuP (~85 and ~60, respectively) (Figure 36d). Likewise, samples of mpg-C_3N_4|RuC (with catalyst loadings of 7.8, 20, and 35 μmol g^{-1}) yielded higher TOFs (~90, ~50, and ~40 h^{-1}, respectively) than those achieved using mpg-C_3N_4|RuP (with catalyst loadings of 5, 7.8, 20, and 40 μmol g^{-1} and TOFs of ~90, ~70, ~37.5, and ~20 h^{-1}, respectively) (Figure 36e). However, by the end of the 5 h illumination period, RuP had a TON higher than RuC (~170 and ~110, respectively), suggesting less degradation when using phosphonate linkers. Cyclic voltammograms recorded using catalyst-modified mpg-C_3N_4 in CO_2-saturated 4:1 v/v DMF:TEOA exhibited an enhanced current for mpg-C_3N_4|RuC compared to mpg-C_3N_4|RuP (~30 μA and ~20 μA at −1.65 V vs Ag/$AgNO_3$, respectively). However, the authors indicated that the origin of the enhancement was not clear. Lastly, the desorption of the complexes was quantified via UV−vis after stirring the constructs in 4:1 v/v MeCN:TEOA. After 20 min, 49% of the RuC had dissociated from the C_3N_4, and after 1 h 85% of the RuC had dissociated from the C_3N_4. In the case of RuP, only 37% and 68% of the complex had dissociated after 20 min and 1 h of stirring, respectively. These results again indicate that phosphonates bind more strongly than carboxylates. The amount of catalyst lost could contribute to the reduced performance after 5 h when using RuC versus RuP but could also indicate that RuC is a better catalyst for CO_2 reduction and perhaps explain the enhanced currents observed in the voltammetry experiments. The authors also suggested that, besides the desorption, there could be some still unknown light-induced degradation process(es).

In other work from Maeda and co-workers, mpg-C_3N_4 was modified with either RuCP, RuP, or RuC, and studied in either DMA or MeCN.[252] In a typical experiment, 8 mg of Ru-complex-modified mpg-C_3N_4 (with catalyst loadings of 7.8 μmol g^{-1}) was suspended in either 4 mL of 4:1 v/v DMA:TEOA or 4:1 v/v MeCN:TEOA before illumination for 20 h with a 400 W Hg lamp equipped with a 400 nm long-pass filter. In nearly all experiments performed under these conditions, HCOOH was the main product. However when RuCP was used as the catalytic component and DMA was the solvent, CO was produced with 64% selectivity and HCOOH with 34% selectivity. Experiments using DMA containing mpg-C_3N_4|RuCP with lower catalyst loadings (1.0 or 1.4 μmol g^{-1}) yielded HCOOH as the main product (52% HCOOH vs 24% CO and 67% HCOOH vs 17% CO for the two loadings, respectively). Alternatively experiments performed using DMA containing mpg-C_3N_4|RuCP with higher catalyst loadings (20.8 or 52.4 μmol g^{-1}) resulted in CO and HCOOH being generated in nearly equivalent amounts (53% CO vs 45% HCOOH for both loadings). Monitoring the photochemical products by GC when using mpg-C_3N_4|RuCP in DMA over 1 h of illumination indicated HCOOH was initially produced at a linear rate, while the production of CO displayed an induction period (Figure 36f). Nonetheless, both rates diminished over longer time scales, with the rate of HCOOH decreasing faster, and eventually leaving CO as the main product (Figure 36g). The authors concluded that catalytically active species for CO versus HCOOH production were different. Visual inspection of a sample with a relatively higher catalyst loading (4 mg of mpg-C_3N_4|RuCP with a catalyst loading of 81.4 μmol g^{-1} suspended in 4 mL of 4:1 v/v DMA:TEOA) before versus after the 20 h of illumination showed a change of color from yellow to black, and UV−vis diffuse reflectance spectroscopy (DRS) measurements confirmed increased absorbance in the 600−800 nm range. These changes in absorbance proved to be reversible after 24 h of exposure to air. Conversely, in related experiments, no pronounced changes in optical properties were observed when using mpg-C_3N_4|RuC or mpg-C_3N_4|RuP in place of mpg-C_3N_4|RuCP. The authors noted that the change in UV−vis diffuse reflectance spectral profile following illumination of mpg-C_3N_4|RuCP in DMA is consistent with the presence of a polymeric Ru species reported in literature as an active catalyst for CO formation during electrochemical CO_2 reduction. In addition to experiments performed using DMA, similar changes in the UV−vis diffuse reflectance spectral profile were observed when illuminating mpg-C_3N_4|RuCP in DMF or dimethyl sulfoxide (DMSO) but not when using THF, MeCN, or MeOH. The authors suggested that the intrinsic donor numbers of DMA, DMF, and DMSO, which are relatively higher than that of the other solvents, may have influenced these results. The authors also studied the effect of replacing TEOA (a relatively strong electron donor) with MeOH (a relatively weaker electron donor). When using 4 mL of a CO_2-saturated 4:1 v/v DMA:MeOH solution with 4 mg of mpg-C_3N_4|RuP (15.1 μmol g^{-1}) and 20 h of illumination, CO was the main product with a TON of 7.5. This result contrasted with those obtained using the same assembly in DMA containing TEOA as the sacrificial source of electrons, which produced mainly HCOOH with a TON of ~1100. The authors rationalized this difference in favoring production of CO over HCOOH when changing the sacrificial electron donor from TEOA to MeOH may be due to differences in the acidity of the solutions, given TEOA yields reaction conditions that are more basic (promoting $HCOO^-$), while using MeOH yields reaction conditions that are more acidic (promoting

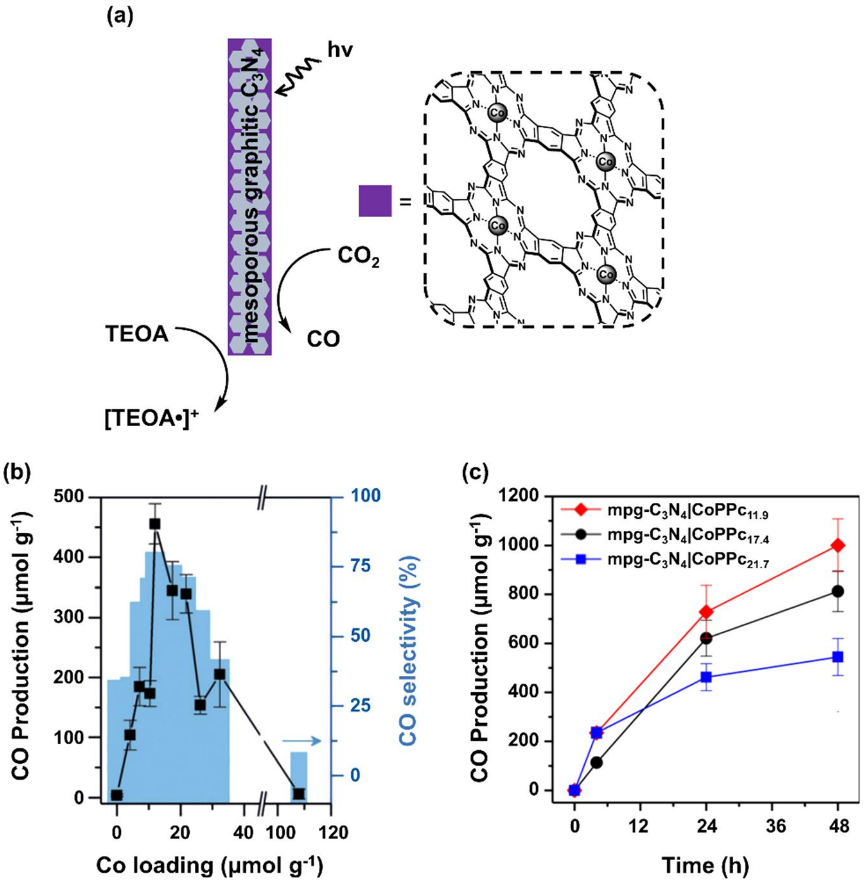

Figure 37. (a) Schematic representation of carbon nitride functionalized with a polymeric cobalt phthalocyanine. (b) Amount of CO produced (black squares) by mpg-C_3N_4|CoPPc using different Co loadings in CO_2-saturated 4:1 v/v acetonitrile:triethanolamine illuminated for 24 h at 100 mW cm^{-2} with an AM 1.5 G and a 400 nm long-pass filter. The calculated CO selectivity (blue bars) is included on the right-coordinate axis. (c) Amount of CO produced by mpg-C_3N_4|$CoPPc_{11.9}$ (red diamonds), mpg-C_3N_4|$CoPPc_{17.4}$ (black circles), and mpg-C_3N_4|$CoPPc_{21.7}$ (blue squares) in CO_2-saturated 4:1 v/v acetonitrile:triethanolamine illuminated for 48 h at 100 mW cm^{-2} with an AM 1.5 G and a 300 nm long-pass filter. Adapted with permission from ref 254. Copyright 2019 Wiley-VCH Verlag GmbH & Co.

CO).[253] The formation of a Ru polymer as a potential CO generator was also ruled out by measuring UV−vis DRS of 4.0 mg of mpg-C_3N_4|RuCP (28 µmol g^{-1}) in 4 mL of a 9:1 v/v DMA:MeOH solution before and after 20 h of illumination. These studies showed no rise in absorption in the 600−800 nm region, giving further credence that the acidity or basicity of the solution is what changed the product selectivity in these experiments. In addition, isotope labeling experiments confirmed (1) CO_2 as the carbon source of the CO, (2) the absence of HCOOH production, and (3) the formation of HCHO after the photochemical reaction. Given the change in free energy for the formation of HCHO, water, and CO from CO_2 and MeOH is $\Delta G° = +67.6$ kJ mol^{-1}, the authors concluded that the CO_2 reduction was achieved in a "non-sacrificial" manner (meaning the $\Delta G°$ of the overall reaction is >0).

Reisner and co-workers have reported photochemical reduction of CO_2 to CO using an organic−inorganic hybrid material in which mpg-C_3N_4 harvests solar energy and activates a surface-deposited polymeric Co phthalocyanine (CoPPc; PPc denotes polymeric phthalocyanine) catalyst. mpg-C_3N_4 was selected because it is nontoxic, easily synthesized, and able to absorb UV as well as visible light. Additionally, it has a E_{CB} of −1.10 V vs SHE at pH 6, allowing it to reduce the catalysts bound to its surface. The CoPPc was deposited onto mpg-C_3N_4 via an in situ polymerization method to form the hybrid material mpg-C_3N_4|CoPPc (Figure 37a).[254] To prepare the hybrid construct, 1,2,4,5-tetracyanobenzene, anhydrous $CoCl_2$, and 1,8-diazabicyclo[5.4.0]undec-7-ene (DBU) were added to a dispersion of mpg-C_3N_4 in 1-pentanol under inert atmosphere, and the dispersion was heated under microwave radiation at 180 °C for 2.5 h. The resulting mpg-C_3N_4|CoPPc was characterized using UV−vis DR, ATR-IR, Raman, and XP spectroscopies, and the photochemical activity was studied in CO_2-saturated MeCN under UV-filtered simulated solar light irradiation (100 mW cm^{-2}, equipped with an AM 1.5 G and a 400 nm long-pass filter) for 24 h, with TEOA as a sacrificial electron donor. Although bare mpg-C_3N_4 generated only trace amounts of H_2 and CO (determined using GC to analyze the headspace gas), mpg-C_3N_4|CoPPc exhibited considerably higher activity toward CO_2 reduction to CO. The photochemical activity of mpg-C_3N_4|CoPPc increased linearly with Co loading until ∼12 µmol Co per gram of mpg-C_3N_4|CoPPc. Further increase in Co content (>20 µmol Co g^{-1}) resulted in a decrease in activity and only a trace amount of CO was detected for the sample containing the highest loading of Co (107 µmol Co g^{-1}) (Figure 37b). At relatively high CoPPc concentrations (>107 µmol Co g^{-1}), the carbon nitride surface was "completely sheathed by the CoPPc layer", which could block the incoming light and reduce the accessibility of the mpg-C_3N_4 surface to TEOA. Longer-term experiments (96 h) showed that the selectivity toward CO decreased marginally

(80.3% ± 11.3 at 24 h compared to 72.5% ± 17.3 at 96 h). Under full solar spectrum irradiation (including wavelengths >300 nm), mpg-C_3N_4|$CoPPc_{11.9}$ (where 11.9 indicates the Co content of 11.9 μmol Co g^{-1} in the hybrid assemblies) generated 1000 μmol CO g^{-1} after 48 h (Figure 37c) with 85% selectivity (TON_{CO} = 84), which corresponds to a 65% increase in activity as compared to the activity of the same construct with irradiation of wavelengths >400 nm (607 μmol Co g^{-1} after 48 h, TON_{CO} = 51). EQE for CO formation by mpg-C_3N_4|$CoPPc_{11.9}$ was 0.11% under 360 nm illumination and 0.03% under 400 nm illumination.

Dukovic and co-workers utilized CdS NRs capped with MPA ligands to immobilize 2-oxoglutarate:ferredoxin oxidoreductase expressed from *Magnetococcus marinus* (MmOGOR) (Figure 38), which contains a [4Fe-4S] cluster.[255] The NRs had an average diameter of 22 nm, as measured using dynamic light scattering (DLS). Photochemical experiments were conducted using a 41 mM MES/4-(2-hydroxyethyl)-1-piperazineethanesulfonic acid (HEPES)/N-[tris(hydroxymethyl)methyl]-3-aminopropane-sulfonic acid (TAPS) pH 6.8 buffer solution containing 44 nM CdS, 100 nM MmOGOR, 7.8 mM CO_2 (delivered using 30 mM $NaHCO_3$), 200 μM succinyl-coenzyme A (SCoA), 7 mM 2-mercaptoethanol, 625 μM tetraphenyl-phosphonium, 500 μM $MgCl_2$, 10 mM NH_4Cl, 1.7 μM glutamate dehydrogenase (GDH), and 252 μM nicotinamide adenine dinucleotide (NADH) under 32 mW illumination with a CW 405 nm diode laser for 3 h. Following the illumination period, analysis of the samples using quadrupole TOF-MS coupled to electron-spray ionization (ESI) confirmed the presence of 2-oxoglutarate, indicating a C−C bond was formed by coupling of CO_2 and SCoA. Product formation was qualitatively confirmed using high-resolution mass spectrometry. Further, an optical-based, quantitative assay, where a second enzyme, GDH, consumes NADH (maximum absorbance at 340 nm) during the amination of 2-oxoglutarate to form glutamate, was used to establish the dependence of the reaction rates on the concentrations of SCoA, CO_2, or excitation frequency. The authors found that CO_2 did not bind as strongly as SCoA to MmOGOR and the internal quantum yield of product formation was relatively low (∼1%), meaning only 1% of photoexcited electrons were used for 2-oxoglutarate formation. Using ultrafast transient absorption spectroscopy and DLS studies, electron transfer from the CdS NRs to the immobilized MmOGOR was found to be strongly dependent on whether the SCoA was bound to the MmOGOR active site. Crystal structures of MmOGOR and MmOGOR-SCoA showed that following binding of SCoA, the enzyme underwent a conformational change at a domain presumed to be the site binding to CdS. Therefore, conformational changes in MmOGOR upon SCoA binding could impact the strength of the NR-enzyme interactions and ultimately the electron-transfer pathway. This work highlights the importance of structural considerations in the design of systems where enzymes are used.

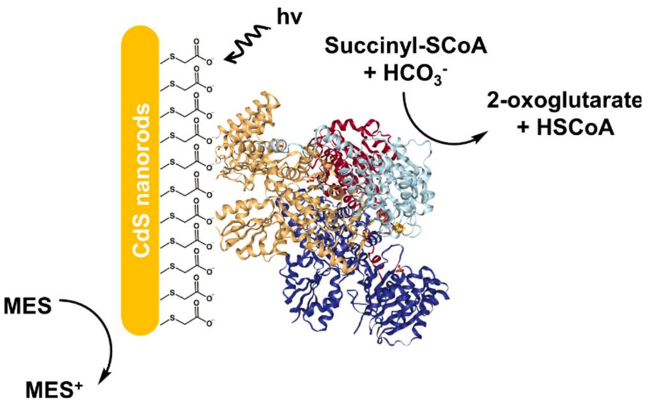

Figure 38. Schematic representation of MPA capped CdS nanorods containing a surface-immobilized 2-oxoglutarate:ferredoxin oxidoreductase. Adapted with permission from ref 255. Copyright 2020 National Academy of Sciences.

Robert and co-workers have described hybrid constructs featuring a molecular Co complex attached to mpg-C_3N_4. mpg-C_3N_4 was used as an earth-abundant visible-light photocatalyst, with relatively high chemical stability, and electron-withdrawing properties. These materials were prepared by adding mpg-C_3N_4 (with a pore volume of 0.50 cm^3 g^{-1} and a specific surface area of 111 m^2 g^{-1}), 1-ethyl-2-(3-dimethylaminopropyl)carbodiimide, and TEA to a suspension of DMF containing a Co quaterpyridine (Coqpy) complex

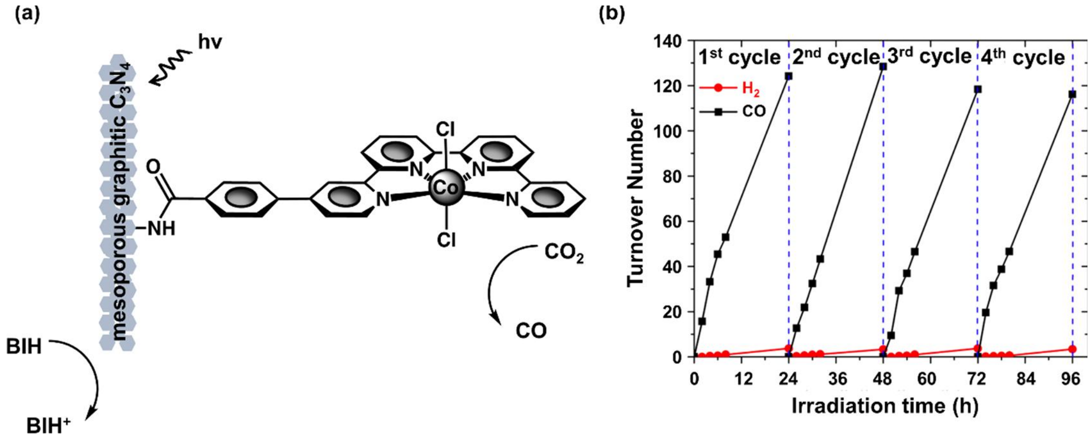

Figure 39. (a) Schematic representation of a cobalt quaterpyridine complex covalently linked to graphitic carbon nitride. (b) Turnover number for the formation of H_2 (red circles) and CO (black squares) by mpg-C_3N_4|Coqpy in CO_2-saturated 0.05 M BIH and 0.03 M phenol in acetonitrile solutions illuminated for four consecutive cycles of 24 h with a 100 W Xe lamp equipped with an AM 1.5 G and a 400 nm long-pass filter. Adapted with permission from ref 256. Copyright 2020 American Chemical Society.

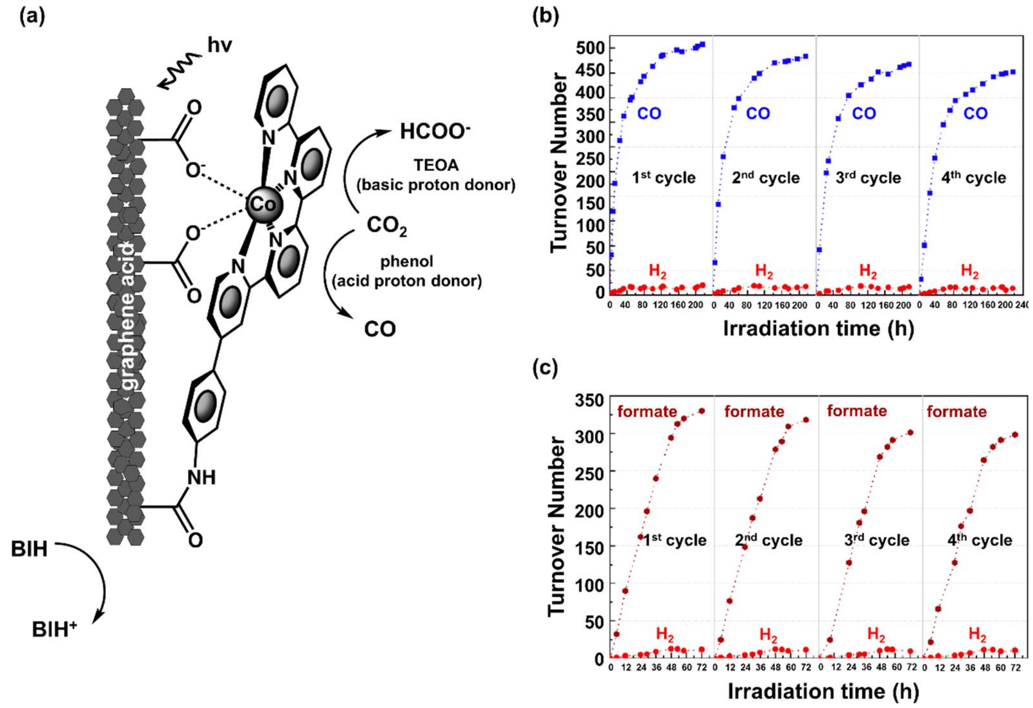

Figure 40. (a) Schematic representation of a cobalt quaterpyridine complex covalently linked to graphene acid. (b) Turnover number for the formation of H_2 (red circles) and CO (blue squares) by GA|Coqpy in CO_2-saturated 0.1 M phenol in acetonitrile solutions illuminated for four consecutive cycles of 216 h each with a 100 W Xe lamp equipped with an AM 1.5 G and a 400 nm long-pass filter. (c) Turnover number for the formation of H_2 (red circles) and $HCOO^-$ (dark red circles) by GA|Coqpy in CO_2-saturated 1.51 M triethanolamine in acetonitrile solutions illuminated for four consecutive cycles of 72 h each with a 100 W Xe lamp equipped with an AM 1.5 G and a 400 nm long-pass filter. Adapted with permission from ref 258. Copyright 2021 American Chemical Society.

functionalized with a carboxylic acid group (Coqpy-Ph-COOH). The grafting of Coqpy-Ph-COOH is reported to occur via an amide linkage to form mpg-C_3N_4|Coqpy (Figure 39a).[256] The samples were characterized via FTIR and XP spectroscopies, and the amount of Co on the surface was determined using ICP-OES to be 0.00876% weight (equivalent to 1.48 μmol g^{-1}). When using nanosheets of graphitic carbon nitride (nsg-C_3N_4) in place of the mpg-C_3N_4, the otherwise identically prepared construct, nsg-C_3N_4|Coqpy, had a higher Co loading of 0.02670% weight (equivalent to 4.53 μmol g^{-1}). Cyclic voltammograms recorded using the homogeneous Coqpy-Ph-COOH complex in DMF, in the presence of CO_2 and 0.1 M phenol as a source of protons, showed the presence of catalytic redox feature with an increasing J, from ~7.5 μA at ~−1.2 V vs SCE to a maximum of ~70 μA at ~−1.6 V vs SCE. Given the mpg-C_3N_4 $E_{CB} \approx -1.35$ V vs SCE,[257] the authors concluded that light excitation of the semiconducting material resulted in reduction of the cobalt-based molecular catalysts. EIS experiments also showed that, among (1) mpg-C_3N_4|Coqpy, (2) mpg-C_3N_4, and (3) mpg-C_3N_4 mixed with Coqpy, the mpg-C_3N_4|Coqpy electrodes yielded the lowest charge-transfer resistance. Photochemical experiments using a sacrificial source of electrons were carried out in CO_2-saturated MeCN, in the presence of 0.05 M 1,3-dimethyl-2-phenyl-2,3-dihydro-1H-benzo[d]imidazole (BIH) as the sacrificial electron donor, 0.03 M phenol as source of protons, and 6 mg of mpg-C_3N_4|Coqpy catalysts (equivalent to ~3 mM Coqpy). After 24 h of illumination using an AM 1.5 G simulator equipped with a 100 W Xe lamp and a 400 nm long-pass filter, the system produced CO from CO_2 (as confirmed via isotope-labeling experiments) with a 98% selectivity and a TON of 128 (or 8 μmol g^{-1} h^{-1}). Analogous experiments using a mixture containing mpg-C_3N_4 and Coqpy-Ph-COOH, or using Coqpy-Ph-COOH adsorbed overnight onto mpg-C_3N_4 (but without the reagents required for forming the amide linkages), resulted in a diminished amount of CO (four and eight times less, respectively), showing that the covalent grafting of Coqpy enhances catalysis. Furthermore, longer-term experiments of 96 h showed that the selectivity was maintained at a value of 97%, reaching a TON of 254. In a recycling experiment, mpg-C_3N_4-Coqpy was used for 24 h, then washed with MeCN, sonicated, centrifuged, dried, and immediately reused in another 24 h cycle with a fresh CO_2-saturated MeCN solution with BIH and phenol. After four consecutive cycles, the catalyst maintained a TON of ~120 on each cycle (TON = 486 in total over 96 h of irradiation) (Figure 39b), and an apparent external quantum yield at 440 nm for CO formation of 0.25%. XRD and UV−vis spectra of mpg-C_3N_4-Coqpy after irradiation showed no evidence of material instability or decomposition. Photoelectrochemical experiments were performed by depositing mpg-C_3N_4|Coqpy onto FTO electrodes that were used as working electrodes in a three-electrode cell configuration, with a Pt counter electrode and a standard calomel reference electrode all suspended in a 0.1 M Na_2SO_4 solution "without any bias". The transient J produced using a 300 W Xe lamp was 3 mA cm^{-2} and was stable over 6 min (10 cycles of 20 s of illumination and 20 s of nonillumination). Control samples consisting of mpg-C_3N_4 dispersed in MeCN mixed with Coqpy-Ph-COOH and mpg-C_3N_4 showed negligible currents.

Robert and co-workers have also reported studies using Coqpy covalently bonded to graphene acid (GA) for photochemical reduction of CO_2 to CO in acidic conditions, and to $HCOO^-$ in basic conditions.[258] GA was chosen over other carbon-based nanomaterials, such as graphene or graphene oxide, since it offers a more precise control of the surface groups due to the presence of −COOH moieties on its surface. Additionally, it offers a high electronic conductivity, a high surface area, and a relatively simple methodology for synthetic manipulation of the surface chemistry. In their work, Coqpy was immobilized by adding its amino-functionalized analog to a suspension of GA in DMF, hydroxybenzotriazole, TEA, and dicyclohexylcarbodiimide to yield the hybrid construct GA|Coqpy (Figure 40a). The immobilization of the catalyst was confirmed using Raman spectroscopy, FTIR spectroscopy, XPS, XAS, XANES, high-resolution TEM, EDX, and UV−vis DRS, with a loading of 5.5% weight calculated from XPS. In addition to the presence of amide bond linkages on the surface, data from XPS, XANES, and EDX indicated the loss of the two axial Cl ligands of the Coqpy complex, whereas the XANES results indicated an additional Co−O interaction attributed to the coordination of carboxylic acid groups on the GA surface to the Co atom to fulfill charge accountability with the Co^{II} oxidation state. Photochemical experiments were carried out by suspending 0.02 mg (∼15 μM) of GA|Coqpy in 6 mL of CO_2-saturated MeCN with 0.05 M BIH as sacrificial electron donor and 0.1 M phenol as a proton source. In these studies, the samples were illuminated with an AM 1.5 G solar simulator equipped with a Xe lamp and a 400 nm optical long-pass filter. After 222 h of illumination, 7.06 μmol of CO was detected using GC, corresponding to a TON (relative to the amount of Coqpy) of 513 and a selectivity (molar fraction of the product) of 97%, with H_2 being the only byproduct. Isotope labeling experiments confirmed that CO was formed from CO_2. Throughout the course of the 222 h experiment, the amount of CO detected did not reach a plateau (indicating the system remains active), while the amount of H_2 produced remained relatively low (TON < 25). Control experiments using GA mixed with Coqpy in place of GA|Coqpy, GA mixed with $CoCl_2$ in place of GA|Coqpy, Ar in place of CO_2, or with no illumination, resulted in negligible amounts of CO (TONs from 0 to 13). In addition, changing the proton source from phenol to TEOA (a weak base) resulted in $HCOO^-$ as the main product (TON = 330 and selectivity = 99% with H_2 as the secondary product) following 45 h of illumination. After 222 h of illumination and under acidic conditions (using phenol as a proton source in place of TEOA), the apparent external quantum yield was determined to be 0.57%, while after 45 h of illumination under basic conditions (TEOA as a proton source in place of phenol) the apparent external quantum yield was determined to be 0.85%. Following four successive cycles of 216 h of illumination performed using phenol as a proton source, where the GA|Coqpy material was filtered and washed between cycles, the TON was reduced by ∼10% (from a TON = 513 at the end of the first cycle to a TON = 450 at the end of the fourth cycle). This equates to an overall TON = 1900 over 860 h (Figure 40b). In the equivalent experiment using TEOA in place of phenol, after four successive cycles of 72 h of illumination each with filtrations and washing in-between cycles, TON also decreased by ∼10% (from a TON = 330 at the end of the first cycle, to a TON = 300 at the end of the fourth cycle with an overall TON = 1300 almost 290 h of irradiation) (Figure 40c). The authors mentioned that the loss in activity could be due to loss of catalyst during the filtering and washing procedures. Further, XPS analysis after the cycling study indicated a reduction of Co metal center during the catalysis, where the amount of reduced Co species present in the hybrid assembly after the reaction was 15.3% when studied under basic conditions and 9.2% under acidic conditions.

Bian and co-workers used a Mn bipyridyl complex (MnP) bearing phosphonic acid anchoring groups for attachment to graphitic carbon nitride (g-C_3N_4) semiconductor surfaces for generating the hybrid material, g-C_3N_4|MnP (Figure 41).[259]

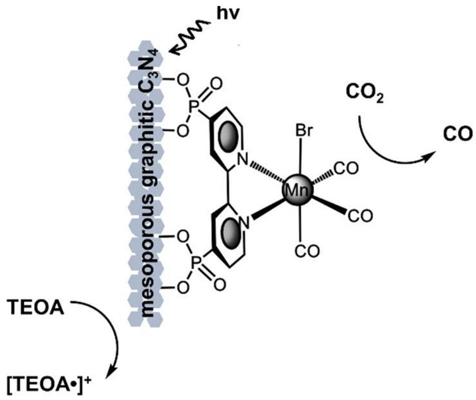

Figure 41. Schematic representation of carbon nitride with phosphonate-modified Lehn-type Mn-based catalyst. Adapted with permission from ref 259. Copyright 2020 Elsevier.

XRD, NMR spectroscopy, and ESI-MS gave evidence of successful preparation of these MnP macromolecular organic complexes. SEM images of g-C_3N_4 and g-C_3N_4|MnP (with a g-C_3N_4|MnP mass ratio of 100:1) demonstrated the pure g-C_3N_4 sample was layered, meaning different layers were stacked together to form a multilayer structure with a smooth surface. After alkali treatment, MnP complexes were loaded onto the surfaces of g-C_3N_4 sheets, and SEM images indicated no changes in the morphology of the g-C_3N_4 after attaching the MnP catalysts. Electrochemical measurement confirmed that catalytic CO_2 reduction processes were only observed in g-C_3N_4 following MnP attachment. Photochemical experiments were conducted using a dispersion containing 10 mg of g-C_3N_4|MnP, a total reaction solvent volume of 30 mL, and illumination from a 500 W Xe arc lamp for 0, 2, 4, 6, and 8 h. Product analysis using GC and ion chromatography confirmed CO as the only product of CO_2 reduction using g-C_3N_4|MnP, and no MeOH was detected. The TON for CO was determined using (1) different mass ratios of g-C_3N_4|MnP (200:1, 100:1, or 50:1), (2) different reaction solvents (H_2O, DMF, or MeCN), (3) different volumes of TEOA as sacrificial electron donor (1, 2, 4, 6, or 8 mL), and (4) different amounts of deionized water (1, 2, or 3 mL). In these studies, the highest TON for CO (102 after 8 h) was achieved using a g-C_3N_4|MnP mass ratio of 100:1, H_2O as reaction solvent, and 6 mL of TEOA as an additive.

Bai and co-workers have reported on photochemical CO_2 reduction using Co porphyrins anchored onto graphitic carbon nitride (Figure 42a).[260] Metalloporphyrins bearing diaminotriazinylphenyl groups (abbreviated as MTDPP, where M is either Fe, Ni, or Co) or a freebase analog (abbreviated as TDPP) were polymerized with urea at elevated temperatures, 390 to 550 °C ramped over a 2 h period, to yield nanosheets of the composite materials (abbreviated as g-CNU|MTDPP for samples featuring metalloporphyrins and g-CNU|TDPP for those featuring a freebase porphyrin) where the molecular catalysts were covalently linked to g-CNU. The resulting

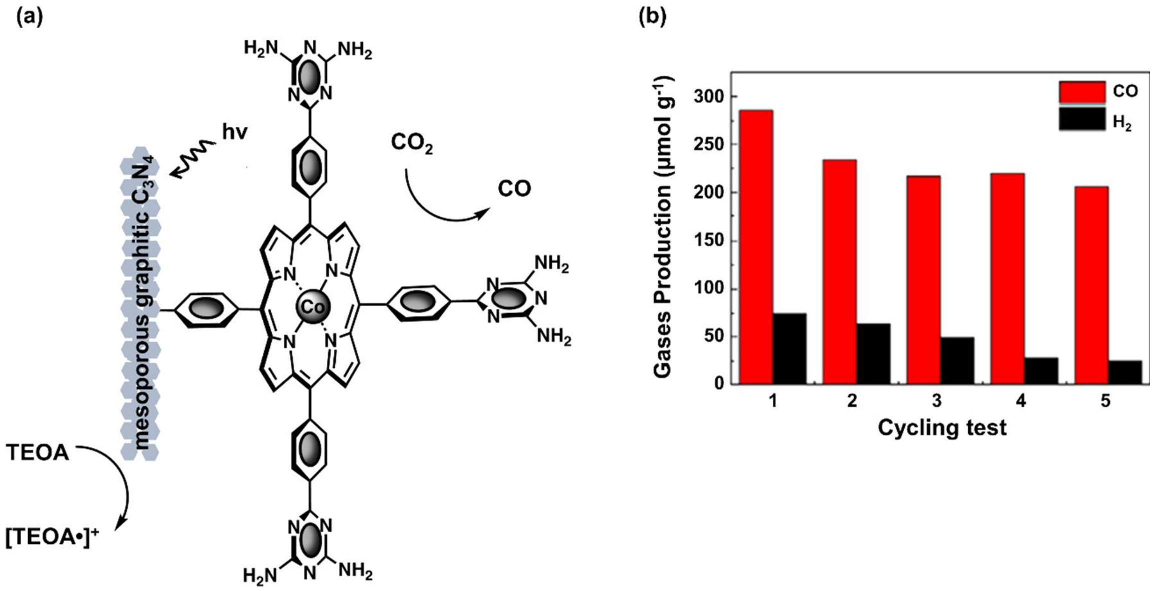

Figure 42. (a) Schematic representation of a cobalt porphyrin linked to graphitic carbon nitride. (b) Production rate for the formation of CO (red) and H_2 (black) by g-CNU|CoTDPP in CO_2-saturated 4:1 v/v acetonitrile:triethanolamine solutions illuminated for five consecutive cycles of 5 h each with a 5 W LED lamp equipped with a 400 nm long-pass filter. Adapted from ref 260.

samples were structurally characterized using FTIR spectroscopy, UV−vis absorption spectroscopy, XPS, XRD, TEM, AFM, and high-angle annular dark-field STEM. Photocurrent measurements were performed using a g-CNU|CoTDPP-modified ITO working electrode wired to a Pt counter electrode and a saturated Ag/AgCl reference electrode. The working electrode was prepared via a dip-coating method where the ITO slide was immersed in a solution containing 1 mg of g-CNU|CoTDPP dissolved in 1 mL of ethanol and 10 μL of Nafion and then air-dried. Under V_b = 0 V with illumination from a 300 W Xe visible light source equipped with a 400 nm long-pass filter, J of ∼1.00 μA cm^{-2}, and ∼0.61 μA cm^{-2} were recorded using g-CNU|CoTDPP-modified ITO and unmodified ITO working electrodes, respectively. Photochemical experiments were performed using a suspension of the nanosheets in MeCN with TEOA as the electron donor under 75 mW cm^{-2} illumination from a 5 W LED lamp equipped with a 400 nm long-pass filter. During these experiments, the CO production rates were determined via analysis of the headspace gas using GC−MS. Following 5 h of illumination, g-CNU|CoTDPP yielded the highest CO production (over 200 μmol g^{-1}), whereas negligible CO (<25 μmol g^{-1}) was produced when using g-CNU, g-CNU|TDPP, g-CNU|FeTDPP, or g-CNU|NiTDPP, demonstrating that Co is indispensable for the photochemical reduction of CO_2. The CO production was also evaluated (under conditions previously stated) for samples of CoTDPP coupled to g-CNU but annealed at different temperatures. When annealed at room temperature, g-CNU|CoTDPP exhibited a CO evolution rate of 30 μmol g^{-1} over 5 h (with selectivity of 83% for CO over H_2). When annealed at 80 °C, the CO evolution rate doubled to 63 μmol g^{-1} over 5 h. Finally, when annealed at 550 °C, the CO evolution rate reached approximately 300 μmol g^{-1} over 5 h, yielding a TOF of 7.1 h^{-1} (0.002 s^{-1}) for CO evolution. Longer-term experiments of 30 h showed a nearly linear growth of the CO production with an average production rate of 31 μmol g^{-1} h^{-1}. In a recycling experiment, g-CNU|CoTDPP was used for five consecutive cycles of 5 h each, the catalyst maintained 76% of their original performance (Figure 42b). The authors concluded that the photochemical CO_2 reduction activity of g-CNU|CoTDPP could be attributed to the following: (1) the enlarged specific surface area of g-CNU|CoTDPP provided more exposed catalytic sites; (2) the incorporation of porphyrins into the framework of g-CNU|CoTDPP extended the visible-light absorption range; (3) the reduced thickness of the nanosheets facilitated the electron-transfer to the surface of the catalysts, preventing charge carrier recombination; and (4) the covalent bonding between CoTDPP and g-CNU accelerated the electron transfer from g-CNU to CoTDPP.

Jing and co-workers investigated the reduction of CO_2 to CO and CH_4 using metallophthalocyanines (abbreviated as MPc, where M = Cu, Fe, or Co) immobilized onto HNO_3-treated graphitic carbon nitride (T-CN) nanosheets via hydrogen bonding to form the heterogeneous assemblies T-CN|MPc (Figure 43a).[261] The study focused primarily on the T-CN|CuPc because this construct was found to have the strongest theoretical adsorption energy (−1.44 eV) for CO_2 compared to the other metal-centered constructs (−0.25, and −0.1 eV for CoPc, and FePc respectively). These theoretical results were consistent with CO_2 temperature-programmed desorption experiments showed CuPc also displayed the strongest signal of the samples studied. DR spectra recorded using T-CN|CuPc showed absorption features characteristic of CuPc. In addition, Raman spectra of T-CN|CuPc showed a band centered at 1528 cm^{-1} assigned to the stretching of C-N-C bond in CuPc, suggesting "a strong chemical interaction" of T-CN with the Pc ligand due to hydrogen bonding. Further evidence consistent with attachment of the CuPc to T-CN through hydrogen bonding was provided via FTIR analysis, where spectra recorded using T-CN|CuPc showed a weakening of the hydroxyl signal intensity as compared to those recorded using unmodified T-CN. CO evolution rates, determined via GC−MS analysis of the headspace gas, were recorded using 0.1 g of powdered T-CN|MPc dispersed in 5 mL of water in a 100 mL steel reactor, followed by bubbling with pure CO_2, 20 min

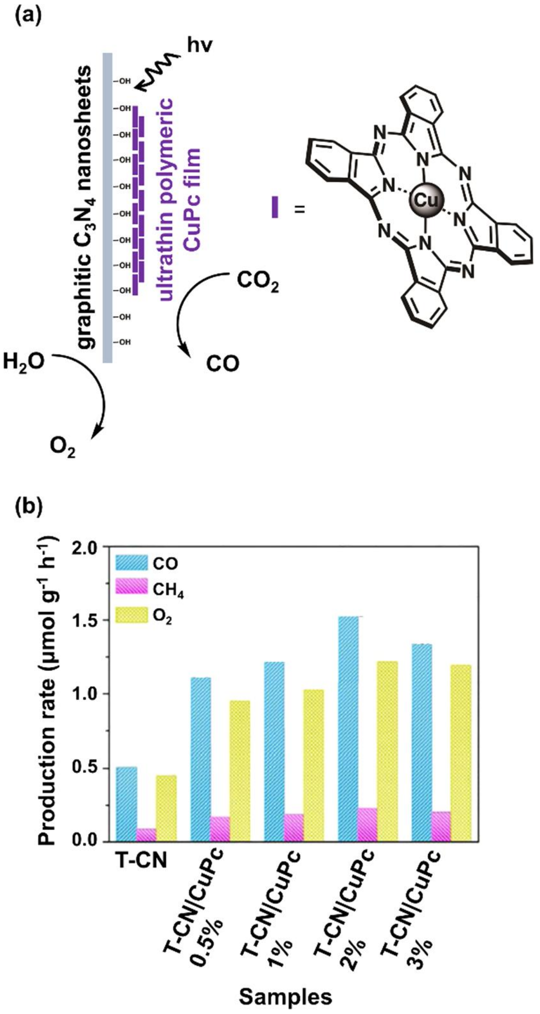

Figure 43. (a) Schematic representation of carbon nitride nanosheets with ultrathin copper phthalocyanine films. (b) Production rate for the formation of CO (light blue), CH_4 (pink), and O_2 (yellow) by T-CN|CuPc with different % weight loadings of CuPc in CO_2-saturated aqueous solutions illuminated for 4 h with a 300 W Xe lamp equipped with a 420 nm long-pass filter. Adapted with permission from ref 261. Copyright 2020 Elsevier.

of equilibration, and then 4 h of irradiation using a 300 W Xe arc lamp with a long-pass filter ($\lambda \geq 420$ nm). Under these conditions, the CO production rates by T-CN|CuPc, T-CN|CoPc, T-CN|FePc, and bare T-CN were found to be approximately 6.0, 5.7, 5.0, and 1.7 μmol g^{-1}, respectively. The highest photochemical activity was observed using T-CN|CuPc (over Co and Fe analogs) and was attributed to the suitable energy band position of CuPc with T-CN, which enabled the relatively high-level energy electron transfer from T-CN to CuPc, strong CO_2 binding, and weak CO binding on the metal center of CuPc. Steady-state surface photovoltage spectroscopy (SS-SPS) was used to investigate the generation, separation, and recombination of photogenerated charge carriers through observing changes in the surface potential of the T-CN|CuPc upon exposure to light. In these experiments, two peaks in V_{ph} were observed. A peak between 300 and 450 nm was attributed to charge separation occurring in the T-CN, and the weaker peak between 600 and 800 nm was assigned to sensitization of the MPc. To assess the effect of catalyst loading on V_{ph}, SS-SPS spectra were collected using different loadings of CuPc onto the T-CN (0, 0.5, 1, 2, and 3% weight CuPc). These results indicated that a 2% weight loading of CuPc generated the highest V_{ph} among the loadings studied. In addition, time-resolved surface photovoltage (TR-SPV) spectra were recorded using samples of T-CN|CuPc with a 2% weight loading of CuPc under an N_2 atmosphere and 355 nm laser pulse from a neodymium-doped yttrium aluminum garnet nanosecond laser. A TR-SPV response of approximately 0.27 mV was observed for T-CN|CuPc with a prolonged photogenerated charge lifetime as compared to unmodified T-CN, indicating an electron-transfer from T-CN to CuPc. The relationship between % weight loading of CuPc and product generation was also investigated using different loadings of CuPc onto the T-CN (0, 0.5, 1, 2, and 3% weight CuPc). Of the loadings studied, a 2% weight CuPc showed the fastest CO, CH_4, and O_2 evolution (at rates of up to 1.50, 0.23, and 1.22 μmol g^{-1} h^{-1}, respectively). Increasing the CuPc loading to 3% weight resulted in a decline in the CO production rate to approximately 1.28 μmol g^{-1} h^{-1}, and CH_4 and O_2 production remained approximately the same as that observed using a 2% weight loading (Figure 43b). Using T-CN|CuPc samples with a 2% weight loading, the apparent external quantum yield of CO_2 reduction to CO and CH_4 was ~0.7% overall when measured under 405 nm monochromatic light irradiation, and ~0.2% when measured under 660 nm monochromatic light.

Wang and co-workers prepared metallotetrakis(4-carboxyphenyl)porphyrins (containing Cu, Co, or Ni) adsorbed onto commercial titania (P25) to form the hybrid material TiO_2|MTCPP (Figure 44a).[262] Evidence of successful porphyrin coordination was provided via FTIR, UV−vis DR, and XP spectroscopies as well as SEM and TEM. These measurements also indicated almost no change in morphology and particle size of the P25 following the surface-modification chemistry. Photochemical experiments were performed in a vacuum reaction system under a 70 kPa atmosphere of CO_2, using 50 mg of TiO_2|MTCPP dispersed onto a porous quartzose slice, and deionized water as a sacrificial agent. The constructs were illuminated with a Xe lamp at 83.5 mW cm^{-2} equipped with a short-pass water filter and the photoproducts were mainly CO and a relatively small amount of CH_4. Control experiments showed that neither of these products were detected when replacing CO_2 with Ar, or when using a 420 nm short-pass filter. By varying the loading of CuTCPP onto TiO_2 from 1.0 to 15.0% weight, it was found that a 5% by total weight loading yielded the highest activity of 13.6 μmol g^{-1} h^{-1} for CO and 1.0 μmol g^{-1} h^{-1} for CH_4. On the basis of their findings, the authors concluded that relatively high loadings of TCPP likely screened the underlying TiO_2 from illumination. The authors also compared the rates of product formation recorded using samples TiO_2|CuTCPP to those measured using samples of TiO_2 modified with other metalloporphyrins (TiO_2|NiTCPP or TiO_2|CoTCPP), a freebase porphyrin (TiO_2|TCPP) or unmodified TiO_2. These results are shown in Figure 44b and summarized in Table 3. Electron spin resonance experiments indicated that upon light irradiation the Cu^{2+} ions in TiO_2|CuTCPP were partially reduced to Cu^{+}. Additionally, longer-term experiments involving three consecutive cycles of 5 h illumination periods showed TiO_2|CuTCPP maintained >95% of its initial photochemical activity. In addition to studies using sacrificial sources of electrons, PEC experiments were performed in 0.1 M aqueous K_2SO_4, under illumination from a Xe lamp (83.5 mW cm^{-2}) over a 6 min period, using working electrodes composed of 1 cm^2 FTO

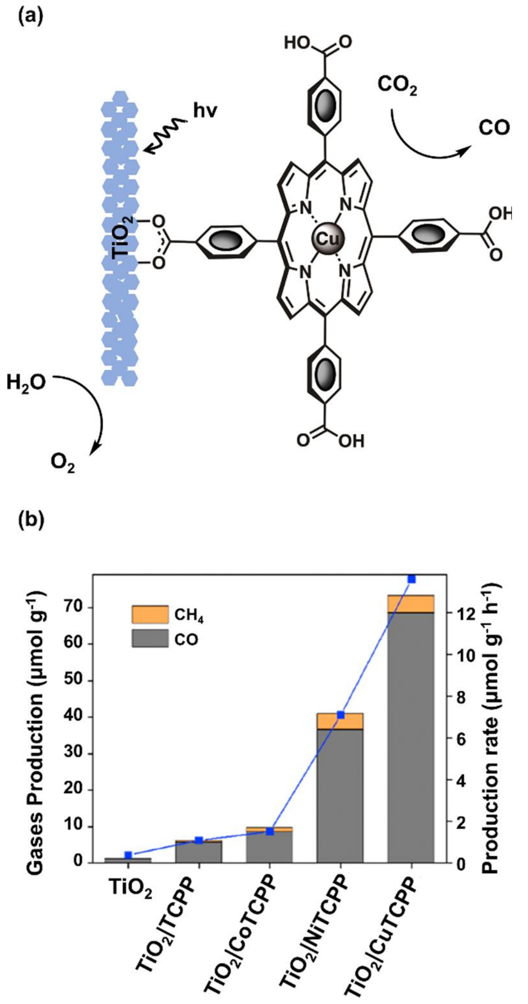

Figure 44. (a) Schematic representation of a carboxylate-modified copper porphyrin on TiO_2. (b) Amount of CH_4 (orange) and CO (gray) produced by TiO_2, TiO_2|TCPP, TiO_2|CoTCPP, TiO_2|NiTCPP, and TiO_2|CuTCPP in CO_2-saturated aqueous solutions under 83.5 mW cm^{-2} illumination. The rate for the formation of CO (blue squares) is included on the right-coordinate axis. Adapted with permission from ref 262. Copyright 2020 MDPI.

Table 3. Summary of Results from Wang and Co-workers[a]

sample	rate of CO formed (μmol CO g^{-1} h^{-1})	rate of CH_4 formed (μmol CH_4 g^{-1} h^{-1})
TiO_2	0.39	0.01
TiO_2|TCPP	1.08	0.06
TiO_2|CuTCPP	13.6	1.0
TiO_2|NiTCPP	7.08	0.89
TiO_2|CoTCPP	1.51	0.27

[a] Adapted with permission from ref 262. Copyright 2020 MDPI.

films with 2 mg of spin-coated TiO_2|MTCPP, a Pt plate as the counter electrode, and a Ag/AgCl as the reference electrode. These experiments showed that amongst the samples investigated TiO_2|CuTCPP generated the highest transient J (up to ~80 μA cm^{-2}), followed by TiO_2|NiTCPP (up to ~50 μA cm^{-2}), and then TiO_2|CoTCPP (<30 μA cm^{-2}).

Wang and co-workers have reported a photochemical system featuring cobalt phthalocyanines modified with carboxylic groups (CoPcCOOH) immobilized onto carbon nitride (CN) via acid−base interaction between their −COOH and −NH_2 groups.[263] The CN, prepared through pyrolysis of urea, was selected as a light absorber given its low cost, ease of preparation on relatively large scales, and lack of noble/toxic metals. Cobalt phthalocyanine was chosen because it is a relatively well-known catalyst for CO_2 electroreduction. The CN was ultrasonicated in a solution of CoPcCOOH in DMF to yield the catalyst-modified material (CN|CoPcCOOH) (Figure 45a). Immobilization of the catalyst was confirmed via XRD, SEM, aberration-corrected STEM, FTIR spectroscopy, XPS, and energy dispersive X-ray spectroscopy. A loading of 2.4% weight, as determined via ICP-MS, was consistent with the estimated loading of a monolayer of CoPcCOOH (2.38% weight). Photochemical experiments were performed using a reaction cell immersed in a water tank to cut off IR illumination and maintain room temperature. The cell contained 3 mg of CN|CoPcCOOH suspended in 5 mL of a CO_2-saturated 4:1 v/v MeCN:TEOA solution that was illuminated at an intensity of 300 mW cm^{-2} using a Xe lamp equipped with a AM 1.5 G filter. After 1 h of illumination, the CO production rate reached a maximum of 1067 μmol g^{-1} h^{-1} (Figure 45b) and a TOF of 33.2 h^{-1} as determined using GC. This production rate was 16 times higher than that achieved in control experiments using an analogous cobalt phthalocyanine without carboxylic groups, in place of CoPcCOOH. However, after 8 h, the CO production rate decreased to 780 μmol g^{-1}

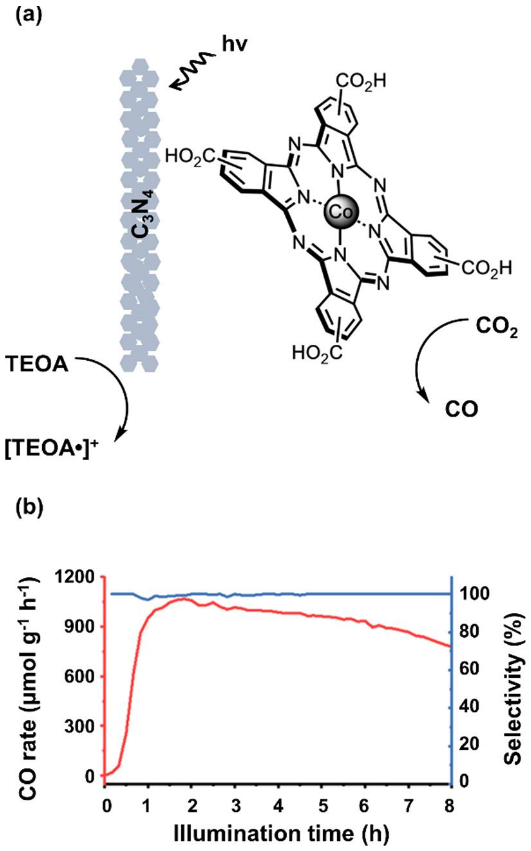

Figure 45. (a) Schematic representation of carbon nitride modified with a cobalt phthalocyanine. (b) Production rate for the formation of CO (red) by CN|CoPcCOOH in of CO_2-saturated 4:1 v/v acetonitrile:triethanolamine solution illuminated for 8 h by a Xe lamp equipped with a AM 1.5 G filter. Selectivity for CO (blue) is included on the right-coordinate axis. Adapted with permission from ref 263. Copyright 2022 American Chemical Society.

Table 4. Summary of Examples from Section 7

light absorber	catalyst	attachment chemistry	reaction medium/solvent	illumination source	|J| at E_{appl} (mA cm^{-2} at V)[a]	product (faradaic efficiency)	catalytic TON and TOF	ref
p-Si(100 or 111)	MeFCP-MePS (see Figure 7a)	Allyl linker	1 M $HClO_4$	Xe lamp at 870 mW cm^{-2}	231 at −0.8 V vs SCE	H_2 (n/a[b])	n/a and n/a	185
InP	$Fe_2S_2(CO)_6$ (see Figure 8)	1,4-benzedithiol	0.1 M $NaBF_4$ (pH 7)	LED lamp at 395 nm	n/a	H_2 (60%)	n/a and n/a	187
planar or pillar p-Si(100)	Mo_3S_4 (see Figure 9a)	Dropcasting	1 M $HClO_4$	Xe lamp at 620–1050 nm (AM 1.5G, 28.3 mW cm^{-2})	planar: 8 at 0, pillar: 9 at 0	H_2 (n/a)	n/a and planar: 960 s^{-1}, pillar: 65 s^{-1}	189
p-GaP(100) or p-Si(111)	NiP_2N_2 (see Figure 10)	Allyl linker	n/a	n/a	n/a	n/a (n/a)	n/a and n/a	190
p-GaP(100)	Cobaloxime (see Figure 11a)	PPy	1 M phosphate (pH 7)	Newport Oriel Apex (Xe lamp) at 100 mW cm^{-2} (AM 1.5G)	2.4 at +0.31	H_2 (n/a)	n/a and n/a	191
p-GaP(100)	Cobaloxime and Fluorinated cobaloxime (see Figure 11c)	PPy	0.1 M phosphate (pH 7) and 0.1 M acetate (pH 4.5)	Newport Oriel Apex (Xe lamp) at 100 mW cm^{-2} (AM 1.5G)	Cobaloxime: 0.56 at 0, Fluorinated Cobaloxime: 1.2 at 0	H_2 (97%)	n/a and n/a	192
p-GaP(100)	Cobaloxime (see Figure 11f)	PPy or PIm	0.1 M phosphate (pH 7)	Newport Oriel Apex (Xe lamp) at 100 mW cm^{-2} (AM 1.5G)	1 at +0.24, 1.3 at 0	H_2 (∼100%)	n/a and PPy: 2.1 s^{-1}, PIm: 2.4 s^{-1}	195
GaP(111A) or GaP (111B)	Cobaloxime	PIm	0.1 M phosphate (pH 7)	Newport Oriel Apex (Xe lamp) at 100 mW cm^{-2} (AM 1.5G)	0.89 at 0	H_2 (∼100%)	n/a and 7000 h^{-1}(1.94 s^{-1})	196
p-Si(100)-InP QDs	$Fe_2S_2(CO)_6$ (see Figure 12a)	Dropcasting	0.1 M H_2SO_4	W lamp at 1 sun (AM 1.5, 100 mW cm^{-2})	1.2 at −0.5 V vs Ag/AgCl	H_2 (n/a)	n/a and n/a	198
n-Si(111)	[Cp*Rh], [Cp*Ir], and $Ru(acac)_2$	Allyl linker	0.1 M $TBAF_6$ in MeCN	n/a	n/a	n/a (n/a)	n/a and n/a	200
p-Si(111)	NiPNP	Negishi Coupling	0.2 M $LiClO_4$ in MeCN	LED lamp at 33 mW cm^{-2}	18 at −0.9 V vs NHE	H_2 (n/a)	n/a and 285 s^{-1}	203
p-Si(100)	Cobalt benzenedithiolene polymer (see Figure 13a)	Dropcasting	0.05 M H_2SO_4 (pH 1.3)	Xe lamp at 100 mW cm^{-2} (AM 1.5G)	3.8 at 0	H_2 (80%)	n/a and n/a	205
$GaInP_2$-ALD TiO_2	Cobaloxime (see Figure 14a)	Carboxylate	0.1 M NaOH (pH 13)	Newport (Xe lamp) at 100 mW cm^{-2} (1 sun)	9 at 0	H_2 (∼100%)	139000 in 20 h and 1.9 s^{-1}	206
p-Si(111)-ALD AZO-TiO_2	Dubois type (see Figure 15a)	Phosphonate	0.2 M $LiClO_4$ in MeCN	LED lamp at 33 mW cm^{-2}	7 at −0.6 V vs NHE	H_2 (n/a)	n/a and n/a	207
p-Si(100)-AZO	[NiFeSe] H_2ase (see Figure 16a)	Dropcasting	50 mM MES (pH 6)	LED lamp at 10 mW cm^{-2}	0.075 at −0.55 V vs SHE	H_2 (96%)	n/a and n/a	111
B-doped p-Si(100)-IO-TiO_2	[NiFeSe] H_2ase (see Figure 17a)	Dropcasting	50 mM MES (pH 6.0) and 50 mM KCl	Newport Oriel Apex (Xe lamp) at 100 mW cm^{-2}, AM 1.5G and $\lambda > 420$ nm filters	0.5 at 0	H_2 (86 ± 8%)	n/a and n/a	209
Black p-Si(100)	[FeFe] H_2ase	Adsorption	1 M phosphate (pH 6.8)	W lamp at 5–50 mW cm^{-2}	1.4 at −0.5 V vs Ag/AgCl	H_2 (33%)	9.9×10^6 in 5 h and 1300 s^{-1}	210
p-Si-TiO_2	Dubois type	Phosphonate	0.1 M acetic acid (pH 4.5)	Newport Oriel (Xe lamp) 100 mW cm^{-2}, AM 1.5G and $\lambda > 400$ nm filters	0.34 at 0	H_2 (87% after 6 h, 76% after 24 h)	646 ± 141 in 24 h and n/a	128
p-GaP(100)	Fe and Co porphyrins (see Figure 18a)	Allyl linker	0.1 M phosphate (pH 7)	Newport Oriel Apex lamp at 100 mW cm^{-2}, AM 1.5G	1.3 at 0	H_2 (97%)	n/a and 3.9 s^{-1} Co^{-1}	211
p-GaP(100)	Fe, Co, Ni, Cu, and Zn porphyrins	Allyl linker	0.1 M phosphate (pH 7)	Newport Oriel Apex (Xe lamp) at 100 mW cm^{-2} (AM 1.5G)	n/a	n/a (n/a)	n/a and n/a	212
p-GaP(100)	Co porphyrin (see Figure 18c)	PPy	0.1 M phosphate (pH 7)	Newport Oriel Apex lamp at 100 mW cm^{-2}, AM 1.5	1.27 at 0	H_2 (93%)	n/a and 17.6 s^{-1} Co^{-1}	213
p-GaAs	Cobaloxime (see Figure 19a)	PPy	0.1 M phosphate (pH 7) and 0.1 M NaOH (pH 13)	Newport Oriel Apex lamp at 1 sun (100 mW cm^{-2})	20 at −0.2	H_2 (∼100%)	n/a and n/a	214
Zn-doped p-GaAs(100)	Fluorinated benzenes (see Figure 20)	Lithium/Grignard	3 M H_2SO_4 (pH −0.5)	Newport W lamp at 1 sun (100 W m^{-2})	20.5 at −0.5	n/a (n/a)	n/a and n/a	215

Table 4. continued

light absorber	catalyst	attachment chemistry	reaction medium/solvent	illumination source	$\lvert J \rvert$ at E_{appl} (mA cm^{-2} at V)[a]	product (faradaic efficiency)	catalytic TON and TOF	ref
LCTA-TiO_2	NiP_2N_2	Phosphonate	0.1 M Na_2SO_4 (pH 3)	SAN-EI Solar Simulator at 100 mW cm^{-2}, AM 1.5 ($\lambda > 300$ nm)	0.2 at +0.3	H_2 (87%)	50 in 3 h and n/a	216
B-doped p-Si(100)-ALD TiO_2	Cobaloxime (see Figure 21a)	Phosphonate	1 M phosphate (pH 7)	Newport Xe lamp at AM 1.5 (100 mW cm^{-2})	1.3 at 0	H_2 (84%)	260 in 1 h and 0.071 s^{-1}	217
$CuFe_xO_y$	Cobaloxime (see Figure 22)	Carboxylate	0.2 M phosphate buffer (pH 6.7)	Xe lamp at 65 or 100 mW cm^{-2}	0.004 at +0.4	H_2 (56%)	90 ± 30 in 20 min and 0.08 s^{-1}	218
Black Si(100)	Cobalt bis(benzene-dithiolate)	$\pi-\pi$ interactions	0.1 M H_2SO_4 (pH 1.5)	ABET Technologies Sun 3000 Solar Simulator at 1 sun (100 mW cm^{-2})	35 at −1.7	n/a (n/a)	n/a and >110 s^{-1}	220
p-Si-TiO_2	$[Co(CR\text{-}DCP)Br_2]^+$ (see Figure 23a)	Carboxylate	0.1 M acetate buffer (pH 4.5)	Xe lamp at 100 mW cm^{-2}	0.682 at 0 (LSV), 0.527 ± 0.035 at 0 (CPPE)	H_2 (80 ± 4%)	n/a and n/a	222
p-InP	Formate dehydroge-nase	Not Immobilized	0.5 M phosphate buffer (pH 6.8), 0.5 M sodium bicarbonate, and 2 mM methyl viologen	Xe lamp at 59–60 mW cm^{-2} ($\lambda < 400$ nm)	0.6 at + 0.05 V vs NHE	$HCOO^-$ (89%)	21,000 and n/a	223
Zn-doped p-InP	RCP (see Figure 24a)	Electropolymerized	H_2O	Xe lamp at 400–800 nm	75 μA at −0.6 V vs Ag/AgCl	$HCOO^-$ (62.3%)	>12 in 3 h and n/a	224
InP	polyRuCA + polyRuCE (see Figure 25a)	Phosphate ethyl, Pyrrolyl	H_2O	Xe lamp at 70 sun	n/a	$HCOO^-$ (78%)	>17 in 24 h and n/a	225
CZTS	Ru polymers	Dropcasting/Phosphonate	H_2O	Xe lamp at 400–800 nm (70x AM 1.5)	~0.25 at −0.4 V vs Ag/AgCl	$HCOO^-$ (80%)	>5 in 3 h and n/a	226
SiGe-jn	Ru polymer (see Figure 26a)	Dropcasting	0.1 M phosphate buffer (pH 6.4)	Xe MAX-320 Asahi Spectra at 1 sun (AM 1.5, 100 mW cm^{-2})	n/a	$HCOO^-$ (93%)	n/a and n/a	228
Cu_2O-AZO-TiO_2-FTO	Lehn's Re(see Figure 27a)	Phosphonate	0.1 M $TBAF_6$ in MeCN	LOT Oriel Xe lamp calibrated to 1 sun	2.5 at −1.9 V vs Fc^+/Fc	CO (80–95%)	>70 in 1.5 h and n/a	229
Si nanowire	Re-NHC's	Adsorption	0.1 M $TBAF_6$ in MeCN and 5% H_2O	Xe lamp 113 mW cm^{-2}	4 at −1.51 V vs Fc^+/Fc	CO (68%)	20.4 in 4 h and n/a	233
Cr_2O_3, N,Zn-Fe_2O_3, TiO_2	Lehn's Ru polymer	Dropcasting	0.1 M $KHCO_3$ (pH 6.6)	HAL-320 lamp at 1 sun (AM 1.5, 100 mW cm^{-2})	0.15 at +0.1	HCOOH (80%)	304 in 13 h and n/a	234
p-Si-GaN nanowires-ALD NiO	Lehn's Ru (see Figure 28)	Carboxylic acid	50 mM $NaHCO_3$ (pH 6.8)	Newport Xe lamp at 100 mW cm^{-2}, AM 1.5G	1.1 at −0.25	$HCOO^-$ (64%)	n/a and n/a	236
Si-TiO_2	Co bis(terpyridine)	Phosphonate	0.1 M $TBAF_6$ in 6:4 MeCN:H_2O	Newport Oriel Xe lamp at AM 1.5G, 100 mW cm^{-2}, $\lambda > 400$ nm	0.250 at −0.95 V vs Fc^+/Fc	CO (48%)	159 in 8 h, 381 in 24 and 16 h^{-1} (0.004 s^{-1})	237
NiO-$CuInS_2$ QD	Lehn's Re (see Figure 29a)	Dropcasting/Phosphonate	0.1 M $TBAF_6$ in DMF	LED lamp at 1 sun (420–750 nm)	0.025 at −0.87 V vs NHE	CO (32%)	11 in 100 min and n/a	238

[a] All potentials are reported vs RHE, unless otherwise stated. [b] n/a = information/data not available.

Table 5. Summary of Examples from Section 8

light absorber	catalyst	attachment chemistry	reaction medium/solvent	illumination source	product (quantum efficiency)	catalytic TON and TOF	ref
CdSe-ZnS QD	Cobaloxime (see Figure 30a)	Phosphonate	Toluene, TEA·HCl, TEOA	Xe lamp with a $\lambda > 400$ nm filter	H_2 (n/a)[a]	10,000 in 10 h and n/a	239
CdS NR	[FeFe]-H_2ase (see Figure 31a)	Carboxylate	50 mM TrisHCl, 5 mM NaCl, 5% glycerol, pH 7 buffer	405 nm LED lamp at 800 μE m^{-2} s^{-1} (∼AM 1.5 G)	H_2 (20%)	10^6 in 4 h and 350 s^{-1}	26
N-doped p-Ta_2O_5	Lehn's Ru (see Figure 32a)	Carboxylate	1:5 TEOA:MeCN	500 W Xe lamp at 410−750 nm	HCOOH (1.90%)	89 in 8 h and n/a	245
N-doped p-Ta_2O_5	Lehn's Ru (see Figure 33a)	Phosphonate	1:5 TEOA:MeCN	500 W Xe lamp at 410−750 nm	HCOOH (n/a)	118 in 60 h and n/a	246
CdS QD or NR	[Ni4Fe-4S] dehydrogenase (see Figure 34b and 34c)	Adsorption	0.35 M MES	W lamp at ca. 23 mW cm^{-1} ($\lambda > 420$ nm)	CO (10^{-4})	n/a and QD: 0.25 s^{-1}, NR: 1.23 s^{-1}	247
TiO_2 (P25)	Co cyclam (see Figure 35a)	Adsorption	4:1:1 MeCN:TEOA:MeOH	Hg lamp at 100 mW cm^{-2}	CO (n/a)	In 4 h: Reflux method: 12.2, Microwave method: 19.7 and n/a	248
mpg-C_3N_4	RuCP (see Figure 36a)	Phosphonate	1:4 TEOA:MeCN	450 W Hg lamp at $\lambda > 400$ nm	HCOOH (1.5%)	>200 in 20 h and n/a	249
mpg-C_3N_4	RuP (see Figure 36a)	Phosphonate	1:4 TEOA:DMA	400 W Hg lamp at $\lambda > 400$ nm	HCOOH (n/a)	∼1000 in 20 h and n/a	250
mpg-C_3N_4	RuP or RuC (see Figure 36a)	RuP: Phosphonate, RuC: Carboxylate	1:4 TEOA:MeCN	400 W Hg lamp at $\lambda > 400$ nm	HCOOH (n/a)	In 5 h: RuC: 110, RuP: 170 and RuC: 40 h^{-1} (0.01 s^{-1}), RuP: 20 h^{-1} (0.005 s^{-1})	251
mpg-C_3N_4	RuP (see Figure 36a)	Phosphonate	1:4 MeOH:DMA	400 W Hg lamp at $\lambda > 400$ nm	CO (n/a)	7.5 in 20 h and n/a	252
mpg-C_3N_4	CoPPc (see Figure 37a)	Dropcasting	1:4 TEOA:MeCN	Newport Oriel Xe lamp at AM 1.5G, 100 mW cm^{-2} ($\lambda > 400$ or 300 nm)	CO (n/a)	In 48 h: $\lambda > 400$ nm: 51, $\lambda > 300$ nm: 84 and n/a	254
CdS NR	2-Oxoglutarate:ferredoxin oxidoreductase (see Figure 38)	Carboxylate	20.5 mM MES/HEPES/TAPS pH 6.8 buffer, 7 mM 2-mercaptoethanol, 625 μM TPP, 500 μM $MgCl_2$, 10 mM NH_4Cl, 1.7 μM GDH, 252 μM NADH, and 30 mM $NaHCO_3$	405 nm CW diode laser at 32 mW	2-oxoglutarate (n/a)	n/a and 39 min^{-1} (0.65 s^{-1})	255
mpg-C_3N_4	Co quaterpyridine (see Figure 39a)	Covalent-amide	0.05 M BIH, 0.03 M PhOH in MeCN	AM 1.5 simulator with a Xe lamp at $\lambda > 400$ nm	CO (0.25%)	128 in 24 h, 486 in 4 × 24 h and n/a	256
GA	Co quaterpyridine (see Figure 40a)	Covalent-amide	0.05 M BIH, 0.1 M PhOH (or 1.51 M TEOA) in MeCN	AM 1.5 simulator with a Xe lamp at $\lambda > 400$ nm	With PhOH: CO (0.57%). With TEOA: $HCOO^-$ (0.85%)	With PhOH: 513 in 222 h, and 1900 in 4 × 216 h, With TEOA: 330 in 72 h, 1300 in 4 × 72 h. and n/a	258
g-C_3N_4	Bipy-triCO-Mn-Br complex see Figure 41)	Phosphonate	H_2O as solvent and 6 mL of TEOA	500 W Xe arc lamp at $\lambda >$ 400 nm	CO (n/a)	102 in 8 h and n/a	259
g-CNU	Co porphyrin (see Figure 42a)	π−π stacking	1:4 TEOA:MeCN	LED lamp at 75 mW cm^{-2} ($\lambda > 400$ nm)	CO (n/a)	n/a and 7.1 h^{-1} (0.002 s^{-1})	260
g-C_3N_4	Cu phthalocyanine (see Figure 43a)	Hydrogen bonding	H_2O	300 W Xe lamp at $\lambda \geq 400$ nm	CO (0.70%)	n/a and n/a	261
TiO_2 (P25)	Cu porphyrin (see Figure 44a)	Carboxylate	H_2O as electron donor	Xe lamp at 83.5 mW cm^{-2}	CO (n/a)	n/a and n/a	262
C_3N_4	Co phthalocyanine (see Figure 45a)	Carboxylate	1:4 TEOA:MeCN	Xe lamp at 300 mW cm^{-2}	CO (0.90%)	221 in 8 h and 33.2 h^{-1} (0.009 s^{-1})	263

[a] n/a = information/data not available.

h^{-1}, yielding a TON of 221. Throughout the 8 h of the experiment, H_2 was the only subproduct, whereas the selectivity of CO over H_2 stayed over 98%. No liquid products were detected using NMR spectroscopy. When the reaction was illuminated with a 365 nm LED light, the apparent external quantum yield of CO_2 to CO was 0.90%. Upon increasing the loading from 2.4% to 10% weight, the material showed no CO production activity. The authors suggested that aggregated CoPcCOOH, which is electrically insulating, could not efficiently transfer electrons from CN to CO_2. The authors also attributed the increasing and decreasing CO production rates to activation and deactivation processes, respectively, where the activation, as indicated by UV−vis and XPS measurements performed in situ and with a chemical reducing agent, involves a 4 e^- reduction to generate the active cocatalysts. Analysis of the electrolyte, via ICP-MS, and following 12 h of operation, indicated that 58% of the Co in the starting CN|CoPcCOOH had leached into the solution. Control experiments performed using CN and CoPcCOOH dissolved in DMF yielded approximately 60% of the activity achieved using CN|CoPcCOOH, indicating the deactivation is not due to catalyst dissolution.

9. TABULATED SUMMARY OF EXAMPLES

In this section, we provide Tables 4 and 5 summarizing the examples presented in Sections 7 and 8, respectively. Additionally, an expanded version of Table 4 is provided in the Supporting Information including information on the reference and counter electrodes used.

10. CRITICAL ANALYSIS, CONCLUSIONS, AND OUTLOOK

A range of strategies have been developed for interfacing molecular components with semiconducting materials and studying the resulting assemblies. In addition to offering opportunities to store solar energy as fuels, advances in this area have brought forth creative synthetic solutions for assembling combinations of hard- and soft-matter materials. Nonetheless, the span of time and length scales associated with transducing solar energy present formidable challenges for understanding and controlling light harvesting, energy transfer, charge separation, catalytic reactions, product selectivity, and interfacial processes. Although there are well-defined and established methods available for characterizing diagnostic- and benchmarking-type efficiencies of artificial photosynthetic assemblies, comparisons are complicated by differences in cost/scalability of the materials used, durability of the assemblies, and the experimental conditions they are operated under (e.g., cell configuration, illumination source, supporting electrolyte, pH, etc.) Further, unlike for molecular electrocatalysts,[264,265] there is a lack of approaches available for extracting thermodynamic and kinetic parameters associated with molecular electrocatalysts immobilized on semiconductor surfaces.

Efficiency, cost/scalability, and durability are required features for large-scale, global implementation of solar-to-fuel technologies, and promising strategies for imparting these properties are highlighted in this review. These include examples of using semiconductors with relatively narrow band gaps to promote effective light absorption across the solar spectrum (refs 111, 128, 189−191, 203, 205, 207, 209, 214, 217, 218, 226, 228, and 237), modulating the surface of the semiconductors with ions or molecular dipoles for directing interfacial energetics and charge transfer efficiencies,[207,215,220,266] protecting the surface of semiconductors with stable overcoating layers to increase stability during photoelectrochemical operation (refs 111, 128, 191, 192, 195, 196, 198, 200, 206, 207, 209, 213−218, 222, 229, 234, 236, 237, and 267), increasing the surface loadings of catalysts via leveraging nanostructured materials or overlayers (refs 128, 209, 217, 228, 229, 237, 238, 249−252, 254, and 256), and passivating surface states (i.e., electronic states found at the surface of materials) via chemisorption with the aim of suppressing surface recombination.[128,196,200,203,208,209,216−218] Despite these advances, an artificial photosynthetic construct has yet to effectively demonstrate all three of the desirable properties illustrated in Figure 46.[268] Looking forward, outstanding research opportunities and questions in the areas of artificial photosynthesis and solar fuels include:

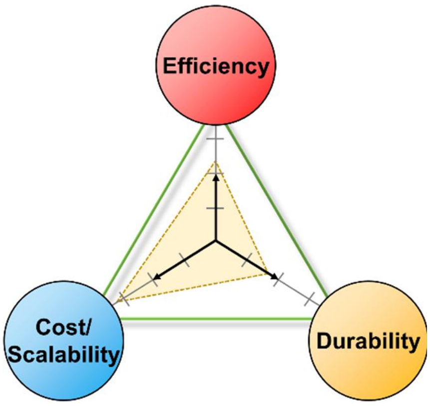

Figure 46. A "golden triangle" for practical solar-fuel production, indicating the desired parameters of efficiency, lifetime, and cost/scalability (the inserted yellow triangle is included for illustrative purposes).

- What are the dominant interactions across length and timescales that control the performance of molecular-modified semiconductors and hierarchical materials?
- How can the molecular science of individual processes in solar fuels generation be leveraged to inform the rational design of systems with enhanced lifetimes, scalability, and efficiencies?
- How do we probe, understand, and tailor the structure, composition, and dynamics of the local region surrounding catalytic active sites to direct chemical reaction pathways?
- What are the degradation mechanisms responsible for photoelectrosynthetic performance loss over time and what strategies can be developed for bypassing them?
- How can we better couple hypothesis-based synthesis with data-science tools, including machine learning and artificial intelligence, to predict effective combinations of the component materials and their reaction environments?

The opportunities and challenges outlined above apply broadly to realizing practical solar-to-fuel devices. Opportunities and challenges specific to developing molecular-modified photocathodes include controlling the selectivity for producing a desired chemical product or type of solar fuel. As illustrated in Table 1, the hydrogen evolution and CO_2 reduction half reactions occur within a relatively narrow potential range, presenting energetic challenges for selectively driving a desired reaction. This figure is also somewhat incomplete, meaning the values listed in Table 1 are formal potentials representing the average energy per electron transferred. Thus, for non-concerted, or stepwise reactions that are not redox leveled, each individual electron is not necessarily transferred at the average value. Further, these thermodynamic potentials do not address transition-state energies, which are central to catalysis and reaction selectivity. Although it is plausible that appropriately designed photocathodes could drive multi-electron, multiproton reactions such as CO_2 reduction without the use of electron transport/protection layers and/or metal cocatalyst, coating layers provide a promising approach. Like enzymes, molecular materials provide precise three-dimensional environments that could be designed to provide specificity for tightly binding an "activated complex" (i.e., a transition state) and thus achieve exquisite selectivity. Auxiliary design features include not only the selection of metal ions of the catalyst[261,262,269] but also the structure of the surrounding coordination spheres,[270] and acidity of any proton relays[252,253,258] for suppressing or controlling rates of hydrogen evolution.[271] In general, a more complete understanding of the photoelectrosynthetic processes occurring at a cathode will require consideration of the lower concentrations of electrons at semiconductor surfaces as compared to those at metal surfaces during electrocatalysis, as well as the interplay between light flux, quantum efficiency, and catalytic site turnover frequencies. In principle, such photodriven assemblies may be capable of using light intensity to control product selectivity, offering a promising tool compared to the metal/conducting electrodes more traditionally used in electrocatalysis.[241] In the case of producing reduced forms of CO_2 as a fuel, and as shown in Table 1, reduction of CO_2 is challenging, especially in aqueous conditions, considering competitive proton reduction that can lead to poor selectivity for carbonaceous products. In addition, CO_2 has a low solubility in water (~0.034 M), adversely affecting diffusion-controlled reactions.[272]

Other challenges central to development of molecular-modified photocathodes include exploration of light-absorbing materials and molecular catalysts that are stable under extreme pH conditions, or that can effectively operate at near-neutral pH. Each experimental operating condition has its own pros and cons in terms of stability, efficiency, and safety, and there is no consensus on what operating conditions should take precedence in developing potential future devices and technologies. Although extreme pH can have advantages in terms of energetics and rates of fuel production,[273] the selection of semiconductor electrodes and catalysts that withstand such caustic conditions is limited. Near-neutral pH conditions relax stability constraints and mitigate risks associated with managing corrosive solutions covering large land mass areas. However, the concentration of protons and hydroxide ions at near-neutral pH conditions are relatively low and can limit mass-transport or require relatively large amounts of supporting electrolyte to lower the solution resistance and mitigate concentration gradients.[274] Additionally, CO_2 reduction under alkaline conditions results in the formation of CO_3^{2-}.[275] Research efforts should account for the limitations associated with each set of operating conditions. Detailed mechanistic understanding of degradation processes will likely facilitate improvements in stability. Nonetheless, nature offers design inspiration for achieving durability via repair rather than inherent stability of the component materials. In biological photosynthesis durability is achieved via continuous repair cycles. For example, the D1 complex that houses the manganese-based water oxidation catalyst lasts only for ~30 min before it is reassembled.[276]

Beyond the materials and component levels, effective interfaces and collaborations between researchers, team managers, and leaders at the organizational level will be crucial to the development and global implementation of practical solar-fuel and artificial photosynthetic systems.[32,277] In nature, healthy large-scale systems require diversity. In this vein, it may be beneficial to enable diverse strategies for researching and envisioning approaches to developing artificial photosynthesis as well as not prematurely choosing a winning approach or set of operating conditions. The research opportunities, advances, and challenges summarized in this review exemplify the potential scientific impact of harnessing solar energy to produce fuels.[13,15,278−281] Progress in these areas would enable more informed rational synthesis of artificial photosynthetic systems with enhanced overall performance. Although several approaches, including molecular, solid-state, and enzymatic based strategies, are currently being pursued to achieve efficient, low cost, and robust assemblies for converting sunlight to fuels, we imagine that as molecules become increasingly complex, surfaces more tailored, and synthetic biology expands to introduce novel functionalities into proteins, such distinctions will become further blurred.

ASSOCIATED CONTENT

SI Supporting Information

The Supporting Information is available free of charge at https://pubs.acs.org/doi/10.1021/acs.chemrev.2c00200.

Expanded version of Table 4 including information on the reference and counter electrodes (PDF)

AUTHOR INFORMATION

Corresponding Author

G. F. Moore − *School of Molecular Sciences and the Biodesign Institute Center for Applied Structural Discovery (CASD), Arizona State University, Tempe, Arizona 85287-1604, United States*; orcid.org/0000-0003-3369-9308; Email: gfmoore@asu.edu

Authors

Edgar A. Reyes Cruz − *School of Molecular Sciences and the Biodesign Institute Center for Applied Structural Discovery (CASD), Arizona State University, Tempe, Arizona 85287-1604, United States*; orcid.org/0000-0001-7307-7613

Daiki Nishiori − *School of Molecular Sciences and the Biodesign Institute Center for Applied Structural Discovery (CASD), Arizona State University, Tempe, Arizona 85287-1604, United States*; orcid.org/0000-0002-4707-0896

Brian L. Wadsworth − *School of Molecular Sciences and the Biodesign Institute Center for Applied Structural Discovery (CASD), Arizona State University, Tempe, Arizona 85287-1604, United States*; orcid.org/0000-0002-0274-9993

Nghi P. Nguyen − *School of Molecular Sciences and the Biodesign Institute Center for Applied Structural Discovery (CASD), Arizona State University, Tempe, Arizona 85287-1604, United States*; orcid.org/0000-0002-8970-3372

Lillian K. Hensleigh − *School of Molecular Sciences and the Biodesign Institute Center for Applied Structural Discovery (CASD), Arizona State University, Tempe, Arizona 85287-1604, United States;* orcid.org/0000-0002-2202-0999

Diana Khusnutdinova − *School of Molecular Sciences and the Biodesign Institute Center for Applied Structural Discovery (CASD), Arizona State University, Tempe, Arizona 85287-1604, United States;* orcid.org/0000-0002-5382-7023

Anna M. Beiler − *School of Molecular Sciences and the Biodesign Institute Center for Applied Structural Discovery (CASD), Arizona State University, Tempe, Arizona 85287-1604, United States;* orcid.org/0000-0003-1027-3304

Complete contact information is available at:
https://pubs.acs.org/10.1021/acs.chemrev.2c00200

Author Contributions

[†]E.A.R.C., D.N., and B.L.W. contributed equally. CRediT: **Edgar Alejandro Reyes Cruz** writing-review & editing; **Daiki Nishiori** writing-review & editing; **Brian L. Wadsworth** writing-review & editing; **Nghi P. Nguyen** writing-review & editing; **Lillian Hensleigh** writing-review & editing; **Diana Khusnutdinova** writing-review & editing; **Anna M Beiler** writing-review & editing; **Gary F. Moore** conceptualization, visualization, writing-review & editing.

Notes

The authors declare no competing financial interest.

Biographies

Edgar A. Reyes Cruz obtained a B.Sc. in chemistry in 2014 at the Instituto Tecnológico y de Estudios Superiores de Monterrey (ITESM), where he worked on the synthesis and characterization of phthalocyanines for dye-sensitized solar cells with Prof. Ernesto Mariño, and model porphyrins with Prof. Ana L. Moore at Arizona State University. Reyes joined the research group of Prof. Gary F. Moore at Arizona State University in 2016 to pursue his Ph.D. studies. His graduate research focuses on the synthesis and characterization of catalyst for carbon dioxide reduction.

Daiki Nishiori earned a M.Sc. in chemistry from the University of Tokyo in 2018 under the supervision of Prof. Hiroshi Nishihara, where he studied hybrid nanomaterials containing photosynthetic proteins for hydrogen evolution and photon detection. Nishiori joined Prof. Gary F. Moore's research group at Arizona State University in 2018 to pursue his Ph.D. studies. His graduate research involves the immobilization of molecular catalysts on semiconductor surfaces and development of oxygen reduction molecular catalysts.

Brian L. Wadsworth received his Ph.D. at Arizona State University in 2020 under Prof. Gary F. Moore, developing electrochemical and spectroscopic techniques to investigate the nano-, micro-, and macro-level properties of molecular fuel-forming electrocatalysts immobilized at electrified interfaces or dissolved in solutions. He received B.A.s in chemistry and biochemistry from Coe College in Cedar Rapids, Iowa in 2015.

Nghi P. Nguyen obtained her B.Sc. in chemistry from Ho Chi Minh City, University of Science in 2017, where she performed research involving dye-sensitized solar cells and perovskite solar cells for applications in energy conversion and environmental remediation. Nguyen joined Prof. Gary F. Moore's research group at Arizona State University in 2018 to pursue her Ph.D. studies. Her graduate research efforts focus on (semi)conductor surface-modification chemistry and the photoelectrochemistry of solar fuels generation.

Lillian K. Hensleigh received her B.Sc. in chemistry and biology from the University of Redlands, CA in 2011, where her undergraduate research focused on analytical soil analysis in Joshua Tree National Park for the purpose of informing environmental restoration efforts. Hensleigh began working with Prof. Gary F. Moore's research group at Arizona State University in the spring of 2020 before enrolling in the biochemistry Ph.D. program in the fall of 2020. Her research focuses on solar-to-fuel energy conversion and the synthesis and characterization of bioinspired photoelectrosynthetic materials.

Diana Khusnutdinova obtained her Ph.D. at Arizona State University in 2019, where she worked with the research group of Prof. Gary F. Moore, studying the design and synthesis of metalloporphyrins and their applications in electrocatalytic and photoelectrosynthetic assemblies for solar energy conversion. She received her B.Sc. and M.Sc. in chemical engineering from the Kazan National Research Technological University in 2010, and her M.Sc. in nanoscience from Arizona State University in 2013.

Anna M. Beiler received her Ph.D. at Arizona State University in 2018 under Prof. Gary F. Moore and Prof. Thomas A. Moore, where she examined the electrochemistry of non-natural amino acid containing proteins and the functionalization of gallium phosphide semiconductors with cobalt-based molecular catalysts for solar-driven hydrogen evolution. She continued her research in solar fuels as a Swedish Olle Engkvist Foundation Postdoctoral Fellow at Uppsala University under Prof. Sascha Ott, studying the integration of metal−organic frameworks with semiconductors for photoelectrochemical applications.

G. F. Moore earned his Ph.D. in chemistry and biochemistry at Arizona State University in 2009 under Prof. Ana L. Moore. In 2011, after completing a Camille and Henry Dreyfus Postdoctoral fellowship at Yale University under Prof. Gary W. Brudvig and Prof. Robert H. Crabtree, he became a staff scientist at Lawrence Berkeley National Laboratory. In 2014, Moore returned to Arizona State University as a member of the faculty in the School of Molecular Sciences. He is a Julie Ann Wrigley Global Institute for Sustainability Scholar, a Department of Energy Early Career Awardee, a Camille Dreyfuss Teacher-Scholar, and a National Science Foundation (NSF) CAREER Awardee.

ACKNOWLEDGMENTS

This material is based upon work supported by the National Science Foundation under Early Career Award 1653982 (materials and synthesis) and by the U.S. Department of Energy, Office of Science, Office of Basic Energy Sciences, under Early Career Award DE-SC0021186 (modeling and benchmarking). G.F.M. acknowledges support from the Camille Dreyfus Teacher-Scholar Awards Program. B.L.W. and A.M.B. were supported by IGERT-SUN fellowships, funded by the National Science Foundation (1144616), and the Phoenix Chapter of the ARCS Foundation. D.N. was supported by the Heiwa Nakajima Foundation.

ABBREVIATIONS

α = absorption coefficient of a photoelectrode
AA = ascorbic acid
ABPE = applied bias photon-to-current efficiency
acac = acetylacetonate
AFM = atomic force microscopy
Ag/AgCl = silver/silver chloride reference electrode
ALD = atomic layer deposition
APCE = absorbed photon-to-current efficiency

ATP = adenosine triphosphate
ATR-IR = attenuated total-reflection infrared
AZO = aluminum-doped zinc oxide
A_0 = chlorophyll *a*
A_1 = phylloquinone
BIH = 1,3-dimethyl-2-phenyl-2,3-dihydro-1H-benzo[d]-imidazole
bpy = 2,2′-bipyridine
b-Si = black silicon
CN = carbon nitride
[Co] = cobalt bis(benzene-dithiolate)
CODH = carbon monoxide dehydrogenase
Cp* = pentamethylcyclopentadienyl
cyclam = 1,4,8,11-tetraazacyclotetradecane
Cyt b_6f = cytochrome plastoquinol-plastocyanin-oxidoreductase
CZTS = Cu_2ZnSnS_4
C = unoxidized catalyst site concentration
$\hat{C}$ = total catalyst site concentration
C^+ = oxidized (activated) catalyst site concentration
C_A^0 = concentration of the chemical substrate
DBU = 1,8-diazabicyclo[5.4.0]undec-7-ene
dcbpy = 4,4′-dicarboxy-2,2′-bipyridine
DLS = dynamic light scattering
DMA = dimethylacetamide
DMF = dimethylformamide
DMSO = dimethylsulfoxide
dpbpy = 4,4′-diphosphate-2,2′-bipyridine
DRS = diffuse reflectance spectroscopy
ε = static dielectric constant
ε_0 = permittivity of free space
E = electrode potential
EDX = energy-dispersive X-ray spectroscopy
EIS = electrochemical impedance spectroscopy
EQE = external quantum efficiency
ESI = electron-spray ionization
E_{CB} = conduction band-edge potential
E_F = semiconductor Fermi level
$E_{F,n}$ = electron quasi-Fermi level
$E_{F,p}$ = hole quasi-Fermi level
$E_{H+/H2}$ = redox potential of the H^+/H_2 couple
E_{PQ}^0 = standard reduction potential of the catalyst
$[E_T]$ = total concentration of enzyme
E_{VB} = valence band-edge potential
$\vec{E}$ = electric field intensity
F = Faraday constant
FE = Faradaic efficiency
FTO = fluorine-doped tin oxide
FTIR = Fourier-transform infrared
F_A, F_b, and F_x = iron−sulfur protein clusters
$\vec{F}$ = force experienced by a unit charge
Γ_{C_T} = per geometric area surface densities of total catalysts
$\Gamma_{C'}$ = per geometric area surface densities of activated catalysts
GA = graphene acid
GATR-FTIR = grazing-angle total reflection Fourier-transform infrared
GC = gas chromatography
GC−MS = gas chromatography−mass spectrometry
GDH = glutamate dehydrogenase
G3P = glyceraldehyde-3-phosphate
g-C_3N_4 = graphitic carbon nitride
η = overpotential
HEPES = 4-(2-hydroxyethyl)-1-piperazineethanesulfonic acid
HER = hydrogen evolution reaction
H_{AB} = electronic matrix element
IC TOF-MS = ion chromatography time-of-flight mass spectroscopy
ICP-AES = inductively coupled plasma atomic emission spectrometry
ICP-MS = inductively coupled plasma mass spectrometry
ICP-OES = inductively coupled plasma optical emission spectrometry
IO = inverse opal
IPCE = incident photon-to-current efficiency
IQE = internal quantum efficiency
ITO = indium tin oxide
I_0 = incident photon flux on the semiconductor after correcting for interface reflection and electrolyte absorption losses
J = current density
J_{cat} = catalyst solution current density
J_g = minority carrier current density
J_{jxn} = semiconductor-catalyst current density
J_n = current density due to electrons
J_n^0 = exchange current density due to electrons
J_p = current density due to holes
J_p^0 = exchange current density due to holes
J_{ph} = photocurrent density
J_{sc} = short-circuit current density
J_{SCR} = electron photocurrent current density in the space-charge region
J_w = electron current density at the depletion edge
J_0 = saturation current density
K = equilibrium constant for a reaction
k = apparent rate constant associated with a catalytic reaction
k_B = Boltzmann constant
k_{cat} = forward rate constant for chemical catalysis
k_{-cat} = reverse rate constant for chemical catalysis
K_d = dissociation constant for the enzyme−substrate complex
k_{et} = forward rate constant for electron transfer
k_{-et} = reverse rate constant for electron transfer
k_f = forward rate constant describing the binding and unbinding of the substrate to the enzyme
k_{ht} = forward rate constant for hole transfer
k_{-ht} = reverse rate constant for hole transfer
k_r = reverse rate constant describing the binding and unbinding of the substrate to the enzyme
K_M = Michaelis constant
K_r = recombination losses in the space-charge region
K^{-1} = equilibrium constant equal to the ratio of the forward and reverse rate constants for electron transfer from the semiconductor
λ = reorganization energy
L = minority charge carrier diffusion length
LCTA = $La_5Ti_2Cu_{0.9}Ag_{0.1}S_5O_7$
LHE = light harvesting efficiency
μ = minority-carrier mobility
MeCN = acetonitrile
MeFCP = methylferrocenophane
MeOH = methanol
MePS = poly(chloromethyl)-styrene
MES = 2-(N-morpholino)ethanesulfonic acid

MmOGOR = 2-oxoglutarate:ferredoxin oxidoreductase from *Magnetococcus marinus*
MPA = 3-mercaptopropionate
mpg-C_3N_4 = mesoporous-graphitic carbon nitride
NADH = nicotinamide adenine dinucleotide
NADPH = reduced nicotinamide adenine dinucleotide phosphate
Nap = naphthalene
NHE = normal hydrogen electrode
NMR = nuclear magnetic resonance
NR = nanorod
nsg-C_3N_4 = nanosheets of graphitic carbon nitride
N = amount of chemical product
N_A = Avogadro constant
N_{cat} = total amount of catalyst on the surface
N_D = doping density
$N_{\text{per unit of time}}$ = amount of product generated per unit of time
n = number of electrons required for the chemical transformation
n_i = intrinsic carrier concentration
n_s = surface electron concentration under steady-state illumination
n_{s0} = surface electron concentration at equilibrium
n_w = electron density at the depletion edge
n_0 = electron concentration/density in the bulk
OEC = oxygen evolving complex
PCET = proton-coupled electron transfer
PEC = photoelectrochemical
PESA = photoelectron spectroscopy in air
pFF = pseudo fill factor
PIm = polyimidazole
PNP = $Ph_2PCH_2NCH_2PPh_2$
PPc = polymeric phthalocyanine
PPy = polypyridyl
PSI = photosystem I
PSII = photosystem II
PV = photovoltaic
Pyr = pyrene
p_s = surface hole concentration under steady-state illumination
p_{s0} = surface hole concentration at equilibrium
P_{total} = power density
Q = point charge
QD = quantum dot
q = unit charge
q_p/A = photon flux per geometric area
qV_{cat} = chemical potential difference cross the catalyst layer
R = gas constant
RHE = reversible hydrogen electrode
R_{ct} = interfacial electron transfer resistance
r = distance
$[S]$ = substrate concentration of an enzymatic reaction
SCE = saturated calomel electrode
SCoA = succinyl-coenzyme A
SEM = scanning electron microscopy
SS-SPS = steady-state surface photovoltage spectroscopy
STEM = scanning transmission electron microscopy
STF = solar-to-fuel
STH = solar-to-hydrogen
Sty = styrene
StyCF_3 = 4-trifluoromethylstyrene
τ = minority carrier average lifetime
T = temperature
TAPS = N-[tris(hydroxymethyl)methyl]-3-aminopropanesulfonic acid
$TBAPF_6$ = tetrabutylammonium hexafluorophosphate
TEA = triethylamine
TEOA = triethanolamine
TEM = transmission electron microscopy
TFA = trifluoroacetic acid
THF = tetrahydrofuran
TOF = turnover frequency
TOF-SIMS = time-of-flight secondary ion mass spectrometry
TOF_{max} = maximum turnover frequency
TON = turnover number
TR-SPV = time-resolved surface photovoltage
TsOH = tosylic acid
t = time
v = velocity or rate of an enzymatic reaction
UV−vis = ultraviolet−visible
ϕ_B = barrier height
Φ_{abs} = probability of photon absorption
Φ_{inj} = probability of charge injection across a semiconductor junction
Φ_{sep} = probability of charge separation
φ = work function
V = applied potential
V_b = bias potential
V_{bi} = built-in voltage or potential
$V_{flatband}$ = flatband potential
V_{max} = maximum reaction velocity of an enzymatic reaction
V_{oc} = open-circuit potential
V_{onset} = onset potential
V_{ph} = photovoltage
W = width of the space-charge region
XANES = X-ray absorption near edge structure spectroscopy
XAS = X-ray absorption spectroscopy
XPS = X-ray photoelectron spectroscopy
XRD = X-ray powder diffraction

REFERENCES

(1) Lewis, N. S.; Nocera, D. G. Powering the planet: Chemical challenges in solar energy utilization. *Proc. Natl. Acad. Sci. U. S. A.* **2006**, *103*, 15729−15735.

(2) Gust, D.; Moore, T. A.; Moore, A. L. Solar Fuels via Artificial Photosynthesis. *Acc. Chem. Res.* **2009**, *42*, 1890−1898.

(3) Listorti, A.; Durrant, J.; Barber, J. Artificial photosynthesis: Solar to fuel. *Nat. Mater.* **2009**, *8*, 929−930.

(4) Faunce, T.; Styring, S.; Wasielewski, M. R.; Brudvig, G. W.; Rutherford, A. W.; Messinger, J.; Lee, A. F.; Hill, C. L.; Degroot, H.; Fontecave, M.; et al. Artificial photosynthesis as a frontier technology for energy sustainability. *Energy Environ. Sci.* **2013**, *6*, 1074−1076.

(5) Faunce, T. A.; Lubitz, W.; Rutherford, A. W.; MacFarlane, D.; Moore, G. F.; Yang, P.; Nocera, D. G.; Moore, T. A.; Gregory, D. H.; Fukuzumi, S.; et al. Energy and environment policy case for a global project on artificial photosynthesis. *Energy Environ. Sci.* **2013**, *6*, 695−698.

(6) Ardo, S.; Fernandez Rivas, D.; Modestino, M. A.; Schulze Greiving, V.; Abdi, F. F.; Alarcon Llado, E.; Artero, V.; Ayers, K.; Battaglia, C.; Becker, J. P.; et al. Pathways to electrochemical solar-hydrogen technologies. *Energy Environ. Sci.* **2018**, *11*, 2768−2783.

(7) Archer, M. D.; Barber, J. *Series on Photoconversion of Solar Energy, Vol. 2: Molecular to Global Photosynthesis*; Imperial College Press: London, 2004.

(8) 120 TW net primary production.

(9) Blankenship, R. E.; Tiede, D. M.; Barber, J.; Brudvig, G. W.; Fleming, G.; Ghirardi, M.; Gunner, M. R.; Junge, W.; Kramer, D. M.; Melis, A.; et al. Comparing Photosynthetic and Photovoltaic Efficiencies and Recognizing the Potential for Improvement. *Science* **2011**, *332*, 805−809.

(10) Fischer, W. W.; Hemp, J.; Johnson, J. E. Evolution of Oxygenic Photosynthesis. *Annu. Rev. Earth Planet. Sci.* **2016**, *44*, 647−683.

(11) Gust, D.; Kramer, D.; Moore, A.; Moore, T. A.; Vermaas, W. Engineered and Artificial Photosynthesis: Human Ingenuity Enters the Game. *MRS Bull.* **2008**, *33*, 383−387.

(12) Faunce, T. Global Artificial Photosynthesis and Renewable Energy Storage and Policy for the Sustainocene. *Adv. Sustain. Syst.* **2018**, *2*, 1800035.

(13) Tumas, B.; Dempsey, J. L.; Mallouk, T. E. *Basic Energy Sciences Roundtable on Liquid Solar Fuels*; U.S. Department of Energy, 2019.

(14) Thorp, H. H. Do us a favor. *Science* **2020**, *367*, 1169.

(15) Hemminger, J.; Fleming, G.; Ratner, M. *Directing Matter and Energy: Five Challenges for Science and the Imagination*; U.S. Department of Energy, **2007**. DOI: 10.2172/935427

(16) Rutherford, A. W.; Moore, T. A. Mimicking photosynthesis, but just the best bits. *Nature* **2008**, *453*, 449.

(17) 120,000 TW Power of the Sun.

(18) Hambourger, M.; Moore, G. F.; Kramer, D. M.; Gust, D.; Moore, A. L.; Moore, T. A. Biology and technology for photochemical fuel production. *Chem. Soc. Rev.* **2009**, *38*, 165−184.

(19) Zhang, B.; Sun, L. Artificial photosynthesis: opportunities and challenges of molecular catalysts. *Chem. Soc. Rev.* **2019**, *48*, 2216−2264.

(20) Dalle, K. E.; Warnan, J.; Leung, J. J.; Reuillard, B.; Karmel, I. S.; Reisner, E. Electro- and Solar-Driven Fuel Synthesis with First Row Transition Metal Complexes. *Chem. Rev.* **2019**, *119*, 2752−2875.

(21) Molecular-modified photoanodes are out of the scope of this work but have been reviewed elsewhere.[22−25]

(22) Wang, M.; Yang, Y.; Shen, J.; Jiang, J.; Sun, L. Visible-light-absorbing semiconductor/molecular catalyst hybrid photoelectrodes for H_2 or O_2 evolution: recent advances and challenges. *Sustain. Energy Fuels* **2017**, *1*, 1641−1663.

(23) Liang, X.; Cao, X.; Sun, W.; Ding, Y. Recent Progress in Visible Light Driven Water Oxidation Using Semiconductors Coupled with Molecular Catalysts. *ChemCatChem* **2019**, *11*, 6190−6202.

(24) Niu, F.; Wang, D.; Li, F.; Liu, Y.; Shen, S.; Meyer, T. J. Hybrid Photoelectrochemical Water Splitting Systems: From Interface Design to System Assembly. *Adv. Energy Mater.* **2020**, *10*, 1900399.

(25) Liu, H.-Y.; Cody, C. C.; Jacob-Dolan, J. A.; Crabtree, R. H.; Brudvig, G. W. Surface-Attached Molecular Catalysts on Visible-Light-Absorbing Semiconductors: Opportunities and Challenges for a Stable Hybrid Water-Splitting Photoanode. *ACS Energy Lett.* **2020**, *5*, 3195−3202.

(26) Brown, K. A.; Wilker, M. B.; Boehm, M.; Dukovic, G.; King, P. W. Characterization of Photochemical Processes for H_2 Production by CdS Nanorod-[FeFe] Hydrogenase Complexes. *J. Am. Chem. Soc.* **2012**, *134*, 5627−5636.

(27) Nellist, M. R.; Laskowski, F. A. L.; Lin, F.; Mills, T. J.; Boettcher, S. W. Semiconductor-Electrocatalyst Interfaces: Theory, Experiment, and Applications in Photoelectrochemical Water Splitting. *Acc. Chem. Res.* **2016**, *49*, 733−740.

(28) Chen, H. Y.; Ardo, S. Direct observation of sequential oxidations of a titania-bound molecular proxy catalyst generated through illumination of molecular sensitizers. *Nat. Chem.* **2018**, *10*, 17−23.

(29) He, Y.; Hamann, T.; Wang, D. Thin film photoelectrodes for solar water splitting. *Chem. Soc. Rev.* **2019**, *48*, 2182−2215.

(30) Wadsworth, B. L.; Khusnutdinova, D.; Urbine, J. M.; Reyes, A. S.; Moore, G. F. Expanding the Redox Range of Surface-Immobilized Metallocomplexes Using Molecular Interfaces. *ACS Appl. Mater. Interfaces* **2020**, *12*, 3903−3911.

(31) McKone, J. R.; Marinescu, S. C.; Brunschwig, B. S.; Winkler, J. R.; Gray, H. B. Earth-abundant hydrogen evolution electrocatalysts. *Chem. Sci.* **2014**, *5*, 865−878.

(32) Cedeno, D.; Krawicz, A.; Moore, G. F. Hybrid photocathodes for solar fuel production: coupling molecular fuelproduction catalysts with solid-state light harvesting and conversion technologies. *Interface Focus* **2015**, *5*, 1−6.

(33) Thorarinsdottir, A. E.; Nocera, D. G. Energy catalysis needs ligands with high oxidative stability. *Chem Catal.* **2021**, *1*, 32−43.

(34) Sun, J.; Zhong, D. K.; Gamelin, D. R. Composite photoanodes for photoelectrochemical solar water splitting. *Energy Environ. Sci.* **2010**, *3*, 1252−1261.

(35) Hisatomi, T.; Kubota, J.; Domen, K. Recent advances in semiconductors for photocatalytic and photoelectrochemical water splitting. *Chem. Soc. Rev.* **2014**, *43*, 7520−7535.

(36) Verhoeven, J. W. Glossary of terms used in photochemistry. *Pure Appl. Chem.* **1996**, *68*, 2223−2286.

(37) McNaught, A. D.; Wilkinson, A. IUPAC - photochemistry (P04588). *IUPAC Gold Book* **1997**, 1 DOI: 10.1351/goldbook.P04588.

(38) Bard, A. J. Photoelectrochemistry and heterogeneous photocatalysis at semiconductors. *J. Photochem.* **1979**, *10*, 59−75.

(39) Bard, A. J.; Memming, R.; Miller, B. Terminology in semiconductor electrochemistry and photoelectrochemical energy conversion. *Pure Appl. Chem.* **1991**, *63*, 569−596.

(40) Nielander, A. C.; Shaner, M. R.; Papadantonakis, K. M.; Francis, S. A.; Lewis, N. S. A taxonomy for solar fuels generators. *Energy Environ. Sci.* **2015**, *8*, 16−25.

(41) Dye-sensitized photoelectrosynthesis cells (DSPECs) are another type of excitonic chemical conversion system that integrates high bandgap, nanoparticle oxide semiconductors with the light-absorbing and catalytic properties of designed chromophore-catalyst. Although DSPECs are another type of PEC systems,[40] the focus of this review is on systems where the semiconductor absorbs the light to create excitons.

(42) Osterloh, F. E. Photocatalysis versus Photosynthesis: A Sensitivity Analysis of Devices for Solar Energy Conversion and Chemical Transformations. *ACS Energy Lett.* **2017**, *2*, 445−453.

(43) Nozik, A. J. Photochemical diodes. *Appl. Phys. Lett.* **1977**, *30*, 567−569.

(44) Surendranath, Y.; Bediako, D. K.; Nocera, D. G. Interplay of oxygen-evolution kinetics and photovoltaic power curves on the construction of artificial leaves. *Proc. Natl. Acad. Sci. U. S. A.* **2012**, *109*, 15617−15621.

(45) Singh, M. R.; Clark, E. L.; Bell, A. T. Thermodynamic and achievable efficiencies for solar-driven electrochemical reduction of carbon dioxide to transportation fuels. *Proc. Natl. Acad. Sci. U. S. A.* **2015**, *112*, E6111−E6118.

(46) Chen, Z.; Jaramillo, T. F.; Deutsch, T. G.; Kleiman-Shwarsctein, A.; Forman, A. J.; Gaillard, N.; Garland, R.; Takanabe, K.; Heske, C.; Sunkara, M.; et al. Accelerating materials development for photoelectrochemical hydrogen production: Standards for methods, definitions, and reporting protocols. *J. Mater. Res.* **2010**, *25*, 3−16.

(47) The air mass 1.5 global tilt (AM 1.5 G) spectrum from the ASTM G-173−03 data set is available online at https://www.nrel.gov/grid/solar-resource/spectra.html.

(48) Costentin, C.; Drouet, S.; Robert, M.; Savéant, J.-M. Turnover Numbers, Turnover Frequencies, and Overpotential in Molecular Catalysis of Electrochemical Reactions. Cyclic Voltammetry and Preparative-Scale Electrolysis. *J. Am. Chem. Soc.* **2012**, *134*, 11235−11242.

(49) Costentin, C.; Savéant, J.-M. Multielectron, Multistep Molecular Catalysis of Electrochemical Reactions: Benchmarking of Homogeneous Catalysts. *ChemElectroChem* **2014**, *1*, 1226−1236.

(50) Kinetics associated with the multielectron, multistep molecular catalytic processes where the catalysts are present in the solution have been described elsewhere.[48]

(51) Dotan, H.; Mathews, N.; Hisatomi, T.; Grätzel, M.; Rothschild, A. On the Solar to Hydrogen Conversion Efficiency of Photoelectrodes for Water Splitting. *J. Phys. Chem. Lett.* **2014**, *5*, 3330−3334.

(52) Hammarström, L.; Winkler, J. R.; Gray, H. B.; Styring, S. Shedding Light on Solar Fuel Efficiencies. *Science* **2011**, *333*, 288.

(53) Green, B. R.; Parson, W. W. *Advances in Photosynthesis and Respiration, Vol. 13: Light-Harvesting antennas in Photosynthesis*, 1st ed.; Springer Netherlands: Dordrecht, 2003.

(54) Moore, G. F.; Brudvig, G. W. Energy Conversion in Photosynthesis: A Paradigm for Solar Fuel Production. *Annu. Rev. Condens. Matter Phys.* **2011**, *2*, 303−327.

(55) Blankenship, R. E. *Molecular Mechanisms of Photosynthesis*, 3rd ed.; Wiley-Blackwell: Oxford, 2021.

(56) Long, S. P.; Humphries, S.; et al. Photoinhibition of Photosynthesis in Nature. *Annu. Rev. Plant Physiol. Plant Mol. Biol.* **1994**, *45*, 633−662.

(57) Goh, C. H.; Ko, S. M.; Koh, S.; Kim, Y. J.; Bae, H. J. Photosynthesis and Environments: Photoinhibition and Repair Mechanisms in Plants. *J. Plant Biol.* **2012**, *55*, 93−101.

(58) Durrant, J. R.; Giorgi, L. B.; Barber, J.; Klug, D. R.; Porter, G. Characterisation of triplet states in isolated Photosystem II reaction centres: Oxygen quenching as a mechanism for photodamage. *BBA - Bioenerg.* **1990**, *1017*, 167−175.

(59) Guergova-Kuras, M.; Boudreaux, B.; Joliot, A.; Joliot, P.; Redding, K. Evidence for two active branches for electron transfer in photosystem I. *Proc. Natl. Acad. Sci. U. S. A.* **2001**, *98*, 4437−4442.

(60) Marcus, R. A.; Sutin, N. Electron transfers in chemistry and biology. *Biochim. Biophys. Acta* **1985**, *811*, 265−322.

(61) Moser, C. C.; Keske, J. M.; Warncke, K.; Farid, R. S.; Dutton, P. L. Nature of biological electron transfer. *Nature* **1992**, *355*, 796−802.

(62) Gray, H. B.; Winkler, J. R. Electron Transfer in Proteins. *Annu. Rev. Biochem.* **1996**, *65*, 537−561.

(63) Bard, A. J.; Faulkner, L. R. *Electrochemical Methods: Fundamentals of Applications*, 2nd ed.; Wiley & Sons: New York, 2001.

(64) Savéant, J.-M.; Costentin, C. *Elements of Molecular and Biomolecular Electrochemistry: An Electrochemical Approach to Electron Transfer Chemistry*, 2nd ed.; Wiley & Sons: Hoboken, 2019.

(65) Ruben, S.; Randall, M.; Kamen, M.; Hyde, J. L. Heavy Oxygen (O^{18}) as a Tracer in the Study of Photosynthesis. *J. Am. Chem. Soc.* **1941**, *63*, 877−879.

(66) Gontero, B.; Lebreton, S.; Graciet, E. *Annual Plant Reviews, Volume 7: Protein-Protein Interactions in Plant Biology*; Sheffield Academic Press: Sheffield, 2002; p 125−157.

(67) Raines, C. A. The Calvin cycle revisited. *Photosynth. Res.* **2003**, *75*, 1−10.

(68) Mitchell, P. Coupling of phosphorylation to electron and hydrogen transfer by a chemi-osmotic type of mechanism. *Nature* **1961**, *191*, 144−148.

(69) Mitchell, P. Chemiosmotic coupling in oxidative and photosynthetic phosphorylation. *Biochim. Biophys. Acta - Bioenerg.* **2011**, *1807*, 1507−1538.

(70) Martin, J. L.; Ishmukhametov, R.; Hornung, T.; Ahmad, Z.; Frasch, W. D. Anatomy of F_1-ATPase powered rotation. *Proc. Natl. Acad. Sci. U. S. A.* **2014**, *111*, 3715−3720.

(71) Junge, W.; Nelson, N. ATP synthase. *Annu. Rev. Biochem.* **2015**, *84*, 631−657.

(72) Cukier, R. I.; Nocera, D. G. Proton-coupled electron transfer. *Annu. Rev. Phys. Chem.* **1998**, *49*, 337−369.

(73) Mayer, J. M. Proton-Coupled Electron Transfer: A Reaction Chemist's View. *Annu. Rev. Phys. Chem.* **2004**, *55*, 363−390.

(74) Huynh, M. H. V.; Meyer, T. J. Proton-coupled electron transfer. *Chem. Rev.* **2007**, *107*, 5004−5064.

(75) Hammarström, L.; Styring, S. Coupled electron transfers in artificial photosynthesis. *Philos. Trans. R. Soc. B Biol. Sci.* **2008**, *363*, 1283−1291.

(76) Hammes-Schiffer, S. Theory of Proton-Coupled Electron Transfer in Energy Conversion Processes. *Acc. Chem. Res.* **2009**, *42*, 1881−1889.

(77) Dempsey, J. L.; Winkler, J. R.; Gray, H. B. Proton-coupled electron flow in protein redox machines. *Chem. Rev.* **2010**, *110*, 7024−7039.

(78) Hammarström, L.; Styring, S. Proton-coupled electron transfer of tyrosines in Photosystem II and model systems for artificial photosynthesis: the role of a redox-active link between catalyst and photosensitizer. *Energy Environ. Sci.* **2011**, *4*, 2379−2388.

(79) Weinberg, D. R.; Gagliardi, C. J.; Hull, J. F.; Murphy, C. F.; Kent, C. A.; Westlake, B. C.; Paul, A.; Ess, D. H.; McCafferty, D. G.; Meyer, T. J. Proton-Coupled Electron Transfer. *Chem. Rev.* **2012**, *112*, 4016−4093.

(80) Hammes-Schiffer, S. Proton-Coupled Electron Transfer: Moving Together and Charging Forward. *J. Am. Chem. Soc.* **2015**, *137*, 8860−8871.

(81) Mora, S. J.; Odella, E.; Moore, G. F.; Gust, D.; Moore, T. A.; Moore, A. L. Proton-Coupled Electron Transfer in Artificial Photosynthetic Systems. *Acc. Chem. Res.* **2018**, *51*, 445−453.

(82) Berardi, S.; Drouet, S.; Francàs, L.; Gimbert-Suriñach, C.; Guttentag, M.; Richmond, C.; Stoll, T.; Llobet, A. Molecular artificial photosynthesis. *Chem. Soc. Rev.* **2014**, *43*, 7501−7519.

(83) Hammarström, L. Accumulative Charge Separation for Solar Fuels Production: Coupling Light-Induced Single Electron Transfer to Multielectron Catalysis. *Acc. Chem. Res.* **2015**, *48*, 840−850.

(84) Lindley, B. M.; Appel, A. M.; Krogh-Jespersen, K.; Mayer, J. M.; Miller, A. J. M. Evaluating the Thermodynamics of Electrocatalytic N_2 Reduction in Acetonitrile. *ACS Energy Lett.* **2016**, *1*, 698−704.

(85) Li, H.; Li, J.; Ai, Z.; Jia, F.; Zhang, L. Oxygen Vacancy-Mediated Photocatalysis of BiOCl: Reactivity, Selectivity, and Perspectives. *Angew. Chem., Int. Ed.* **2018**, *57*, 122−138.

(86) Beiler, A. M.; Moore, G. F. Multi-electron-Transfer Photochemistry: Caught in the act. *Nat. Chem.* **2018**, *10*, 3−4.

(87) Chen, X.; Li, N.; Kong, Z.; Ong, W. J.; Zhao, X. Photocatalytic fixation of nitrogen to ammonia: state-of-the-art advancements and future prospects. *Mater. Horizons* **2018**, *5*, 9−27.

(88) Woodrow, I. E.; et al. Enzymatic regulation photosynthetic CO_2 fixation in C_3 plants. *Annu. Rev. Plant Physiol. Plant Mol. Biol.* **1988**, *39*, 533−594.

(89) Evans, D. J.; Pickett, C. J. Chemistry and the hydrogenases. *Chem. Soc. Rev.* **2003**, *32*, 268−275.

(90) Bachmeier, A.; Armstrong, F. A. Solar-driven proton and carbon dioxide reduction to fuels - lessons from metalloenzymes. *Curr. Opin. Chem. Biol.* **2015**, *25*, 141−151.

(91) Del Barrio, M.; Sensi, M.; Orain, C.; Baffert, C.; Dementin, S.; Fourmond, V.; Léger, C. Electrochemical Investigations of Hydrogenases and Other Enzymes That Produce and Use Solar Fuels. *Acc. Chem. Res.* **2018**, *51*, 769−777.

(92) Evans, R. M.; Siritanaratkul, B.; Megarity, C. F.; Pandey, K.; Esterle, T. F.; Badiani, S.; Armstrong, F. A. The value of enzymes in solar fuels research - efficient electrocatalysts through evolution. *Chem. Soc. Rev.* **2019**, *48*, 2039−2052.

(93) Cracknell, J. A.; Vincent, K. A.; Armstrong, F. A. Enzymes as Working or Inspirational Electrocatalysts for Fuel Cells and Electrolysis. *Chem. Rev.* **2008**, *108*, 2439−2461.

(94) Armstrong, F. A.; Hirst, J. Reversibility and efficiency in electrocatalytic energy conversion and lessons from enzymes. *Proc. Natl. Acad. Sci. U. S. A.* **2011**, *108*, 14049−14054.

(95) Shaw, W. J. The outer-Coordination Sphere: Incorporating Amino Acids and Peptides as Ligands for Homogeneous Catalysts to Mimic Enzyme Function. *Catal. Rev. Sci. Eng.* **2012**, *54*, 489−550.

(96) Zhao, M.; Wang, H. B.; Ji, L. N.; Mao, Z. W. Insights into metalloenzyme microenvironments: biomimetic metal complexes with a functional second coordination sphere. *Chem. Soc. Rev.* **2013**, *42*, 8360−8375.

(97) Gunner, M. R.; Honig, B. Electrostatic control of midpoint potentials in the cytochrome subunit of the *Rhodopseudomonas viridis* reaction center. *Proc. Natl. Acad. Sci. U. S. A.* **1991**, *88*, 9151−9155.

(98) Mao, J.; Hauser, K.; Gunner, M. R. How Cytochromes with Different Folds Control Heme Redox Potentials. *Biochemistry* **2003**, *42*, 9829−9840.

(99) Gray, H. B.; Stiefel, E. I.; Valentine, J. S.; Bertini, I. *Biological Inorganic Chemistry Structure and Reactivity*, 1st ed.; University Science Books, 2007.

(100) Zheng, Z.; Gunner, M. R. Analysis of the electrochemistry of hemes with E_ms spanning 800 mV. *Proteins Struct. Funct. Bioinforma.* **2009**, *75*, 719−734.

(101) Liu, J.; Chakraborty, S.; Hosseinzadeh, P.; Yu, Y.; Tian, S.; Petrik, I.; Bhagi, A.; Lu, Y. Metalloproteins Containing Cytochrome, Iron-Sulfur, or Copper Redox Centers. *Chem. Rev.* **2014**, *114*, 4366−4369.

(102) Zamost, B. L.; Nielsen, H. K.; Starnes, R. L. Thermostable enzymes for industrial applications. *J. Ind. Microbiol.* **1991**, *8*, 71−81.

(103) Tye, J. W.; Hall, M. B.; Darensbourg, M. Y. Better than platinum? Fuel cells energized by enzymes. *Proc. Natl. Acad. Sci. U. S. A.* **2005**, *102*, 16911−16912.

(104) Meredith, M. T.; Minteer, S. D. Biofuel cells: Enhanced enzymatic bioelectrocatalysis. *Annu. Rev. Anal. Chem.* **2012**, *5*, 157−179.

(105) Woolerton, T. W.; Sheard, S.; Chaudhary, Y. S.; Armstrong, F. A. Enzymes and bio-inspired electrocatalysts in solar fuel devices. *Energy Environ. Sci.* **2012**, *5*, 7470−7490.

(106) Liese, A.; Hilterhaus, L. Evaluation of immobilized enzymes for industrial applications. *Chem. Soc. Rev.* **2013**, *42*, 6236−6249.

(107) Rasmussen, M.; Abdellaoui, S.; Minteer, S. D. Enzymatic biofuel cells: 30 years of critical advancements. *Biosens. Bioelectron.* **2016**, *76*, 91−102.

(108) Porter, J. L.; Rusli, R. A.; Ollis, D. L. Directed Evolution of Enzymes for Industrial Biocatalysis. *ChemBioChem* **2016**, *17*, 197−203.

(109) Frey, M. Hydrogenases: Hydrogen-Activating Enzymes. *ChemBioChem* **2002**, *3*, 153−160.

(110) Cammack, R. Hydrogenase sophistication. *Nature* **1999**, *397*, 214−215.

(111) Lee, C. Y.; Park, H. S.; Fontecilla-Camps, J. C.; Reisner, E. Photoelectrochemical H_2 Evolution with a Hydrogenase Immobilized on a TiO_2-Protected Silicon Electrode. *Angew. Chem., Int. Ed.* **2016**, *55*, 5971−5974.

(112) Alfonta, L.; Zhang, Z.; Uryu, S.; Loo, J. A.; Schultz, P. G. Site-Specific Incorporation of a Redox-Active Amino Acid into Proteins. *J. Am. Chem. Soc.* **2003**, *125*, 14662−14663.

(113) Landwehr, M.; Carbone, M.; Otey, C. R.; Li, Y.; Arnold, F. H. Diversification of Catalytic Function in a Synthetic Family of Chimeric Cytochrome P450s. *Chem. Biol.* **2007**, *14*, 269−278.

(114) Nocera, D. G. Solar Fuels and Solar Chemicals Industry. *Acc. Chem. Res.* **2017**, *50*, 616−619.

(115) Jones, A. K.; Lichtenstein, B. R.; Dutta, A.; Gordon, G.; Dutton, P. L. Synthetic Hydrogenases: Incorporation of an Iron Carbonyl Thiolate into a Designed Peptide. *J. Am. Chem. Soc.* **2007**, *129*, 14844−14845.

(116) Ugwumba, I. N.; Ozawa, K.; Xu, Z. Q.; Ely, F.; Foo, J. L.; Herlt, A. J.; Coppin, C.; Brown, S.; Taylor, M. C.; Ollis, D. L.; et al. Improving a Natural Enzyme Activity through Incorporation of Unnatural Amino Acids. *J. Am. Chem. Soc.* **2011**, *133*, 326−333.

(117) Dong, Z.; Luo, Q.; Liu, J. Artificial enzymes based on supramolecular scaffolds. *Chem. Soc. Rev.* **2012**, *41*, 7890−7908.

(118) Faiella, M.; Roy, A.; Sommer, D.; Ghirlanda, G. De Novo Design of Functional Proteins: Toward Artificial Hydrogenases. *Biopolymers* **2013**, *100*, 558−571.

(119) Roy, S.; Nguyen, T. A. D.; Gan, L.; Jones, A. K. Biomimetic peptide-based models of [FeFe]-hydrogenases: Utilization of phosphine-containing peptides. *Dalt. Trans.* **2015**, *44*, 14865−14876.

(120) Mak, W. S.; Tran, S.; Marcheschi, R.; Bertolani, S.; Thompson, J.; Baker, D.; Liao, J. C.; Siegel, J. B. Integrative genomic mining for enzyme function to enable engineering of a non-natural biosynthetic pathway. *Nat. Commun.* **2015**, *6*, 1−9.

(121) Alcala-Torano, R.; Sommer, D. J.; Bahrami Dizicheh, Z.; Ghirlanda, G. *Methods in Enzymology, Volume 580: Peptide, Protein and Enzyme Design*; Academic Press: Cambridge, 2016; p 389−416.

(122) Sakimoto, K. K.; Kornienko, N.; Yang, P. Cyborgian Material Design for Solar Fuel Production: The Emerging Photosynthetic Biohybrid Systems. *Acc. Chem. Res.* **2017**, *50*, 476−481.

(123) Berggren, G.; Adamska, A.; Lambertz, C.; Simmons, T. R.; Esselborn, J.; Atta, M.; Gambarelli, S.; Mouesca, J. M.; Reijerse, E.; Lubitz, W.; et al. Biomimetic assembly and activation of [FeFe]-hydrogenases. *Nature* **2013**, *499*, 66−69.

(124) Slater, J. W.; Marguet, S. C.; Monaco, H. A.; Shafaat, H. S. Going beyond Structure: Nickel-Substituted Rubredoxin as a Mechanistic Model for the [NiFe] Hydrogenases. *J. Am. Chem. Soc.* **2018**, *140*, 10250−10262.

(125) Helm, M. L.; Stewart, M. P.; Bullock, R. M.; Dubois, M. R.; Dubois, D. L. A Synthetic Nickel Electrocatalyst with a Turnover Frequency Above 100,000 s^{-1} for H_2 Production. *Science* **2011**, *333*, 863−866.

(126) Gross, M. A.; Reynal, A.; Durrant, J. R.; Reisner, E. Versatile Photocatalytic Systems for H_2 Generation in Water Based on an Efficient DuBois-Type Nickel Catalyst. *J. Am. Chem. Soc.* **2014**, *136*, 356−366.

(127) Das, A. K.; Engelhard, M. H.; Bullock, R. M.; Roberts, J. A. S. A Hydrogen-Evolving $Ni(P_2N_2)_2$ Electrocatalyst Covalently Attached to a Glassy Carbon Electrode: Preparation, Characterization, and Catalysis. Comparisons with the Homogeneous Analogue. *Inorg. Chem.* **2014**, *53*, 6875−6885.

(128) Leung, J. J.; Warnan, J.; Nam, D. H.; Zhang, J. Z.; Willkomm, J.; Reisner, E. Photoelectrocatalytic H_2 evolution in water with molecular catalysts immobilised on p-Si *via* a stabilising mesoporous TiO_2 interlayer. *Chem. Sci.* **2017**, *8*, 5172−5180.

(129) Jain, A.; Lense, S.; Linehan, J. C.; Raugei, S.; Cho, H.; Dubois, D. L.; Shaw, W. J. Incorporating Peptides in the Outer-Coordination Sphere of Bioinspired Electrocatalysts for Hydrogen Production. *Inorg. Chem.* **2011**, *50*, 4073−4085.

(130) Jain, A.; Reback, M. L.; Lindstrom, M. L.; Thogerson, C. E.; Helm, M. L.; Appel, A. M.; Shaw, W. J. Investigating the Role of the Outer-Coordination Sphere in $[Ni(P^{Ph}{}_2N^{Ph\text{-}R}{}_2)_2]^{2+}$ Hydrogenase Mimics. *Inorg. Chem.* **2012**, *51*, 6592−6602.

(131) Reback, M. L.; Ginovska-Pangovska, B.; Ho, M. H.; Jain, A.; Squier, T. C.; Raugei, S.; Roberts, J. A. S.; Shaw, W. J. The Role of a Dipeptide Outer-Coordination Sphere on H_2-Production Catalysts: Influence on Catalytic Rates and Electron Transfer. *Chem. Eur. J.* **2013**, *19*, 1928−1941.

(132) Ginovska-Pangovska, B.; Dutta, A.; Reback, M. L.; Linehan, J. C.; Shaw, W. J. Beyond the Active Site: The Impact of the Outer Coordination Sphere on Electrocatalysts for Hydrogen Production and Oxidation. *Acc. Chem. Res.* **2014**, *47*, 2621−2630.

(133) Gust, D.; Moore, T. A.; Makings, L. R.; Liddell, P. A.; Nemeth, G. A.; Moore, A. L. Photodriven Electron Transfer in Triad Molecules: A Two-Step Charge Recombination Reaction. *J. Am. Chem. Soc.* **1986**, *108*, 8028−8031.

(134) Yang, J.; Yoon, M. C.; Yoo, H.; Kim, P.; Kim, D. Excitation energy transfer in multiporphyrin arrays with cyclic architectures: Towards artificial light-harvesting antenna complexes. *Chem. Soc. Rev.* **2012**, *41*, 4808−4826.

(135) Rudolf, M.; Kirner, S. V.; Guldi, D. M. A multicomponent molecular approach to artificial photosynthesis - the role of fullerenes and endohedral metallofullerenes. *Chem. Soc. Rev.* **2016**, *45*, 612−630.

(136) Kosco, J.; Moruzzi, F.; Willner, B.; McCulloch, I. Photocatalysts Based on Organic Semiconductors with Tunable Energy Levels for Solar Fuel Applications. *Adv. Energy Mater.* **2020**, *10*, 2001935.

(137) Cheng, Y.-Z.; Ding, X.; Han, B.-H. Porous Organic Polymers for Photocatalytic Carbon Dioxide Reduction. *ChemPhotoChem* **2021**, *5*, 406−417.

(138) Zhao, Z.; Zhan, S.; Feng, L.; Liu, C.; Ahlquist, M. S. G.; Wu, X.; Fan, K.; Li, F.; Sun, L. Molecular Engineering of Photocathodes based on Polythiophene Organic Semiconductors for Photoelectrochemical Hydrogen Generation. *ACS Appl. Mater. Interfaces* **2021**, *13*, 40602−40611.

(139) Wasielewski, M. R. Photoinduced Electron Transfer in Supramolecular Systems for Artificial Photosynthesis. *Chem. Rev.* **1992**, *92*, 435−461.

(140) Gust, D.; Moore, T. A.; Moore, A. L. Molecular Mimicry of Photosynthetic Energy and Electron Transfer. *Acc. Chem. Res.* **1993**, *26*, 198−205.

(141) Gust, D.; Moore, T. A.; Moore, A. L. Mimicking Photosynthetic Solar Energy Transduction. *Acc. Chem. Res.* **2001**, *34*, 40−48.

(142) Guldi, D. M. Fullerene-porphyrin architectures; photosynthetic antenna and reaction center models. *Chem. Soc. Rev.* **2002**, *31*, 22−36.

(143) Alstrum-Acevedo, J. H.; Brennaman, M. K.; Meyer, T. J. Chemical Approaches to Artificial Photosynthesis. 2. *Inorg. Chem.* **2005**, *44*, 6802−6827.

(144) Nakamura, Y.; Aratani, N.; Osuka, A. Cyclic porphyrin arrays as artificial photosynthetic antenna: synthesis and excitation energy transfer. *Chem. Soc. Rev.* **2007**, *36*, 831−845.

(145) Wasielewski, M. R. Self-Assembly Strategies for Integrating Light Harvesting and Charge Separation in Artificial Photosynthetic Systems. *Acc. Chem. Res.* **2009**, *42*, 1910−1921.

(146) McConnell, I.; Li, G.; Brudvig, G. W. Energy conversion in natural and artificial photosynthesis. *Chem. Biol.* **2010**, *17*, 434−447.

(147) Grätzel, M. Dye-sensitized solar cells. *J. Photochem. Photobiol. C Photochem. Rev.* **2003**, *4*, 145−153.

(148) Moore, G. F.; Blakemore, J. D.; Milot, R. L.; Hull, J. F.; Song, H. E.; Cai, L.; Schmuttenmaer, C. A.; Crabtree, R. H.; Brudvig, G. W. A visible light water-splitting cell with a photoanode formed by codeposition of a high-potential porphyrin and an iridium water-oxidation catalyst. *Energy Environ. Sci.* **2011**, *4*, 2389−2392.

(149) Alibabaei, L.; Brennaman, M. K.; Norris, M. R.; Kalanyan, B.; Song, W.; Losego, M. D.; Concepcion, J. J.; Binstead, R. A.; Parsons, G. N.; Meyer, T. J. Solar water splitting in a molecular photoelectrochemical cell. *Proc. Natl. Acad. Sci. U. S. A.* **2013**, *110*, 20008−20013.

(150) Alibabaei, L.; Sherman, B. D.; Norris, M. R.; Brennaman, M. K.; Meyer, T. J. Visible photoelectrochemical water splitting into H_2 and O_2 in a dye-sensitized photoelectrosynthesis cell. *Proc. Natl. Acad. Sci. U. S. A.* **2015**, *112*, 5899−5902.

(151) Ashford, D. L.; Gish, M. K.; Vannucci, A. K.; Brennaman, M. K.; Templeton, J. L.; Papanikolas, J. M.; Meyer, T. J. Molecular Chromophore-Catalyst Assemblies for Solar Fuel Applications. *Chem. Rev.* **2015**, *115*, 13006−13049.

(152) Brennaman, M. K.; Dillon, R. J.; Alibabaei, L.; Gish, M. K.; Dares, C. J.; Ashford, D. L.; House, R. L.; Meyer, G. J.; Papanikolas, J. M.; Meyer, T. J. Finding the Way to Solar Fuels with Dye-Sensitized Photoelectrosynthesis Cells. *J. Am. Chem. Soc.* **2016**, *138*, 13085−13102.

(153) Xu, P.; McCool, N. S.; Mallouk, T. E. Water splitting dye-sensitized solar cells. *Nano Today* **2017**, *14*, 42−58.

(154) Dotan, H.; Sivula, K.; Grätzel, M.; Rothschild, A.; Warren, S. C. Probing the photoelectrochemical properties of hematite (α-Fe_2O_3) electrodes using hydrogen peroxide as a hole scavenger. *Energy Environ. Sci.* **2011**, *4*, 958−964.

(155) Trotochaud, L.; Mills, T. J.; Boettcher, S. W. An Optocatalytic Model for Semiconductor-Catalyst Water-Splitting Photoelectrodes Based on In Situ Optical Measurements on Operational Catalysts. *J. Phys. Chem. Lett.* **2013**, *4*, 931−935.

(156) Wadsworth, B. L.; Nguyen, N. P.; Nishiori, D.; Beiler, A. M.; Moore, G. F. Addressing the Origin of Photocurrents and Fuel Production Activities in Catalyst-Modified Semiconductor Electrodes. *ACS Appl. Energy Mater.* **2020**, *3*, 7512−7519.

(157) Garnett, E.; Yang, P. Light Trapping in Silicon Nanowire Solar Cells. *Nano Lett.* **2010**, *10*, 1082−1087.

(158) Liu, C.; Dasgupta, N. P.; Yang, P. Semiconductor Nanowires for Artificial Photosynthesis. *Chem. Mater.* **2014**, *26*, 415−422.

(159) Peter, L. M. Energetics and kinetics of light-driven oxygen evolution at semiconductor electrodes: the example of hematite. *J. Solid State Electrochem.* **2013**, *17*, 315−326.

(160) Walter, M. G.; Warren, E. L.; McKone, J. R.; Boettcher, S. W.; Mi, Q.; Santori, E. A.; Lewis, N. S. Solar Water Splitting Cells. *Chem. Rev.* **2010**, *110*, 6446−6473.

(161) Gutsche, C.; Niepelt, R.; Gnauck, M.; Lysov, A.; Prost, W.; Ronning, C.; Tegude, F. J. Direct determination of minority carrier diffusion lengths at axial GaAs nanowire p-n junctions. *Nano Lett.* **2012**, *12*, 1453−1458.

(162) Williams, F.; Nozik, A. J. Solid-state perspectives of the photoelectrochemistry of semiconductor-electrolyte junctions. *Nature* **1984**, *312*, 21−27.

(163) Lewis, N. S. Chemical Control of Charge Transfer and Recombination at Semiconductor Photoelectrode Surfaces. *Inorg. Chem.* **2005**, *44*, 6900−6911.

(164) Peter, L. M. Dynamic Aspects of Semiconductor Photoelectrochemistry. *Chem. Rev.* **1990**, *90*, 753−769.

(165) Memming, R. *Semiconductor Electrochemistry*; Wiley-VCH: Weinheim, 2015; p 169−266.

(166) Deng, J.; Su, Y.; Liu, D.; Yang, P.; Liu, B.; Liu, C. Nanowire Photoelectrochemistry. *Chem. Rev.* **2019**, *119*, 9221−9259.

(167) Joe, J.; Yang, H.; Bae, C.; Shin, H. Metal Chalcogenides on Silicon Photocathodes for Efficient Water Splitting: A Mini Overview. *Catalysts* **2019**, *9*, 1−37.

(168) Bard, A. J.; Bocarsly, A. B.; Fan, F. R. F.; Walton, E. G.; Wrighton, M. S. The Concept of Fermi Level Pinning at Semiconductor/Liquid Junctions. Consequences for Energy Conversion Efficiency and Selection of Useful Solution Redox Couples in Solar Devices. *J. Am. Chem. Soc.* **1980**, *102*, 3671−3677.

(169) For a nonideal semiconductor, the presence of surface states can introduce additional energy levels that pin the band edges relative to the Fermi level, affecting the maximum obtainable photovoltage.

(170) Lewis, N. S. An analysis of charge transfer rate constants for semiconductor/liquid interfaces. *Annu. Rev. Phys. Chem.* **1991**, *42*, 543−580.

(171) Gärtner, W. W. Depletion-Layer Photoeffects in Semiconductors. *Phys. Rev.* **1959**, *116*, 84−87.

(172) Reichman, J. The current-voltage characteristics of semiconductor-electrolyte junction photovoltaic cells. *Appl. Phys. Lett.* **1980**, *36*, 574−577.

(173) Lin, F.; Boettcher, S. W. Adaptive semiconductor/electrocatalyst junctions in water-splitting photoanodes. *Nat. Mater.* **2014**, *13*, 81−86.

(174) Hamann, T. W. Water splitting: An adaptive junction. *Nat. Mater.* **2014**, *13*, 3−4.

(175) Gerischer, H. The role of semiconductor structure and surface properties in photoelectrochemical processes. *J. Electroanal. Chem.* **1983**, *150*, 553−569.

(176) Gerischer, H. Electron-Transfer Kinetics of Redox Reactions at the Semiconductor/Electrolyte Contact. A New Approach. *J. Phys. Chem.* **1991**, *95*, 1356−1359.

(177) Nozik, A. J.; Memming, R. Physical Chemistry of Semiconductor-Liquid Interfaces. *J. Phys. Chem.* **1996**, *100*, 13061−13078.

(178) Sathrum, A. J.; Kubiak, C. P. Kinetics and Limiting Current Densities of Homogeneous and Heterogeneous Electrocatalysts. *J. Phys. Chem. Lett.* **2011**, *2*, 2372−2379.

(179) Mills, T. J.; Lin, F.; Boettcher, S. W. Theory and Simulations of Electrocatalyst-Coated Semiconductor Electrodes for Solar Water Splitting. *Phys. Rev. Lett.* **2014**, *112*, 148304.

(180) Le Formal, F.; Pastor, E.; Tilley, S. D.; Mesa, C. A.; Pendlebury, S. R.; Grätzel, M.; Durrant, J. R. Rate Law Analysis of Water Oxidation on a Hematite Surface. *J. Am. Chem. Soc.* **2015**, *137*, 6629−6637.

(181) Wadsworth, B. L.; Beiler, A. M.; Khusnutdinova, D.; Reyes Cruz, E. A.; Moore, G. F. Interplay between Light Flux, Quantum Efficiency, and Turnover Frequency in Molecular-Modified Photoelectrosynthetic Assemblies. *J. Am. Chem. Soc.* **2019**, *141*, 15932−15941.

(182) Gerischer, H. Charge transfer processes at semiconductor-electrolyte interfaces in connection with problems of catalysis. *Surf. Sci.* **1969**, *18*, 97−122.

(183) Gerischer, H. Electrochemical photo and solar cells principles and some experiments. *J. Electroanal. Chem.* **1975**, *58*, 263−274.

(184) Nozik, A. J. Photoelectrochemistry: Applications to solar energy conversion. *Annu. Rev. Phys. Chem.* **1978**, *29*, 189−222.

(185) Mueller-Westerhoff, U. T.; Nazzal, A. [1.1]Ferrocenophanes as Effective Catalysts in the Photoelectrochemical Hydrogen Evolution from Acidic Aqueous Media. *J. Am. Chem. Soc.* **1984**, *106*, 5381−5382.

(186) Wadsworth, B. L.; Khusnutdinova, D.; Moore, G. F. Polymeric coatings for applications in electrocatalytic and photoelectrosynthetic fuel production. *J. Mater. Chem. A* **2018**, *6*, 21654−21665.

(187) Nann, T.; Ibrahim, S. K.; Woi, P. M.; Xu, S.; Ziegler, J.; Pickett, C. J. Water Splitting by Visible Light: A Nanophotocathode for Hydrogen Production. *Angew. Chem., Int. Ed.* **2010**, *49*, 1574−1577.

(188) E vs RHE = E vs Ag/AgCl + 0.209 V + 0.059*pH.

(189) Hou, Y.; Abrams, B. L.; Vesborg, P. C. K.; Björketun, M. E.; Herbst, K.; Bech, L.; Setti, A. M.; Damsgaard, C. D.; Pedersen, T.; Hansen, O.; et al. Bioinspired molecular co-catalysts bonded to a silicon photocathode for solar hydrogen evolution. *Nat. Mater.* **2011**, *10*, 434−438.

(190) Moore, G. F.; Sharp, I. D. A Noble-Metal-Free Hydrogen Evolution Catalyst Grafted to Visible Light-Absorbing Semiconductors. *J. Phys. Chem. Lett.* **2013**, *4*, 568−572.

(191) Krawicz, A.; Yang, J.; Anzenberg, E.; Yano, J.; Sharp, I. D.; Moore, G. F. Photofunctional Construct That Interfaces Molecular Cobalt-Based Catalysts for H_2 Production to a Visible-Light-Absorbing Semiconductor. *J. Am. Chem. Soc.* **2013**, *135*, 11861−11868.

(192) Cedeno, D.; Krawicz, A.; Doak, P.; Yu, M.; Neaton, J. B.; Moore, G. F. Using Molecular Design to Control the Performance of Hydrogen-Producing Polymer-Brush-Modified Photocathodes. *J. Phys. Chem. Lett.* **2014**, *5*, 3222−3226.

(193) Du, P.; Knowles, K.; Eisenberg, R. A Homogeneous System for the Photogeneration of Hydrogen from Water Based on a Platinum(II) Terpyridyl Acetylide Chromophore and a Molecular Cobalt Catalyst. *J. Am. Chem. Soc.* **2008**, *130*, 12576−12577.

(194) Berben, L. A.; Peters, J. C. Hydrogen evolution by cobalt tetraimine catalysts adsorbed on electrode surfaces. *Chem. Commun.* **2010**, *46*, 398−400.

(195) Beiler, A. M.; Khusnutdinova, D.; Jacob, S. I.; Moore, G. F. Chemistry at the Interface: Polymer-Functionalized GaP Semiconductors for Solar Hydrogen Production. *Ind. Eng. Chem. Res.* **2016**, *55*, 5306−5314.

(196) Beiler, A. M.; Khusnutdinova, D.; Jacob, S. I.; Moore, G. F. Solar Hydrogen Production Using Molecular Catalysts Immobilized on Gallium Phosphide (111)A and (111)B Polymer-Modified Photocathodes. *ACS Appl. Mater. Interfaces* **2016**, *8*, 10038−10047.

(197) Wadsworth, B. L.; Beiler, A. M.; Khusnutdinova, D.; Jacob, S. I.; Moore, G. F. Electrocatalytic and Optical Properties of Cobaloxime Catalysts Immobilized at a Surface-Grafted Polymer Interface. *ACS Catal.* **2016**, *6*, 8048−8057.

(198) Chandrasekaran, S.; Macdonald, T. J.; Mange, Y. J.; Voelcker, N. H.; Nann, T. A quantum dot sensitized catalytic porous silicon photocathode. *J. Mater. Chem. A* **2014**, *2*, 9478−9481.

(199) E vs RHE = E vs Ag/AgCl + 0.21 V + 0.059*pH.

(200) Lattimer, J. R. C.; Blakemore, J. D.; Sattler, W.; Gul, S.; Chatterjee, R.; Yachandra, V. K.; Yano, J.; Brunschwig, B. S.; Lewis, N. S.; Gray, H. B. Assembly, characterization, and electrochemical properties of immobilized metal bipyridyl complexes on silicon(111) surfaces. *Dalt. Trans.* **2014**, *43*, 15004−15012.

(201) Rakowski Dubois, M.; Dubois, D. L. Development of Molecular Electrocatalysts for CO_2 Reduction and H_2 Production/Oxidation. *Acc. Chem. Res.* **2009**, *42*, 1974−1982.

(202) Rakowski DuBois, M.; DuBois, D. L. The roles of the first and second coordination spheres in the design of molecular catalysts for H_2 production and oxidation. *Chem. Soc. Rev.* **2009**, *38*, 62−72.

(203) Seo, J.; Pekarek, R. T.; Rose, M. J. Photoelectrochemical operation of a surface-bound, nickel-phosphine H_2 evolution catalyst on p-Si(111): a molecular semiconductor|catalyst construct. *Chem. Commun.* **2015**, *51*, 13264−13267.

(204) Hanna, C. M.; Sanborn, C. D.; Ardo, S.; Yang, J. Y. Interfacial Electron Transfer of Ferrocene Immobilized onto Indium Tin Oxide through Covalent and Noncovalent Interactions. *ACS Appl. Mater. Interfaces* **2018**, *10*, 13211−13217.

(205) Downes, C. A.; Marinescu, S. C. Efficient Electrochemical and Photoelectrochemical H_2 Production from Water by a Cobalt Dithiolene One-Dimensional Metal-Organic Surface. *J. Am. Chem. Soc.* **2015**, *137*, 13740−13743.

(206) Gu, J.; Yan, Y.; Young, J. L.; Steirer, K. X.; Neale, N. R.; Turner, J. A. Water reduction by a p-GaInP$_2$ photoelectrode stabilized by an amorphous TiO_2 coating and a molecular cobalt catalyst. *Nat. Mater.* **2016**, *15*, 456−460.

(207) Kim, H. J.; Seo, J.; Rose, M. J. H_2 Photogeneration Using a Phosphonate-Anchored Ni-PNP Catalyst on a Band-Edge-Modified *p*-Si(111)|AZO Construct. *ACS Appl. Mater. Interfaces* **2016**, *8*, 1061−1066.

(208) Gurrentz, J. M.; Rose, M. J. Non-Catalytic Benefits of Ni(II) Binding to an Si(111)-PNP Construct for Photoelectrochemical Hydrogen Evolution Reaction: Metal Ion Induced Flat Band Potential Modulation. *J. Am. Chem. Soc.* **2020**, *142*, 5657−5667.

(209) Nam, D. H.; Zhang, J. Z.; Andrei, V.; Kornienko, N.; Heidary, N.; Wagner, A.; Nakanishi, K.; Sokol, K. P.; Slater, B.; Zebger, I.; et al. Solar Water Splitting with a Hydrogenase Integrated in Photoelectrochemical Tandem Cells. *Angew. Chem., Int. Ed.* **2018**, *57*, 10595−10599.

(210) Zhao, Y.; Anderson, N. C.; Ratzloff, M. W.; Mulder, D. W.; Zhu, K.; Turner, J. A.; Neale, N. R.; King, P. W.; Branz, H. M. Proton Reduction Using a Hydrogenase-Modified Nanoporous Black Silicon Photoelectrode. *ACS Appl. Mater. Interfaces* **2016**, *8*, 14481−14487.

(211) Khusnutdinova, D.; Beiler, A. M.; Wadsworth, B. L.; Jacob, S. I.; Moore, G. F. Metalloporphyrin-modified semiconductors for solar fuel production. *Chem. Sci.* **2017**, *8*, 253−259.

(212) Nishiori, D.; Wadsworth, B. L.; Reyes Cruz, E. A.; Nguyen, N. P.; Hensleigh, L. K.; Karcher, T.; Moore, G. F. Photoelectrochemistry of metalloporphyrin-modified GaP semiconductors. *Photosynth. Res.* **2022**, *151*, 195−204.

(213) Beiler, A. M.; Khusnutdinova, D.; Wadsworth, B. L.; Moore, G. F. Cobalt Porphyrin-Polypyridyl Surface Coatings for Photoelectrosynthetic Hydrogen Production. *Inorg. Chem.* **2017**, *56*, 12178−12185.

(214) Nguyen, N. P.; Wadsworth, B. L.; Nishiori, D.; Reyes Cruz, E. A.; Moore, G. F. Understanding and Controlling the Performance-Limiting Steps of Catalyst-Modified Semiconductors. *J. Phys. Chem. Lett.* **2021**, *12*, 199−203.

(215) Garner, L. E.; Steirer, K. X.; Young, J. L.; Anderson, N. C.; Miller, E. M.; Tinkham, J. S.; Deutsch, T. G.; Sellinger, A.; Turner, J. A.; Neale, N. R. Covalent Surface Modification of Gallium Arsenide Photocathodes for Water Splitting in Highly Acidic Electrolyte. *ChemSusChem* **2017**, *10*, 767−773.

(216) Rosser, T. E.; Hisatomi, T.; Sun, S.; Antón-García, D.; Minegishi, T.; Reisner, E.; Domen, K. $La_5Ti_2Cu_{0.9}Ag_{0.1}S_5O_7$ Modified with a Molecular Ni Catalyst for Photoelectrochemical H_2 Generation. *Chem. Eur. J.* **2018**, *24*, 18393−18397.

(217) Chandrasekaran, S.; Kaeffer, N.; Cagnon, L.; Aldakov, D.; Fize, J.; Nonglaton, G.; Baleras, F.; Mailley, P.; Artero, V. A robust ALD-protected silicon-based hybrid photoelectrode for hydrogen evolution under aqueous conditions. *Chem. Sci.* **2019**, *10*, 4469−4475.

(218) Tapia, C.; Bellet-Amalric, E.; Aldakov, D.; Boudoire, F.; Sivula, K.; Cagnon, L.; Artero, V. Achieving visible light-driven hydrogen evolution at positive bias with a hybrid copper-iron oxide|TiO_2-cobaloxime photocathode. *Green Chem.* **2020**, *22*, 3141−3149.

(219) Morrison, S. R. *Electrochemistry at Semiconductor and Oxidized Metal Electrodes*, 1st ed.; Springer US: New York, 1980.

(220) Hanna, C. M.; Pekarek, R. T.; Miller, E. M.; Yang, J. Y.; Neale, N. R. Decoupling Kinetics and Thermodynamics of Interfacial Catalysis at a Chemically Modified Black Silicon Semiconductor Photoelectrode. *ACS Energy Lett.* **2020**, *5*, 1848−1855.

(221) Pekarek, R. T.; Christensen, S. T.; Liu, J.; Neale, N. R. Energetic effects of hybrid organic/inorganic interfacial architecture

on nanoporous black silicon photoelectrodes. *Sustain. Energy Fuels* **2019**, *3*, 1660−1667.

(222) Nie, C.; Liu, C.; Gong, L.; Wang, M. Boosting the performance of a silicon photocathode for photoelectrochemical hydrogen production by immobilization of a cobalt tetraazamacrocyclic catalyst. *J. Mater. Chem. A* **2021**, *9*, 234−238.

(223) Parkinson, B. V.; Weaver, P. F. Photoelectrochemical pumping of enzymatic CO_2 reduction. *Nature* **1984**, *309*, 148−149.

(224) Arai, T.; Sato, S.; Uemura, K.; Morikawa, T.; Kajino, T.; Motohiro, T. Photoelectrochemical reduction of CO_2 in water under visible-light irradiation by a p-type InP photocathode modified with an electropolymerized ruthenium complex. *Chem. Commun.* **2010**, *46*, 6944−6946.

(225) Sato, S.; Arai, T.; Morikawa, T.; Uemura, K.; Suzuki, T. M.; Tanaka, H.; Kajino, T. Selective CO_2 Conversion to Formate Conjugated with H_2O Oxidation Utilizing Semiconductor/Complex Hybrid Photocatalysts. *J. Am. Chem. Soc.* **2011**, *133*, 15240−15243.

(226) Arai, T.; Tajima, S.; Sato, S.; Uemura, K.; Morikawa, T.; Kajino, T. Selective CO_2 conversion to formate in water using a CZTS photocathode modified with a ruthenium complex polymer. *Chem. Commun.* **2011**, *47*, 12664−12666.

(227) Wibowo, R. A.; Lee, E. S.; Munir, B.; Kim, K. H. Pulsed laser deposition of quaternary $Cu_2ZnSnSe_4$ thin films. *Phys. Status Solidi* **2007**, *204*, 3373−3379.

(228) Arai, T.; Sato, S.; Morikawa, T. A monolithic device for CO_2 photoreduction to generate liquid organic substances in a single-compartment reactor. *Energy Environ. Sci.* **2015**, *8*, 1998−2002.

(229) Schreier, M.; Luo, J.; Gao, P.; Moehl, T.; Mayer, M. T.; Grätzel, M. Covalent Immobilization of a Molecular Catalyst on Cu_2O Photocathodes for CO_2 Reduction. *J. Am. Chem. Soc.* **2016**, *138*, 1938−1946.

(230) Calzaferri, G.; Hädener, K.; Li, J. Photoreduction and electroreduction of carbon dioxide by a novel rhenium(I) *p*-phenylterpyridine carbonyl complex. *J. Photochem. Photobiol. A Chem.* **1992**, *64*, 259−262.

(231) Stanton, C. J.; Machan, C. W.; Vandezande, J. E.; Jin, T.; Majetich, G. F.; Schaefer, H. F.; Kubiak, C. P.; Li, G.; Agarwal, J. Re(I) NHC Complexes for Electrocatalytic Conversion of CO_2. *Inorg. Chem.* **2016**, *55*, 3136−3144.

(232) Huckaba, A. J.; Sharpe, E. A.; Delcamp, J. H. Photocatalytic Reduction of CO_2 with Re-Pyridyl-NHCs. *Inorg. Chem.* **2016**, *55*, 682−690.

(233) Jin, T.; He, D.; Li, W.; Stanton, C. J.; Pantovich, S. A.; Majetich, G. F.; Schaefer, H. F.; Agarwal, J.; Wang, D.; Li, G. CO_2 reduction with Re(I)-NHC compounds: driving selective catalysis with a silicon nanowire photoelectrode. *Chem. Commun.* **2016**, *52*, 14258−14261.

(234) Sekizawa, K.; Sato, S.; Arai, T.; Morikawa, T. Solar-Driven Photocatalytic CO_2 Reduction in Water Utilizing a Ruthenium Complex Catalyst on p-Type Fe_2O_3 with a Multiheterojunction. *ACS Catal.* **2018**, *8*, 1405−1416.

(235) Sekizawa, K.; Oh-Ishi, K.; Kataoka, K.; Arai, T.; Suzuki, T. M.; Morikawa, T. Stoichiometric water splitting using a p-type Fe_2O_3 based photocathode with the aid of a multi-heterojunction. *J. Mater. Chem. A* **2017**, *5*, 6483−6493.

(236) Shan, B.; Vanka, S.; Li, T. T.; Troian-Gautier, L.; Brennaman, M. K.; Mi, Z.; Meyer, T. J. Binary molecular-semiconductor p-n junctions for photoelectrocatalytic CO_2 reduction. *Nat. Energy* **2019**, *4*, 290−299.

(237) Leung, J. J.; Warnan, J.; Ly, K. H.; Heidary, N.; Nam, D. H.; Kuehnel, M. F.; Reisner, E. Solar-driven reduction of aqueous CO_2 with a cobalt bis(terpyridine)-based photocathode. *Nat. Catal.* **2019**, *2*, 354−365.

(238) Huang, J.; Xu, B.; Tian, L.; Pati, P. B.; Etman, A. S.; Sun, J.; Hammarström, L.; Tian, H. A heavy metal-free $CuInS_2$ quantum dot sensitized NiO photocathode with a Re molecular catalyst for photoelectrochemical CO_2 reduction. *Chem. Commun.* **2019**, *55*, 7918−7921.

(239) Huang, J.; Mulfort, K. L.; Du, P.; Chen, L. X. Photodriven Charge Separation Dynamics in CdSe/ZnS Core/Shell Quantum Dot/Cobaloxime Hybrid for Efficient Hydrogen Production. *J. Am. Chem. Soc.* **2012**, *134*, 16472−16475.

(240) Brown, K. A.; Harris, D. F.; Wilker, M. B.; Rasmussen, A.; Khadka, N.; Hamby, H.; Keable, S.; Dukovic, G.; Peters, J. W.; Seefeldt, L. C.; et al. Light-driven dinitrogen reduction catalyzed by a CdS:nitrogenase MoFe protein biohybrid. *Science* **2016**, *352*, 448−450.

(241) Brown, K. A.; Ruzicka, J.; Kallas, H.; Chica, B.; Mulder, D. W.; Peters, J. W.; Seefeldt, L. C.; Dukovic, G.; King, P. W. Excitation-Rate Determines Product Stoichiometry in Photochemical Ammonia Production by CdS Quantum Dot-Nitrogenase MoFe Protein Complexes. *ACS Catal.* **2020**, *10*, 11147−11152.

(242) Chica, B.; Ruzicka, J.; Kallas, H.; Mulder, D. W.; Brown, K. A.; Peters, J. W.; Seefeldt, L. C.; Dukovic, G.; King, P. W. Defining Intermediates of Nitrogenase MoFe Protein during N_2 Reduction under Photochemical Electron Delivery from CdS Quantum Dots. *J. Am. Chem. Soc.* **2020**, *142*, 14324−14330.

(243) Rockström, J. W.; Steffen, K.; Noone, Å.; Persson, F. S.; Chapin, E. F.; Lambin, T. M.; Lenton, M.; Scheffer, C.; Folke, H. J.; et al. Schellnhuber; et al. A safe operation space for humanity. *Nature* **2009**, *461*, 472−475.

(244) Steffen, W.; Richardson, K.; Rockström, J.; Cornell, S. E.; Fetzer, I.; Bennett, E. M.; Biggs, R.; Carpenter, S. R.; De Vries, W.; De Wit, C. A.; et al. Planetary boundaries: Guiding human development on a changing planet. *Science* **2015**, *347*, 1259855.

(245) Sato, S.; Morikawa, T.; Saeki, S.; Kajino, T.; Motohiro, T. Visible-Light-Induced Selective CO_2 Reduction Utilizing a Ruthenium Complex Electrocatalyst Linked to a p-Type Nitrogen-Doped Ta_2O_5 Semiconductor. *Angew. Chem., Int. Ed.* **2010**, *49*, 5101−5105.

(246) Suzuki, T. M.; Tanaka, H.; Morikawa, T.; Iwaki, M.; Sato, S.; Saeki, S.; Inoue, M.; Kajino, T.; Motohiro, T. Direct assembly synthesis of metal complex-semiconductor hybrid photocatalysts anchored by phosphonate for highly efficient CO_2 reduction. *Chem. Commun.* **2011**, *47*, 8673−8675.

(247) Chaudhary, Y. S.; Woolerton, T. W.; Allen, C. S.; Warner, J. H.; Pierce, E.; Ragsdale, S. W.; Armstrong, F. A. Visible light-driven CO_2 reduction by enzyme coupled CdS nanocrystals. *Chem. Commun.* **2012**, *48*, 58−60.

(248) Jin, T.; Liu, C.; Li, G. Photocatalytic CO_2 reduction using a molecular cobalt complex deposited on TiO_2 nanoparticles. *Chem. Commun.* **2014**, *50*, 6221−6224.

(249) Maeda, K.; Sekizawa, K.; Ishitani, O. A polymeric-semiconductor-metal-complex hybrid photocatalyst for visible-light CO_2 reduction. *Chem. Commun.* **2013**, *49*, 10127−10129.

(250) Kuriki, R.; Sekizawa, K.; Ishitani, O.; Maeda, K. Visible-Light-Driven CO_2 Reduction with Carbon Nitride: Enhancing the Activity of Ruthenium Catalysts. *Angew. Chem., Int. Ed.* **2015**, *54*, 2406−2409.

(251) Maeda, K.; Kuriki, R.; Ishitani, O. Photocatalytic Activity of Carbon Nitride Modified with a Ruthenium(II) Complex Having Carboxylic- or Phosphonic Acid Anchoring Groups for Visible-light CO_2 Reduction. *Chem. Lett.* **2016**, *45*, 182−184.

(252) Kuriki, R.; Ishitani, O.; Maeda, K. Unique Solvent Effects on Visible-Light CO_2 Reduction over Ruthenium(II)-Complex/Carbon Nitride Hybrid Photocatalysts. *ACS Appl. Mater. Interfaces* **2016**, *8*, 6011−6018.

(253) Ishida, H.; Tanaka, K.; Tanaka, T. Electrochemical CO_2 Reduction Catalyzed by $[Ru(bpy)_2(CO)_2]^{2+}$ and $[Ru(bpy)_2(CO)Cl]^+$. The Effect of pH on the Formation of CO and $HCOO^-$. *Organometallics* **1987**, *6*, 181−186.

(254) Roy, S.; Reisner, E. Visible-Light-Driven CO_2 Reduction by Mesoporous Carbon Nitride Modified with Polymeric Cobalt Phthalocyanine. *Angew. Chem., Int. Ed.* **2019**, *58*, 12180−12184.

(255) Hamby, H.; Li, B.; Shinopoulos, K. E.; Keller, H. R.; Elliott, S. J.; Dukovic, G. Light-driven carbon-carbon bond formation via CO_2 reduction catalyzed by complexes of CdS nanorods and a 2-oxoacid oxidoreductase. *Proc. Natl. Acad. Sci. U. S. A.* **2020**, *117*, 135−140.

(256) Ma, B.; Chen, G.; Fave, C.; Chen, L.; Kuriki, R.; Maeda, K.; Ishitani, O.; Lau, T. C.; Bonin, J.; Robert, M. Efficient Visible-Light-Driven CO_2 Reduction by a Cobalt Molecular Catalyst Covalently Linked to Mesoporous Carbon Nitride. *J. Am. Chem. Soc.* **2020**, *142*, 6188−6195.

(257) Wang, X.; Blechert, S.; Antonietti, M. Polymeric Graphitic Carbon Nitride for Heterogeneous Photocatalysis. *ACS Catal.* **2012**, *2*, 1596−1606.

(258) Ma, B.; Blanco, M.; Calvillo, L.; Chen, L.; Chen, G.; Lau, T.-C.; Dražić, G.; Bonin, J.; Robert, M.; Granozzi, G. Hybridization of Molecular and Graphene Materials for CO_2 Photocatalytic Reduction with Selectivity Control. *J. Am. Chem. Soc.* **2021**, *143*, 8414−8425.

(259) Ma, X.; Hu, C.; Bian, Z. Hybrid photocatalytic systems comprising a manganese complex anchored on g-C_3N_4 for efficient visible-light photoreduction of CO_2. *Inorg. Chem. Commun.* **2020**, *117*, 107951.

(260) Tian, S.; Chen, S.; Ren, X.; Hu, Y.; Hu, H.; Sun, J.; Bai, F. An efficient visible-light photocatalyst for CO_2 reduction fabricated by cobalt porphyrin and graphitic carbon nitride via covalent bonding. *Nano Res.* **2020**, *13*, 2665−2672.

(261) Sun, J.; Bian, J.; Li, J.; Zhang, Z.; Li, Z.; Qu, Y.; Bai, L.; Yang, Z. Di; Jing, L. Efficiently photocatalytic conversion of CO_2 on ultrathin metal phthalocyanine/g-C_3N_4 heterojunctions by promoting charge transfer and CO_2 activation. *Appl. Catal. B Environ.* **2020**, *277*, 119199.

(262) Wang, Z.; Zhou, W.; Wang, X.; Zhang, X.; Chen, H.; Hu, H.; Liu, L.; Ye, J.; Wang, D. Enhanced Photocatalytic CO_2 Reduction over TiO_2 Using Metalloporphyrin as the Cocatalyst. *Catalysts* **2020**, *10*, 654.

(263) Shang, B.; Zhao, F.; Choi, C.; Jia, X.; Pauly, M.; Wu, Y.; Tao, Z.; Zhong, Y.; Harmon, N.; Maggard, P. A.; et al. Monolayer Molecular Functionalization Enabled by Acid-Base Interaction for High-Performance Photochemical CO_2 Reduction. *ACS Energy Lett.* **2022**, *7*, 2265−2272.

(264) Artero, V.; Savéant, J.-M. Toward the rational benchmarking of homogeneous H_2-evolving catalysts. *Energy Environ. Sci.* **2014**, *7*, 3808−3814.

(265) Costentin, C.; Savéant, J.-M. Towards an intelligent design of molecular electrocatalysis. *Nat. Rev. Chem.* **2017**, *1*, 0087.

(266) Ashkenasy, G.; Cahen, D.; Cohen, R.; Shanzer, A.; Vilan, A. Molecular Engineering of Semiconductor Surfaces and Devices. *Acc. Chem. Res.* **2002**, *35*, 121−128.

(267) Bae, D.; Seger, B.; Vesborg, P. C. K.; Hansen, O.; Chorkendorff, I. Strategies for stable water splitting *via* protected photoelectrodes. *Chem. Soc. Rev.* **2017**, *46*, 1933−1954.

(268) Kim, J. H.; Hansora, D.; Sharma, P.; Jang, J.-W.; Lee, J. S. Toward practical solar hydrogen production-an artificial photosynthetic leaf-to-farm challenge. *Chem. Soc. Rev.* **2019**, *48*, 1908−1971.

(269) Corbin, N.; Zeng, J.; Williams, K.; Manthiram, K. Heterogeneous molecular catalysts for electrocatalytic CO_2 reduction. *Nano Res.* **2019**, *12*, 2093−2125.

(270) Margarit, C. G.; Schnedermann, C.; Asimow, N. G.; Nocera, D. G. Carbon Dioxide Reduction by Iron Hangman Porphyrins. *Organometallics* **2019**, *38*, 1219−1223.

(271) Liu, Y.; McCrory, C. C. L. Modulating the mechanism of electrocatalytic CO2 reduction by cobalt phthalocyanine through polymer coordination and encapsulation. *Nat. Commun.* **2019**, *10*, 1683.

(272) Sun, Z.; Ma, T.; Tao, H.; Fan, Q.; Han, B. Fundamentals and Challenges of Electrochemical CO_2 Reduction Using Two-Dimensional Materials. *Chem* **2017**, *3*, 560−587.

(273) Hu, C.; Zhang, L.; Gong, J. Recent progress made in the mechanism comprehension and design of electrocatalysts for alkaline water splitting. *Energy Environ. Sci.* **2019**, *12*, 2620−2645.

(274) Modestino, M. A.; Walczak, K. A.; Berger, A.; Evans, C. M.; Haussener, S.; Koval, C.; Newman, J. S.; Ager, J. W.; Segalman, R. A. Robust production of purified H_2 in a stable, self-regulating, and continuously operating solar fuel generator. *Energy Environ. Sci.* **2014**, *7*, 297−301.

(275) Rabinowitz, J. A.; Kanan, M. W. The future of low-temperature carbon dioxide electrolysis depends on solving one basic problem. *Nat. Commun.* **2020**, *11*, 10−12.

(276) Moore, G. F. *Photosynthesis: Structures, Mechanisms, and Applications*; Springer International Publishing, 2017; pp 407−415.

(277) Nguyen, N. P.; Moore, G. F. Storing sunlight at low temperatures? *Joule* **2021**, *5*, 2254−2256.

(278) Koval, C. A.; Lercher, J.; Scott, S. L. *Basic Research Needs for Catalysis Science*; U.S. Department of Energy, 2017.

(279) Heinz, T.; Shpyrko, O. *Basic Energy Sciences Roundtable on Opportunities for Basic Research at the Frontiers of XFEL Ultrafast Science*; U.S. Department of Energy, 2017. DOI: 10.2172/1616251

(280) Ratner, D.; Sumpter, B. *Basic Energy Sciences Roundtable on Producing and Managing Large Scientific Data with Artificial Intelligence and Machine Learning*; U.S. Department of Energy, 2019. DOI: 10.2172/1630823

(281) Petford-Long, A.; Gilbert, B. *Basic Energy Sciences Roundtable on Research Opportunities in the Physical Sciences Enabled by Cryogenic Electron Microscopy*; U.S. Department of Energy, 2021.